

UNIVERSITY OF SÃO PAULO  
DEPARTMENT OF MINING AND PETROLEUM ENGINEERING

VICTOR JORGE DE OLIVEIRA MARUM

**Efficiency analysis of an incompressible-flow ejector using  
Computational Fluid Dynamics (CFD) simulations and mathematical  
modeling**

São Paulo

2020

VICTOR JORGE DE OLIVEIRA MARUM

**Efficiency analysis of an incompressible-flow ejector using  
Computational Fluid Dynamics (CFD) simulations and mathematical  
modeling**

Corrected Version

Dissertation presented to the Polytechnic School  
of the University of São Paulo for obtaining the  
title of Master of Science.

Concentration area: Mineral Engineering.

Supervisor: Prof. Rafael dos Santos Gioria, PhD.

São Paulo


2020

Autorizo a reprodução e divulgação total ou parcial deste trabalho, por qualquer meio convencional ou eletrônico, para fins de estudo e pesquisa, desde que citada a fonte.

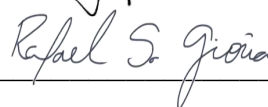
Este exemplar foi revisado e corrigido em relação à versão original, sob responsabilidade única do autor e com a anuência de seu orientador.

São Paulo, 5 de dezembro de 2020.

Assinatura do autor:

 Victor Marum

Assinatura do orientador:

 Rafael S. Gioia

#### Catálogo-na-publicação

Marum, Víctor Jorge de Oliveira

Efficiency analysis of an incompressible-flow ejector using Computational Fluid Dynamics (CFD) simulations and mathematical modeling / V.J.O. Marum -- versão corr. – São Paulo, 2020.

107 p.

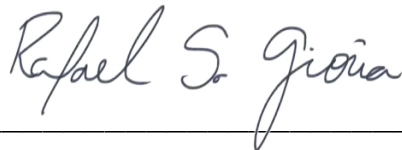
Dissertação (Mestrado) – Escola Politécnica da Universidade de São Paulo. Departamento de Engenharia de Minas e Petróleo.

1.Ejector 2.Computational Fluid Dynamics 3.Efficiency analysis  
4.Carbon Capture and Storage. I. Universidade de São Paulo. Escola Politécnica. Departamento de Engenharia de Minas e Petróleo II.t.

MARUM, Victor Jorge de Oliveira. **Efficiency analysis of an incompressible-flow ejector using Computational Fluid Dynamics (CFD) simulations and mathematical modeling.** 2020. 107 p. Dissertation (Master of Science) – Polytechnic School, University of São Paulo, São Paulo, 2020.

Approved in: October 9<sup>th</sup>, 2020.

EXAMINING COMMITTEE



---

Prof. Rafael dos Santos Gioria, PhD.  
Universidade de São Paulo (USP)



---

Ivan Korkischko, PhD.  
Universidade de São Paulo (USP)



---

Prof. Reinaldo Marcondes Orselli, PhD.  
Universidade Federal do ABC (UFABC)

*To my parents.*

# Acknowledgements

For me, this section is the most important part of an academic manuscript. While writing the *Acknowledgements*, we realize that nobody does anything alone and the credits must be properly distributed to people and institutions that have participated, directly or indirectly, in the work.

First of all, I would like to express my sincere gratitude to my supervisor, Professor Rafael dos Santos Gioria, for his unconditional support and motivation throughout the development of this work. It was a very satisfying experience for me to work under his guidance. His generosity, goodness, patience and commitment are admirable and inspiring! Thank you very much for absolutely everything!

“*Poor is the disciple who forgets his first mentor*”. I would be unfair if I forgot to recognize the contributions of Professor Oleg Bokhonok, my undergraduation supervisor, to my academic experience. He introduced me to the scientific research and taught me so much of what I know today. Thank you for the encouragement and friendship!

Thanks to Professor Ronaldo Carrion and Professor Marcio Augusto Sampaio Pinto for the courtesy of providing the infrastructure of their laboratories (*Laboratório de Mecânica Computacional* and *Laboratório de Simulação e Gerenciamento de Reservatórios de Petróleo – LASG*, respectively) as a valuable contribution to the development of this work.

I also thank Professor Ronaldo Carrion who, together with PhD. Renato Picelli Sanches, gave valuable suggestions in my master’s qualification exam to improve this work.

My master’s scholarship was completely sponsored by Research Centre for Gas Innovation (RCGI) through *Fundação de Apoio à Universidade de São Paulo (FUSP)*, contract number: 3141/38. Thank you very much for the financial support! I take this paragraph to also thank my partners in Project 38 of RCGI, who integrated with me the “Ejector Team”.

I would never forget to thank the staff members of the Department of Mining and Petroleum Engineering (PMI), especially the secretaries, librarians and people responsible for cleaning. They contribute to education as much as professors and researchers!

This work would have been more difficult and boring if there were not the pleasant moments shared with my research colleagues. Our post-lunch chats, filled with discussion about polemic issues, will never be forgotten!

I am so grateful to PhD. Marcelo Bessa Nisti for all advices and motivation transmitted between the series of physical exercises at gym. His words helped me to face the scientific research from a different perspective! Thank you!

Finally, but nonetheless important, I express my complete gratitude to my parents, Marlene and Napoleão, to whom I absolutely owe everything I have and everything I am. And to my sister, Vanessa, who teaches me every day the meaning of the word *patience*! Thank you for the unconditional support and for always believing in what I decide to do. My love for you has the dimension of the Universe, if we believe it is infinite!

*“Estamos a destruir o planeta e o egoísmo de cada geração não se preocupa em perguntar como é que vão viver os que virão depois. A única coisa que importa é o triunfo do agora. É a isto que eu chamo a cegueira da razão”.*

*– José Saramago  
(in “Ensaio sobre a cegueira”)*



# Abstract

MARUM, Victor Jorge de Oliveira. **Efficiency analysis of an incompressible-flow ejector using Computational Fluid Dynamics (CFD) simulations and mathematical modeling.** 2020. 107 p. Dissertation (Master of Science) – Polytechnic School, University of São Paulo, São Paulo, 2020.

Carbon Capture and Storage (CCS) is capable of delivering significant emissions reduction of carbon dioxide (CO<sub>2</sub>) into atmosphere. In CCS applications, CO<sub>2</sub> must be compressed at high pressures to be reinjected into depleted hydrocarbon reservoirs by a mechanical machine, such as ejectors. In this work, a quasi-one-dimensional (1D) mathematical approach from literature was employed to perform a theoretical analysis of an incompressible-flow ejector, using results from Computational Fluid Dynamics (CFD) simulations as input data. In order to properly express the non-uniformity of the velocity and pressure profiles at the ejector sections, kinetic-energy and pressure correction factors were employed in the results from CFD simulations. In addition, a new efficiency approximation is proposed including those correction factors on its formulation. Finally, a sensitivity analysis was conducted aiming to investigate the influence of each ejector component on its performance. The results have shown that the mathematical approach from literature presents good agreement with the CFD results and could accurately delimit the ejector's envelope of operation and predict its efficiency peak. And the new approximation has presented lower deviation from CFD results for specific entrainment ratio ( $M$ ) values. The plots of the pressure and velocity profiles indicated that the pressure stabilization occurs inside the mixing section and the velocity stabilization takes place inside the diffuser. The sensitivity analysis pointed out that the nozzle geometry affects the ejector's efficiency curve for all  $M$  while geometries of the suction chamber, mixing section and diffuser affect the efficiency curve only for higher and intermediate  $M$ .

**Keywords:** Ejector. Computational Fluid Dynamics. Efficiency analysis. Carbon Capture and Storage.

# Resumo

MARUM, Victor Jorge de Oliveira. **Análise da eficiência de um ejetor de escoamento incompressível utilizando Dinâmica de Fluidos Computacional (CFD) e modelagem matemática.** 2020. 107 p. Dissertação (Mestre em Ciências)–Escola Politécnica, Universidade de São Paulo, São Paulo, 2020.

A técnica de Captura e Armazenamento de Carbono (CCS) é capaz de proporcionar reduções significativas das emissões de dióxido de carbono ( $\text{CO}_2$ ) na atmosfera. Nas operações de CCS, o  $\text{CO}_2$  deve ser comprimido a altas pressões para ser reinjetado em reservatórios de hidrocarbonetos depletados por meio de equipamentos mecânicos, como, por exemplo, ejetores. No presente trabalho, um modelo matemático quase-unidimensional (1D) da literatura foi utilizado para realizar uma análise teórica de um ejetor de escoamento incompressível, usando-se resultados de simulações de Dinâmica de Fluidos Computacional (CFD) como parâmetros de *input*. A fim de expressar adequadamente a não uniformidade dos perfis de velocidade e de pressão nas seções do ejetor, foram empregados fatores de correção de energia cinética e de pressão nos resultados das simulações de CFD. Além disso, uma nova aproximação de eficiência é proposta incluindo estes fatores de correção. Por fim, uma análise de sensibilidade foi realizada para investigar a influência de cada componente do ejetor em seu desempenho. Os resultados mostraram que o modelo matemático da literatura apresenta boa concordância com os resultados de CFD, sendo capaz de delimitar o envelope de operação do ejetor e o seu pico de eficiência. E a nova aproximação apresentou menor desvio em relação aos resultados de CFD para valores específicos do parâmetro *entrainment ratio* ( $M$ ). Os perfis de pressão e de velocidade indicaram que a estabilização da pressão ocorre no interior da seção de mistura e a estabilização da velocidade ocorre no interior difusor. A análise de sensibilidade indicou que a geometria do bocal afeta a curva de eficiência do ejetor para todos os valores de  $M$ , enquanto que as geometrias da câmara de sucção, da seção de mistura e do difusor impactam a curva de eficiência apenas para valores mais altos e intermediários de  $M$ .

**Palavras-chave:** Ejetor. Dinâmica de Fluidos Computacional. Análise de eficiência. Captura e Armazenamento de Carbono.

# Nomenclature

## Abbreviations

1D	One-dimensional
2D	Two-dimensional
3D	Three-dimensional
CCS	Carbon Capture and Storage
CFD	Computational Fluid Dynamics
CO <sub>2</sub>	Carbon dioxide
COP	Coefficient of performance
EPUSP	Polytechnic School of the University of São Paulo
FEM	Finite Element Method
GJG	Gas-jet-gas
IEA	International Energy Agency
LJG	Liquid-jet-gas
LJGL	Liquid-jet-gas-liquid
LJL	Liquid-jet-liquid
OP	Operating condition
RCGI	Research Centre for Gas Innovation
SDG	Sustainable Development Goals
UN	United Nations

## Roman symbols

$a$	Mixing-section-to-diffuser area ratio
$a_1$	Constant of the $k-\omega$ SST turbulence model formulation
$A$	Cross-sectional area
$a_s$	Acceleration of the infinitesimal fluid particle in the streamline direction
$C_{1\varepsilon}, C_{2\varepsilon}, C_\mu$	Dimensionless constants
$D$	Diameter
$d\vec{S}$	Unit of surface
$E$	Total energy per unit mass

$f$	Friction factor
$F_2$	Blending function of the $k-\omega$ SST turbulence model formulation
$\vec{F}$	Flux crossing an arbitrary control surface
$\vec{f}_e$	External volume forces per unit mass
$g$	Gravity
$H$	Stagnation or total enthalpy
$h_L$	Head losses
$\bar{I}$	Unit tensor
$k$	Turbulent kinetic energy
$K, K'$	Friction loss coefficient, corrected friction loss coefficient
$L$	Length
$\dot{m}$	Mass flow rate
$M$	Entrainment ratio
$\hat{n}$	Unit vector pointing outward the infinitesimal area element $dA$
$N, N_{ideal}, N'$	Pressure recovery ratio, maximum theoretical pressure recovery ratio, corrected pressure recovery ratio
$NXP$	Nozzle exit position
$p, P, \bar{P}, \bar{P}'$	Pressure, static pressure, total pressure, corrected total pressure
$P_k$	Rate of production of turbulent kinetic energy
$q_H$	Heat sources other than conduction
$Q, \dot{Q}$	Volumetric flow rate, general rate of heat transfer
$\vec{Q}_S, Q_V$	Surface source, volume source
$R$	Nozzle-to-mixing-section area ratio
$t$	Time
$S$	Arbitrary control surface
$T$	Absolute temperature
$U$	Scalar quantity per unit of volume
$\vec{v}, V, \bar{V}, \bar{V}$	Velocity vector, average velocity, velocity ratio, velocity profile at a specific cross section
$W_f$	Work of the external volume forces
$\dot{W}$	Total work rate
$\dot{W}_S$	Work rate resulting from rotating shafts

$\dot{W}_{shear}$	Work rate due to shear acting on moving boundaries
$\dot{W}_I$	Work rate due to movement of the control volume in relation to a fixed reference frame
$z$	Position of a fluid particle in relation to a fixed reference frame

### **Greek symbols**

$\alpha$	Kinetic-energy correction factor
$\beta_1, \beta_2, \beta^*$	Dimensionless constants
$\gamma$	Pressure correction factor
$\gamma_1, \gamma_2$	Dimensionless constants
$\delta$	Correlation factor of the new efficiency approximation
$\delta_N$	Nozzle tip thickness
$\varepsilon$	Rate of viscous dissipation
$\eta, \eta_{ideal}, \eta^{new}$	Ejector's efficiency, ejector's theoretical maximum efficiency (ideal efficiency), ejector's new approximation
$\theta$	Suction chamber convergent angle
$\ell$	Length scale
$\kappa$	Thermal conductivity coefficient
$\lambda$	Correlation factor of the new efficiency approximation
$\mu, \mu_t$	Dynamic viscosity, eddy viscosity
$\rho$	Density
$\sigma$	Correlation factor of the new efficiency approximation
$\sigma_k, \sigma_\varepsilon$	Prandtl's dimensionless and constant numbers
$\sigma_\omega, \sigma_{\omega,1}, \sigma_{\omega,2}$	Dimensionless constants
$\tau, \bar{\tau}$	Shear stress, viscous shear stress tensor
$\vartheta$	Velocity scale
$\varphi$	Diffuser divergent angle
$\Omega$	Arbitrary control volume
$\omega$	Turbulence frequency

### **Subscripts**

1	Referred to the primary flow
2	Referred to the secondary flow

$3$	Referred to the mixture between primary and secondary flows
$i$	Referred to the nozzle inlet position
$n$	Referred to the nozzle outlet position
$s$	Referred to the suction chamber inlet position
$v$	Referred to the suction chamber outlet position
$o$	Referred to the mixing section inlet position
$t$	Referred to the mixing section outlet position
$d$	Referred to the diffuser outlet position
$NI$	Referred to the nozzle inlet
$NT$	Referred to the nozzle throat
$NO$	Referred to the nozzle outlet
$S$	Referred to the suction chamber
$M$	Referred to the mixing section
$D$	Referred to the diffuser
$W$	Referred to the internal wall of the mixing section

### **Others**

$\otimes$	Tensor product operator
$\vec{\nabla}$	Gradient or divergent operator
$D/Dt$	Material derivative (used for the Lagrangian description of a fluid motion)

# Contents

<b>Chapter 1: Introduction.....</b>	<b>16</b>
1.1 Contextualization .....	16
1.2 Objectives.....	20
<b>Chapter 2: Literature Review and Theoretical Aspects.....</b>	<b>22</b>
2.1 Historical overview .....	22
2.2 Ejector system.....	22
2.3 Components of ejectors .....	23
2.3.1 Nozzle.....	24
2.3.2 Suction chamber .....	26
2.3.3 Mixing section.....	27
2.3.4 Diffuser .....	28
2.4 Classification of ejectors .....	29
2.5 Ejector modeling.....	29
2.5.1 Mathematical modeling for compressible-flow ejectors.....	30
2.5.2 Mathematical modeling for incompressible-flow ejectors .....	31
2.6 Basics of Computational Fluid Dynamics .....	31
2.7 General description of the Finite Element Method (FEM).....	34
2.8 Study of ejectors using CFD.....	35
<b>Chapter 3: Methodology .....</b>	<b>37</b>
3.1 Computational set up.....	37
3.1.1 Geometry building .....	38
3.1.2 Material specification .....	38
3.1.3 Definition of assumptions and boundary conditions .....	38
3.1.4 Turbulence model definition.....	39
3.1.4.1 $k-\varepsilon$ turbulence model.....	40
3.1.4.2 $k-\omega$ turbulence model.....	41
3.1.4.3 $k-\omega$ SST turbulence model .....	43
3.1.5 Meshing .....	44
3.1.6 Simulation running and postprocessing .....	44

3.2	Mathematical modeling.....	44
3.2.1	The Bernoulli equation.....	45
3.2.2	Friction losses.....	47
3.2.3	Mathematical model for incompressible-flow ejectors.....	48
3.2.4	Pressure correction factor ( $\gamma$ ).....	52
3.2.5	Kinetic-energy correction factor ( $\alpha$ ).....	54
3.2.6	Equations with corrected factors.....	54

**Chapter 4: Results and Discussion .....56**

4.1	Mesh refinement study.....	56
4.2	Computational model validation.....	58
4.3	Results from CFD simulations.....	59
4.3.1	Internal pressure distribution.....	62
4.3.2	Internal velocity distribution.....	64
4.3.3	Pressure profiles at the ejector sections.....	65
4.3.4	Velocity profiles at the ejector sections.....	70
4.4	Calculation of the friction loss coefficients.....	75
4.5	Efficiency analysis with the mathematical model.....	76
4.6	Calculation of the corrected friction loss coefficients.....	77
4.7	A new approximation.....	80
4.8	Sensitivity analysis.....	88
4.9	Derivatives of the sensitivity curves.....	94

**Chapter 5: Conclusions .....97**

	Bibliography.....	99
--	-------------------	----



# Chapter 1

## Introduction

*“Carbon capture and storage (CCS) is the only technology able to deliver significant emissions reductions from the use of fossil fuels in power generation and industrial applications”.*

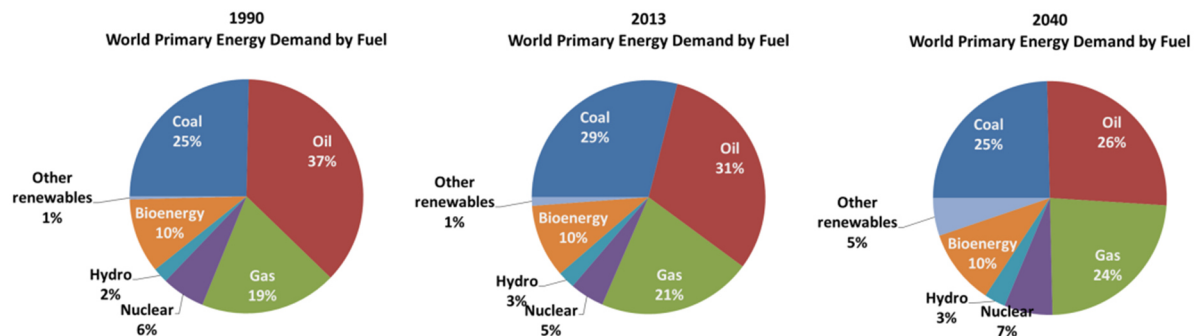
*– International Energy Agency (2015).*

### **1.1 Contextualization**

Petroleum is everywhere! In modern society, we rarely find an environment or a product that does not contain petroleum or its derivatives. Natural, non-renewable and limited in nature, petroleum moves billions of dollars every day in an enormous industrial activity, employing thousands of workers, technicians and scientists. A considerable amount of resources is allocated for the development of new research in the petroleum industry, enabling the emergence of new-sophisticated technologies to discover potential oil reserves and improving existing techniques for drilling, production, transportation and refining activities (THOMAS, 2001).

It is nothing new for anyone that petroleum production is far from being considered as a reasonably clean activity. The process of petroleum extraction is followed by generation of large amounts of waste, high-energy demand and production of greenhouse gases. Although countries increasingly tend to adopt renewable energy in their industrial activities, the use of fossil fuels will not end anytime soon, and a significantly percentage of world’s primary energy will be required for the next years as consequence (see Figure 1.1). Therefore, environmental damage due to those

Figure 1.1 – Global primary energy demand by fuel in 1990, 2013 and 2040 (in the New Policies Scenario proposed by IEA).



Source: Adapted from INTERNATIONAL ENERGY AGENCY (2015a).

activities must be minimized and controlled so that future generations are not severely harmed.

Motivated by the urgent demand for a more sustainable planet, the United Nations (UN) has launched the *2030 Agenda for Sustainable Development* – known today as *Agenda 2030* – which was adopted by all UN Member States in 2015 as a plan of action for people, planet and prosperity. This Agenda proposes 17 Sustainable Development Goals (SDG) and 169 associated targets to eradicate poverty and other deprivations that must go hand-in-hand with strategies that improve health and education, reduce social inequality and stimulate economic growth, while tackling climate change and working to preserve the oceans and forests (UNITED NATIONS, 2015).

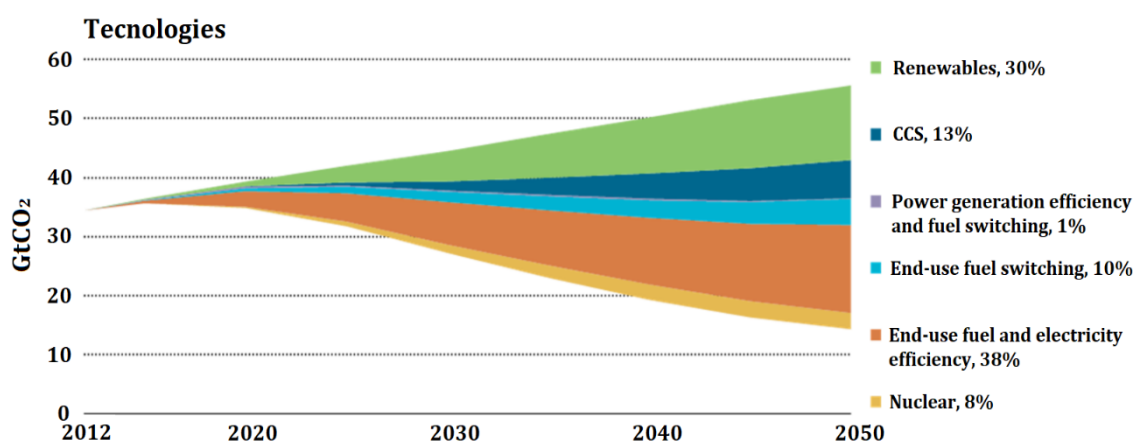
Specifically for the planet, the SDG aim to protect it from degradation by encouraging people for a more sustainable consumption and production, managing its natural resources and adopting urgent measures for climate change, so that it can support the needs of the present and future generations (UNITED NATIONS, 2015).

During the development of a hydrocarbon field, gas may be produced in addition to oil and water containing into reservoirs. The most common type of gas to be produced is the carbon dioxide (CO<sub>2</sub>), which is one of the major responsible for the greenhouse effect and global warming (MERCER, 1978; ANDERSON; HAWKINS; JONES, 2016). A strategy to mitigate environmental damages associated to undesirable CO<sub>2</sub> production must be properly selected since discharging it into atmosphere is not a sustainable option and goes against the Agenda 2030.

The injection of CO<sub>2</sub> into geological formations in subsurface is considered a good strategy to sustainably solve the problem of unwanted CO<sub>2</sub> production. This

technique is one of the Carbon Capture and Storage (CCS) modalities. According to the International Energy Agency (IEA) – a global authority in promoting policies aimed at controlling CO<sub>2</sub> emissions –, CCS could deliver 13% of the cumulative emissions reductions needed by 2050 to limit the predicted global increase in temperature to 2 °C (Figure 1.2) (INTERNATIONAL ENERGY AGENCY, 2015b). To conduct a CCS operation, the most commonly options employed are the CO<sub>2</sub> storage into saline aquifers and the CO<sub>2</sub> reinjection into depleted hydrocarbon reservoirs (RACKLEY, 2010).

Figure 1.2 – Contribution of technologies and sectors for the global cumulative CO<sub>2</sub> reductions.



Source: Adapted from INTERNATIONAL ENERGY AGENCY (2015c).

To be reinjected into depleted reservoirs, CO<sub>2</sub> needs to be compressed at high pressures in industrial plants by a mechanical machine, such as a compressor, a vacuum pump or an ejector. The main advantages of ejectors in comparison with pumps and compressors are their structure with no moving parts (PARK; LIM; YOON, 2008), absence of lubricants or bearings (LITTLE; GARIMELLA; DIPRETE, 2016), reliability and low installation cost (SHESTOPALOV et al., 2015), and the fact that their pumping process does not require external work.

Ejectors (see Figure 1.3) have been proved to be effective devices and their applications are extended to several engineering segments: in aeronautics to increase reliability of aircrafts propulsion (e.g. KRACÍK; DVOŘÁK, 2015), in thermal energy refrigeration systems (e.g. BESAGNI; MEREU; INZOLI, 2016), in desalination processes (e.g. WANG et al., 2017), in laser tomography procedures (e.g. BOUHANGUEL; DESEVAUX; GAVIGNET, 2011) and in the petroleum industry for

Figure 1.3 – A typical ejector.



Source: RITM Industry®

artificial lift, flow assurance (e.g. PEDROSO, 2015) and CCS applications (e.g. RACKLEY, 2010). On the other hand, ejectors have low efficiency compared with other mechanical devices (i.e. pumps and compressors) and they are constructed to achieve the best performance at a specific operating condition (OP) (HAMZAOUI et al., 2018). For this reason, their geometry must be properly designed and optimization studies are strongly recommended (e.g. FAN et al., 2011; SADEGHI et al., 2017; SANAYE; NIROOMAND, 2011; WANG et al., 2017; YAPICI; ALDAS, 2013).

To understand the complex nature of the flow field inside ejectors, theoretical mathematical models may provide relevant information. Although the internal flow field of ejectors is three-dimensional, one-dimensional (1D) mathematical approaches can guide system operation, interpret experimental results, assist in system design and optimization (HE; LI; WANG, 2009), determine the ejector maximum efficiency point (ANTONIO et al., 2012) and predict the ejector performance at critical and subcritical operation modes in compressible-flow models (CHEN et al., 2013).

Another tool for ejector modeling is the Computational Fluid Dynamics (CFD) technique, which can provide a detailed description of the flow field inside ejectors by numerical solutions. CFD technique is proven to be an efficient method to overcome some limitations of 1D mathematical approaches (LEE et al., 2016). In last years, CFD technique has been used to accurately investigate the influence of friction loss coefficients and ejector geometry on its performance (WANG et al., 2017; WU et al., 2014; ZHANG et al., 2018), to study the flow distribution inside ejectors (ZHU et al.,

2017) and also to optimize the ejector geometrical parameters (YADAV; PATWARDHAN, 2008).

This dissertation contributes to development of one of the Research Centre for Gas Innovation (RCGI) thematic projects. RCGI is a global institute for advanced studies on sustainable development of the energy sector, located at Polytechnic School of the University of São Paulo (EPUSP). The global project in which this present work is inserted is entitled “*High efficiency ejector for gas compression*” and its main objective is to develop a highly efficient ejector system capable of compressing CO<sub>2</sub> at high pressures to be applied into CCS activities.

In the present and preliminary study, a quasi-1D mathematical approach was employed to perform a theoretical analysis of an incompressible-flow ejector model using data from CFD simulations. This incompressible-flow analysis is important – even recognizing the compressible characteristic of CCS operations – to build knowledge and experience with the ejector modeling, initially achieved through a more simplified approach. Theoretical analysis includes the estimation of the ejector’s friction loss coefficients and the study of the ejector’s efficiency curve. Results presented in this dissertation should aggregate for the progress of the RCGI global project and also – even if minimally – to the fulfillment of Agenda 2030, as a humble contribution to the attempt of transforming our planet into a more sustainable place.

## **1.2 Objectives**

The global objective of this work is to perform a theoretical analysis of an incompressible-flow ejector to be used as a first step in the comprehension of an ejector system, which will be employed in CCS activities in the future. As specific objectives, this dissertation aims to:

- Analyze the feasibility of a quasi-1D mathematical approach to study the efficiency of an incompressible-flow ejector, including delimitation of the theoretical maximum efficiency that the ejector can reach (envelope of operation) and prediction of the ejector’s maximum efficiency point (efficiency peak);
- Build and validate a computational set up to conduct the CFD simulations with the purpose of generating data to be used as input into the mathematical approach;

- Propose a method to estimate the friction loss coefficients of each ejector component, useful for cases when data of CFD simulations are available;
- Investigate the applicability of the kinetic-energy and pressure correction factors into the CFD data in order to properly express the non-uniformity of the pressure and velocity profiles in some ejector's sections of interest;
- Study the influence of each ejector component on its performance through a sensitivity analysis;
- Generate results that can cooperate to the development of the RCGI's ejector project.

## Chapter 2

# Literature Review and Theoretical Aspects

*“No theory is good except on condition that one use it to go on beyond”.*

*– André P. G. Gide (1869 – 1951)*

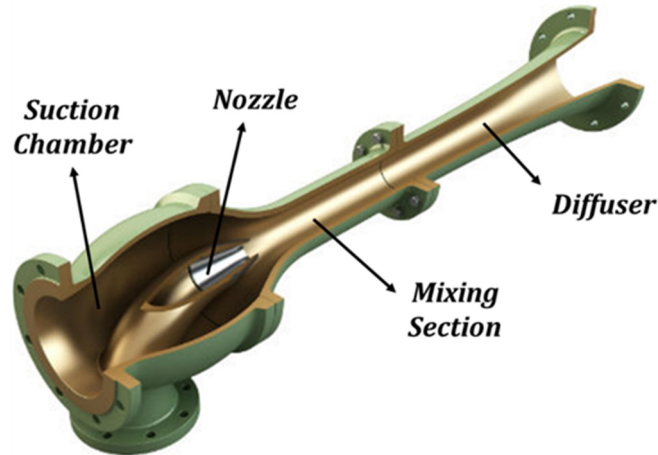
### **2.1 Historical overview**

In the nineteenth century, limitations of some mechanical pumps for replenishing boilers with steam engines were overcome in 1858 with the invention of the first ejector registered in literature (ELBEL, 2011). The ejector basic design theory was firstly proposed at the beginning of 1860s, and it was later improved after the advances on mathematical theory for combined streams conducted by RANKINE (1870). Ejector theory was conceptualized in 1901 by Charles Pearson after a successful application of the device for removing air from a steam-engine condenser. Later, an ejector was used by Maurice Leblanc in the first steam jet refrigeration system in 1910 (GOSNEY, 1982). These events are considered by many authors as the “birth of ejectors”.

### **2.2 Ejector system**

Ejectors are mechanical devices that use a high-pressure flow (called *primary flow*) to suction and pump a low-pressure flow (named *secondary flow*) with an intermediate pressure. A common ejector structure is composed by a *nozzle*, a *suction chamber*, a *mixing section* and a *diffuser*, as shown in Figure 2.1.

Figure 2.1 – A common ejector structure.



Source: Adapted from TEAM Tech AS©.

When passing through the nozzle, the primary flow is accelerated and it creates a low-pressure region at the nozzle exit position. This condition allows the suction of the secondary flow through the suction chamber. Both primary and secondary flows enter the mixing section where they are expected to be completely mixed to ensure the best performance of the ejector. At the mixing section inlet position, the primary and secondary flows have different pressure and velocity profiles, and they become approximately uniform when the mixing is achieved. Inside the mixing section, the primary flow transfers momentum to the secondary flow during the mixing process. When leaving the mixing section, the mixing flow has its final pressure increased by the diffuser.

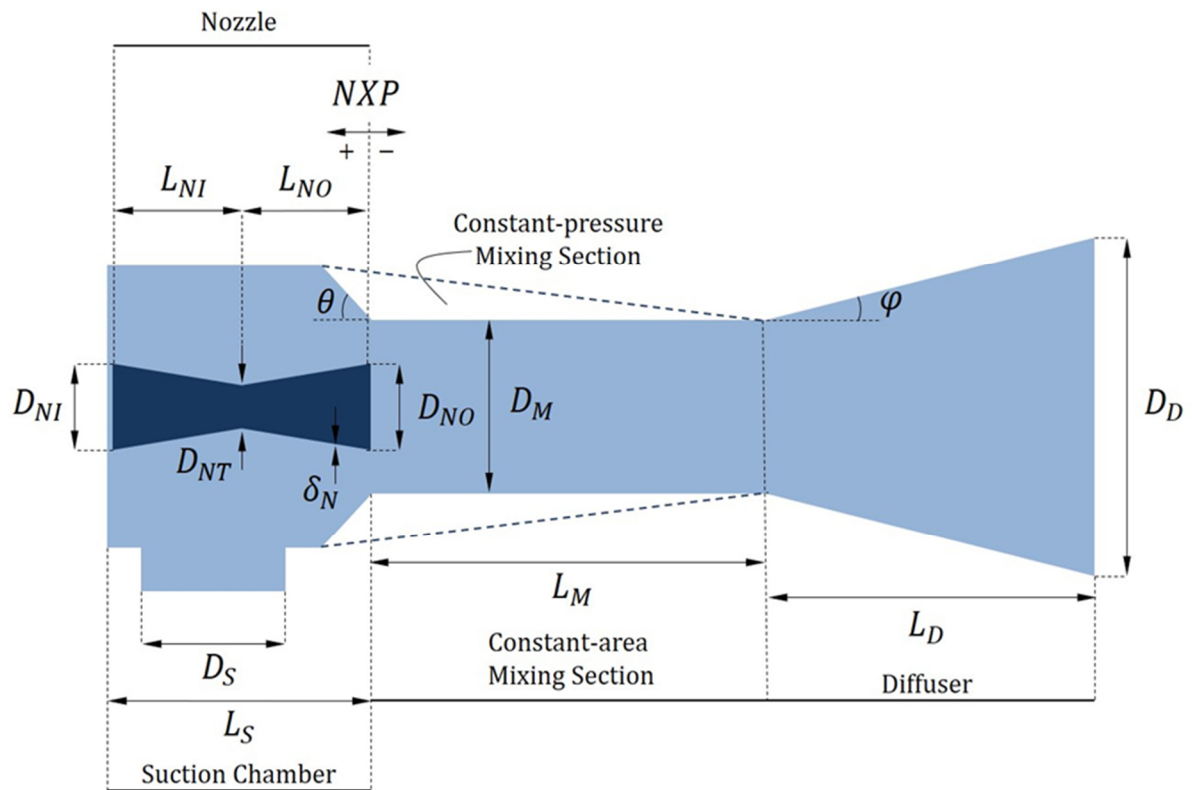
### 2.3 Components of ejectors

In this section, each ejector component (nozzle, suction chamber, mixing section and diffuser) is individually explained. The main geometrical parameters of these components investigated in literature and considered for optimization procedures are shown in Figure 2.2.

In Figure 2.2,  $D_{NI}$  is the nozzle inlet diameter,  $D_{NO}$  is the nozzle outlet diameter,  $D_{NT}$  is the nozzle throat diameter,  $D_S$  is the suction chamber inlet diameter,  $D_M$  is the mixing section diameter,  $D_D$  is the diffuser outlet diameter,  $L_{NI}$  is the nozzle inlet length,  $L_{NO}$  is the nozzle outlet length,  $L_S$  is the suction chamber length,  $L_M$  is the mixing section length,  $L_D$  is the diffuser length,  $\delta_N$  is the nozzle exit thickness,  $\theta$  is the



Figure 2.2 – Main geometrical parameters of ejectors. Geometry recommended for compressible-flow ejectors.



Source: Author.

suction chamber convergent angle,  $\varphi$  is the diffuser divergent angle and  $NXP$  is the distance between the nozzle outlet and the mixing section inlet. By convention,  $NXP$  is positive when it moves away from the mixing section, negative when it enters the mixing section and null when the nozzle outlet coincides with the mixing section inlet

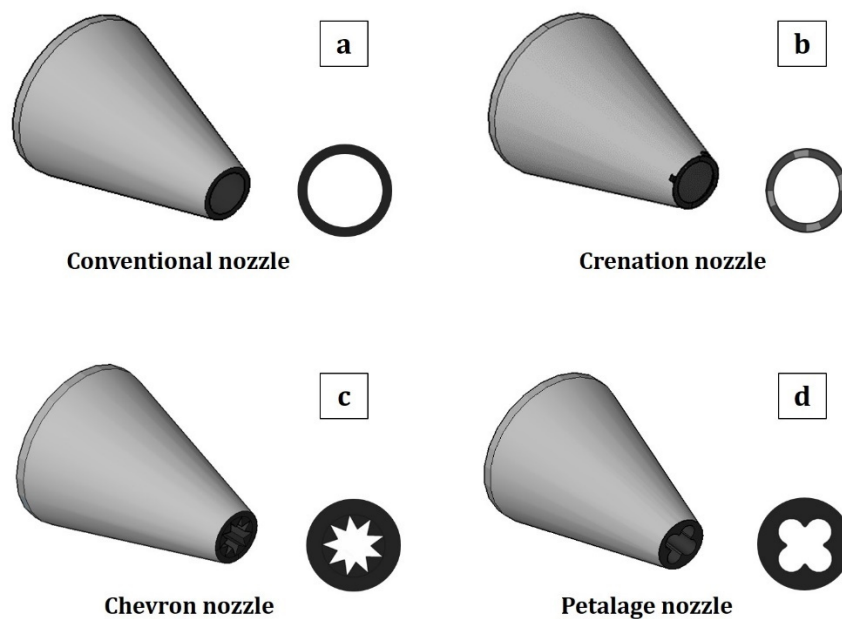
### 2.3.1 Nozzle

Nozzle is a flow passage with varying cross-sectional area in which the velocity of the primary flow is increased in the flow direction (MORAN; SHAPIRO; BOETTNER, 2011). The nozzle characteristics that most affect the ejector performance are its geometry and position in relation to the mixing section entrance (WATANAWANAVET, 2008). Different configurations can be employed for nozzles and their geometry must be chosen so that the ejector efficiency is as higher as possible for a specific operating condition.

For compressible-flow ejectors, it is recommended a convergent-divergent nozzle configuration (the same shown in Figure 2.2), known as *supersonic nozzles*, that contains a throat section which induces a supersonic flow. For incompressible-flow ejectors (i.e. when the flow density does not change in the entire flow), it is suggested a simple convergent nozzle, also called *conventional nozzles*.

The influence of a conventional (Figure 2.3-a), a petalage (Figure 2.3-d) and a crenation (Figure 2.3-b) nozzle on the performance of supersonic ejectors working under the same operating condition was investigated by XUE et al. (2017). In that study, authors concluded that the nozzle geometry affects the entrainment ratio (i.e. the ratio between the volumetric flow rates of the secondary and primary flows), the critical backpressure (i.e. the critical pressure delivered by the diffuser) and the shape of the mixing layer for supersonic ejectors.

Figure 2.3 – Different nozzle configurations.



Source: Author.

A similar study was conducted by KONG et al. (2013), where the influences of a conventional (Figure 2.3-a) and a Chevron (Figure 2.3-c) nozzles on the performance of a supersonic ejector were compared. The authors observed that the Chevron nozzle gives higher entrainment ratio ( $M$ ) and pressure recovery (defined by the authors as the difference between the static pressures at the suction chamber inlet and the diffuser outlet) compared to the conventional configuration.

FU et al. (2016) investigated the influence of the nozzle outlet diameter ( $D_{NO}$ ) and its divergent-section length ( $L_{NO}$ ) on the performance of steam ejectors. The results obtained have revealed that the entrainment ratio significantly increases with the increment in  $D_{NO}$ , and then decreases when  $D_{NO}$  exceeds a specific value.

LONG; HAN; CHEN (2008) observed that the nozzle tip thickness ( $\delta_N$ ) does not significantly affect the ejector performance and it should explain why this parameter is generally ignored in studies related to ejectors geometry. However,  $\delta_N$  exerts great influence on the tip vortex development near the nozzle tip, the distribution of turbulent kinetic energy and the backflows that might occur in some operating conditions.

The nozzle can be fixed or movable inside the ejector and its position (in relation to the mixing section inlet) is defined by the parameter  $NXP$ . Ejectors with movable nozzle provide more flexible operational range compared with a totally fixed nozzle (APHORNRATANA; EAMES, 1997). In addition,  $NXP$  affects the size of recirculation bubble observed in the suction chamber (BAEK et al., 2018), the mixing process between primary and secondary flows and the creation of backflows inside the nozzle due to the dominance of the diffuser outlet pressure (ELHUB et al., 2018).

A special attention should be paid for selecting the best  $NXP$ , ensuring the adequate acceleration of the secondary flow (by the primary flow) inside the mixing section, and reducing friction losses and kinetic energy losses as much as possible during the mixing process (ZHANG et al., 2017).

Optimum  $NXP$  value changes slightly from case to case (FALSAFIOON; AIDOUN; POIRIER, 2017). However, generally, when  $NXP$  is zero (i.e. when the nozzle is positioned exactly at the mixing section entrance), the ejector efficiency (PHITAKWINAI; THEPA; NILNONT, 2016) and its entrainment ratio (WU et al., 2018) peaks are achieved. On the other hand, some authors observed that increasing  $NXP$  will also increase the entrainment ratio (HU et al., 2014; VARGA; OLIVEIRA; DIACONU, 2009).

### **2.3.2 Suction chamber**

*Suction chamber* is the ejector component through which the suction of the secondary flow occurs. For an axisymmetric ejector configuration, the suction chamber and

nozzle are concentric. For a non-axisymmetric geometry, the secondary flow enters the suction chamber through a lateral flow passage (see Figure 2.2).

The geometric parameters considered in the studies of the suction chamber are its diameter ( $D_S$ ), length ( $L_S$ ) and convergent angle ( $\theta$ ). Few works in literature deal with suction chamber investigations. YADAV; PATWARDHAN (2008) studied the influence of  $D_S$  and  $\theta$  on the ejector performance, and concluded that: i) a larger suction chamber may reduce the suction capacity; ii) suction chamber has significant effect on the entrainment ratio; iii) it is recommended a range of  $5^\circ$  to  $15^\circ$  for  $\theta$ .

Effects of  $\theta$  on the ejector performance were also studied by RAMESH; SEKHAR (2018) and the results showed that the optimum  $\theta$  may increase the entrainment ratio for almost 50%, and this parameter has little influence on the backpressure.

### 2.3.3 Mixing section

The region where mixing between both primary and secondary fluids occurs is called *mixing section*, or “ejector throat”. This section is an important component which exerts a considerable influence on the ejector performance (ABDEL-HAMID et al., 2018; LI; LI, 2011). Inside the mixing section, the primary flow (high-pressure flow) transfers momentum to the secondary flow (low-pressure flow) (ARBEL et al., 2003).

Two distinguished concepts of mixing section were introduced by KEENAN (1950): constant-area and constant-pressure (see Figure 2.2); and it remains as theoretical basis for ejector designs until now. In constant-pressure configurations, the cross-sectional area of the mixing section is variable and the static pressure remains constant while the primary and secondary fluids are mixing (ZHANG et al., 2017). Constant-area designs present changes in static pressure along the mixing section length.

Constant-pressure mixing section gives higher efficiency for compressible-flow ejectors, while the constant-area configuration is theoretically better for incompressible-flow ones (KEENAN, 1950). In the constant-pressure configuration, the geometric parameters taken into account are the convergent angle ( $\theta$ ) (the same as the suction chamber’s convergent angle) and the mixing section length ( $L_M$ ). For constant-area designs, the geometrical parameters considered are  $L_M$  and the mixing section diameter ( $D_M$ ).

A properly  $L_M$  should be designed to ensure the complete mixing between the two fluids and to create a uniform velocity profile before the diffuser entrance. SHAH; CHUGHTAI; INAYAT (2013) studied the effects of the mixing section length on the transport process in a steam ejector using three different values for  $L_M$  (110, 130 and 150 mm), and concluded that the lowest length gives the highest entrainment ratio under a specific operating condition. On the other hand, VARGA; OLIVEIRA; DIACONU (2009) found that  $L_M$  has little influence on the entrainment ratio but strong influence on the critical backpressure.

The ejector performance is very sensitive to  $\theta$ , specially near its optimum working point, and the entrainment ratio can significantly vary by changing  $\theta$  (ZHU et al., 2009). PALACZ et al. (2016) conducted an optimization study of the mixing section geometry and their results showed a strong relationship between  $D_M$  and the ejector performance. In addition, according to LIU; GROLL (2008), the higher the  $NXP$ , the lower the mixture effectiveness.

### 2.3.4 Diffuser

*Diffuser* is a flow passage with varying cross-sectional area in which the mixing flow velocity is decreased in the flow direction (MORAN; SHAPIRO; BOETTNER, 2011). The diffuser efficiency is measured by its capacity to increase the ejector return pressure (backpressure). Similar to the mixing section, the flow inside the diffuser is very complex because it involves strong flow interactions, shear forces, turbulent mixing and vorticity (WANG; YU, 2016).

In diffusers, the inlet diameter is the same as the mixing section outlet diameter ( $D_M$ ), since these components are connected. Other geometric parameters that are part of the diffuser's design are its outlet diameter ( $D_D$ ), length ( $L_D$ ) and divergent angle ( $\varphi$ ).

The diffuser efficiency is expected to increase with the increment of the nozzle-throat-to-mixing-section area ratio ( $D_{NT}^2/D_M^2$ ), while decreases with the raise of the pressure ratio (i. e. ratio between the inlet pressure of the primary flow and the inlet pressure of the secondary flow) and entrainment ratio (ZHENG; DENG, 2017). The computational investigations conducted by BANASIAK; HAFNER; ANDRESEN (2012) showed that the larger the  $D_D$ , the better the ejector performance, and the optimum  $\varphi$  is approximately  $3^\circ$  for a specific operating condition and ejector configuration. The diffuser backpressure firstly increases quickly and then slowly as a

function of the diffuser-to-nozzle-inlet area ratio ( $D_D^2/D_{NT}^2$ ), as stated by LIU; GROLL (2008).

## 2.4 Classification of ejectors

The most common classification of ejectors is according to the characteristics of their working fluids. Working fluid is an important parameter to be considered in the selection of the optimal ejector design. The primary flow could be in the liquid or gas state, while the secondary flow could be liquid, gas or a liquid-gas mixture (CUNNINGHAM, 2001):

- a) *Liquid-jet-liquid (LJL) ejectors*: ejectors with both primary and secondary flows in the liquid state;
- b) *Liquid-jet-gas (LJG) ejectors*: ejectors with the primary flow in the liquid state and the secondary flow in the gaseous state;
- c) *Gas-jet-gas (GJG) ejectors*: ejectors with both primary and secondary flows in the gaseous state;
- d) *Liquid-jet-gas-liquid (LJGL) ejectors*: ejectors with the primary flow in the liquid state and the secondary flow is a mixture of liquid and gas.

## 2.5 Ejector modeling

The flow field inside the ejector section is relatively complex, because it may involve turbulence, mixing process, non-uniform velocity and pressure profiles, recirculation, two-phase flow and compressible flow. Although the internal flow field of ejectors is three-dimensional (3D), one-dimensional (1D) mathematical approaches can guide system operation, interpret experimental results, assist in system design and optimization (HE; LI; WANG, 2009), determine the ejector maximum efficiency points (ANTONIO et al., 2012) and predict the ejector performance at critical and subcritical operation modes for compressible model (CHEN et al., 2013). Mathematical approaches that describe the internal flow of ejectors are found in the literature for compressible and incompressible models.

### 2.5.1 Mathematical modeling for compressible-flow ejectors

Based on conservation equations (i.e. mass, energy and momentum conservation laws) and theories associated with mixing and gas dynamics, and the ideal-gases assumption, KEENAN; NEUMANN (1942) were the first authors to propose the ejector theory for compressible flows using a one-dimensional analysis. KEENAN (1950) later modified that model by introducing the two distinguished concepts of mixing section: constant-area and constant-pressure configurations. And it remains as a theoretical basis for ejector designs until now. The authors concluded that the constant-pressure mixing section gives a higher efficiency for compressible-flow ejectors, while the constant-area configuration is theoretically better for incompressible-flow models, as already mentioned in section 2.3.3. The theory proposed by KEENAN (1950) is based on the assumptions that both primary and secondary flows have the same pressure at the mixing section inlet, and mixing is complete in inside the constant-area mixing section. However, that model was valid only for cases when the ejector operates under its critical mode and did not include irreversibility due to friction losses on its formulation.

Later, MUNDAY; BAGSTER (1977) introduced the concept of *effective area* (or *fictive throat*), which is useful to understand the maximum limitations of the ejectors capacity. KORNHAUSER (1990), who used refrigerant R12 in an ejector refrigeration cycle, presented the first 1D and homogeneous mathematical model for a two-phase ejector. HUANG et al. (1999) proposed a 1D mathematical model assuming that the effective area occurs at the constant-area mixing section inlet, and validated it with experimental results. In addition, HUANG et al. (1999) observed that his 1D model was effective to predict the ejector performance when it operates under the critical mode.

GALANIS; SORIN (2016) proposed a 1D mathematical model, which is able to calculate the ejector dimensions by including the ideal gas assumption and considering that the effective area occurs at the nozzle outlet section. CHEN et al. (2013) complemented the model proposed by HUANG et al. (1999) by calculating the ejector performance for both critical and sub-critical modes. A set of references that describe 1D mathematical models for compressible-flow ejectors is widely presented in literature in details (e.g. ASFORA; SANTOS; DUARTE, 2019; CARRILLO; DE LA FLOR; LISSÉN, 2017; EL-DESSOUKY et al., 2002).

### 2.5.2 Mathematical modeling for incompressible-flow ejectors

Although the most of 1D mathematical approaches found in the literature deal with compressible-flow models, some authors have presented useful theories for incompressible-flow ejectors. Probably, the first 1D model for incompressible-flow ejectors was suggested by GOSLINE; O'BRIEN (1934), who proposed the governing equations to represent the fluid dynamics inside ejectors. CUNNINGHAM (1957) later incremented this theory by including friction losses in the mathematical formulation. As cited in WINOTO; LI; SHAH (2000), the model proposed by CUNNINGHAM (1957) was followed by the works of VOGEL, (1956), MUELLER (1964), REDDY; KAR (1968), SANGER (1970), GRUPPING; COPPES; GROOT (1988) and HATZLAVRAMIDIS (1991). WINOTO; LI; SHAH (2000) presented a detailed set of equations for incompressible-flow ejectors, both for the case where primary and secondary fluids are different as for water ejectors (i.e. ejectors whose primary and secondary fluids are water). This model presented a great agreement with experimental results and considers constant values of friction loss coefficients for each ejector component, and it is very useful to conduct preliminary analysis about the ejector performance.

As mentioned before, a 1D mathematical model approximately represents the internal flow of ejectors, because it has a 3D feature in practice. 1D models can be useful for preliminary studies and they should be complemented with other tools to guarantee a better accuracy of the theoretical analysis.

## 2.6 Basics of Computational Fluid Dynamics

The study of the fluid movement has been developed for many centuries. Aristotle (384 – 322 BC) was the first to describe the principle of continuity. Archimedes (287 – 212 BC) defined the buoyancy conditions for a body when immersed in a fluid; Romans built aqueducts to transport water to supply their cities; in the 15<sup>th</sup> century, Leonardo da Vinci (1452 – 1519) proposed solutions to reduce the drag force of vessels in the water; in 1586, Simon Stevin (1548 – 1620) published *Static and Hydrostatic*, accepted as an “encyclopedia” on the fluid mechanics for that time. Leonhard Euler (1707 – 1783) is considered one of the founders of hydrodynamics for publishing the famous *Euler equations*. However, mathematical descriptions of the fluid behavior were only strengthened in the 19<sup>th</sup> century, in the form of the *Navier–Stokes equations*, after the



pioneering works of Claude Navier (1822), Simeon Poisson (1829) and George Stokes (1845) (FORTUNA, 2000). For the Navier–Stokes equations, there is currently an analytical solution for very limited cases. Moreover, whoever analytically presents a general solution to these equations will solve one of the “millennium problems”.

The absence of an analytical solution makes us dependent on numerical methods. For simple problems, a numerical solution can be obtained using only a basic calculator or less. However, problems involving fluid motion are not so simple and a more powerful tool, such as computers, is essential. Computational Fluid Dynamics (CFD) can be defined as the set of methodologies that enable the computer to provide some information about fluid flows through numerical solution (HIRSH, 2007).

For a brief introduction to CFD, it would be necessary to write a book. The purpose of this section is to present a summary of some basic CFD concepts that will be useful to understand the computational procedure employed in this work. The following theoretical aspects have been summarized from HIRSH (2007) with minor adaptations and some other references included, where it contains a more detailed and didactic description of the content presented here for the interested reader.

Fluid mechanics is fundamentally based on conservation laws. A general conservation law enunciates that the variation in the total quantity of a given extensive property within a *domain* is equal to the balance between the quantity of that property which crosses the *boundary surface* of the domain, plus the contributions from any internal sources that generate that quantity.

For an arbitrary volume fixed in space ( $\Omega$ ), also called *control volume*, completely delimited by an arbitrary closed surface ( $S$ ), also known as *control surface*, the integral form of the conservation law for a scalar quantity per unit of volume ( $U$ ) inside  $\Omega$  can be expressed as

$$\frac{\partial}{\partial t} \int_{\Omega} U \, d\Omega + \oint_S \vec{F} \cdot d\vec{S} = \int_{\Omega} Q_V \, d\Omega + \oint_S \vec{Q}_S \cdot d\vec{S} \quad (2.1)$$

and its differential form as

$$\frac{\partial U}{\partial t} + \vec{\nabla} \cdot \vec{F} = Q_V + \vec{\nabla} \cdot \vec{Q}_S \quad (2.2)$$

where  $t$  is the time,  $\vec{F}$  is the flux (i.e. the amount of  $U$  crossing the unit of surface,  $d\vec{S}$ , per unit of time),  $Q_V$  is the volume source (i.e. sum of the external control volume forces per unit of volume),  $\vec{Q}_S$  is the surface source (i.e. forces per unit of volume that cross the control surface) and  $\vec{\nabla}$  is the gradient or divergence operator.

It is important to mention that there are properties (i.e. intensive properties) that do not obey a conservation law (e.g. pressure, temperature, entropy). Fluid dynamics is generally described by the Navier–Stokes equations, that correspond to a set of coupled and nonlinear partial differential equations derived from the basic laws of conservation: mass, momentum and energy (ISKANDARANI, 2010). Mass, momentum and energy conservation equations can be respectively written, in their differential form, as (HIRSH, 2007)

$$\frac{\partial \rho}{\partial t} + \vec{\nabla} \cdot (\rho \vec{v}) = 0 \quad (2.3)$$

$$\frac{\partial \rho \vec{v}}{\partial t} + \vec{\nabla} \cdot (\rho \vec{v} \otimes \vec{v} + p \vec{I} - \vec{\tau}) = \rho \vec{f}_e \quad (2.4)$$

$$\frac{\partial \rho E}{\partial t} + \vec{\nabla} \cdot (\rho \vec{v} H - \kappa \vec{\nabla} T - \vec{\tau} \cdot \vec{v}) = W_f + q_H \quad (2.5)$$

where  $\rho$  is the fluid density,  $\vec{v}$  is the velocity vector,  $\otimes$  denotes the tensor product of the vector quantities  $\rho \vec{v}$  and  $\vec{v}$ ,  $p$  is the pressure,  $\vec{I}$  is the unit tensor,  $\vec{\tau}$  is the viscous shear stress tensor,  $\vec{f}_e$  is the external volume forces per unit mass,  $E$  is the total energy per unit mass (defined as the sum of fluids internal energy and kinetic energy per unit mass),  $H$  is the stagnation or total enthalpy,  $\kappa$  is the thermal conductivity coefficient,  $T$  is the absolute temperature,  $W_f$  is the work of the external volume forces and  $q_H$  is the heat sources other than conduction.

The viscous shear stress tensor ( $\vec{\tau}$ ) is defined as

$$\tau_{ij} = \left[ \mu \left( \frac{\partial v_j}{\partial x_i} + \frac{\partial v_i}{\partial x_j} \right) - \frac{2}{3} (\vec{\nabla} \cdot \vec{v}) \delta_{ij} \right] \quad (2.6)$$

where  $\mu$  is the dynamic viscosity.

The conservation laws for the basic flow quantities (mass –  $\rho$ , momentum –  $\rho \vec{v}$  and energy –  $\rho E$ ) can be written in a compact form (Equation (2.7)), expressing the

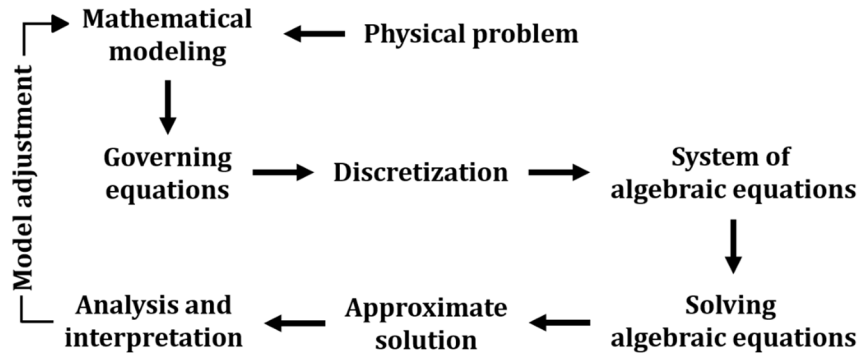
coupled nature of their conservative form and representing the Navier-Stokes equations:

$$\frac{\partial}{\partial t} \begin{bmatrix} \rho \\ \rho \vec{v} \\ \rho E \end{bmatrix} + \vec{\nabla} \cdot \begin{bmatrix} \rho \vec{v} \\ \rho \vec{v} \otimes \vec{v} + p \vec{I} - \vec{\tau} \\ \rho \vec{v} H - \kappa \vec{\nabla} T - \vec{\tau} \cdot \vec{v} \end{bmatrix} = \begin{bmatrix} 0 \\ \rho f_e \\ W_f + q_H \end{bmatrix} \quad (2.7)$$

The computational treatment of the model requires an adequate expression of the equations and domain in which they are valid. As we cannot obtain numerical solutions for continuous regions – due to the infinite points that it presents –, the domain should be *discretized*. The discrete domain through points is called *grid* (or *mesh*) (FORTUNA, 2000).

For the discretized domain, an approximate solution is obtained for the system of algebraic equations constructed for each point (or *element*) of the domain. Finally, the analysis and interpretations of the simulations (called *post processing*) are conducted (see Figure 2.4).

Figure 2.4 – Steps to obtain a numerical solution in fluid flow problems.



Source: Adapted from FORTUNA (2000).

## 2.7 General description of the Finite Element Method (FEM)

After selecting the mathematical model, a suitable discretization method, i.e. a method to approximate the differential equations by a system of algebraic equations for the variables at some set of discrete locations in space and time, should be chosen. The most used approaches used to discretize the domain are finite-difference, finite-volume and finite-elements (FERZIGER; PERIC, 2002). As it will be better explained

further, the present work uses a commercial software of CFD where a discretization algorithm by the finite element method (FEM) is implemented.

In the FEM technique, each geometrical form circumvented by the union of points is called *element* and the unknown field variables are expressed in terms of assumed approximating functions (*interpolating functions* or *shape functions*) within each element. The approximating functions are defined in terms of field variables of specified points (called *nodes* or *nodal points*). Once the field variables of the nodes are found, the field variables at any point can be determined by using the approximating functions (BHAVIKATTI, 2005).

In short, the steps involved in the finite element analysis are (BHAVIKATTI, 2005):

- Selecting suitable fields variables and the elements;
- Discretizing the domain;
- Selecting the approximating functions;
- Finding the element properties;
- Assembling element properties to obtain global properties;
- Imposing the boundary conditions;
- Solving the system of equations to get the nodal unknowns;
- Making additional calculations to obtain the desired values.

## 2.8 Study of ejectors using CFD

The first attempt to study ejectors using CFD technique was in the 1990s. NEVE (1991) is probably the first author registered in the literature who took advantage of CFD results by analyzing the performance of an ejector's diffuser. Later, RIFFAT; GAN; SMITH (1996) observed that the ejector performance strongly depends on the nozzle geometry and the *NXP* parameter by applying the CFD method.

In the last decades, with the advances on mathematical methods and computers, especially with the creation of commercial softwares for CFD, computational simulation results have been presenting more and more accuracy on ejector studies. Several successful cases of CFD simulations applied to ejectors are reported in the literature. KIM et al. (2006) investigated the influence of some geometrical parameters and inlet pressures on the ejector performance. YADAV; PATWARDHAN (2008) studied the effects of the suction chamber geometry on the suction effectiveness of the secondary

flow. ZHU et al. (2009) investigated the influence of the *NXP* parameter and the convergence angle of the mixing section on the ejector performance. PALACZ et al. (2016) conducted an optimization study for the mixing section geometrical parameters in order to increase the coefficient of performance (COP) of a supermarket refrigeration system. LIU et al. (2017) observed that the mixing section efficiency is the most sensitive rather than the individual efficiencies of the nozzle, suction chamber and diffuser.

# Chapter 3

## Methodology

*“The method of science is tried and true. It is not perfect, it’s just the best we have. And to abandon it, with its skeptical protocols, is the pathway to a dark age”.*

*– Carl E. Sagan (1934 – 1996)*

In this work, a quasi-one-dimensional (1D) mathematical approach is employed to perform a theoretical analysis of an incompressible-flow ejector model using data from Computational Fluid Dynamics (CFD) simulations. In this chapter, the computational procedure adopted to conduct the CFD simulations is introduced first and the development of the mathematical approach is presented next.

### **3.1 Computational set up**

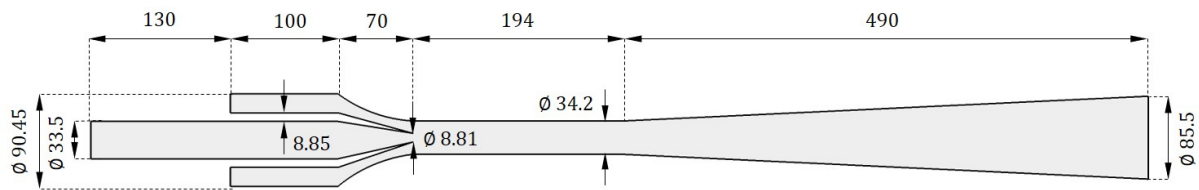
The CFD simulations were carried out using the commercial software COMSOL Multiphysics®, which employs a finite-element discretization scheme to numerically solve the Navier-Stokes equations. The computational set up was built considering the following steps:

- i) Geometry building;
- ii) Material specification;
- iii) Definition of assumptions and boundary conditions;
- iv) Turbulence model definition;
- v) Meshing;
- vi) Simulation running and post processing.

### 3.1.1 Geometry building

A 2D-axisymmetric ejector geometry (Figure 3.1) was built following a similar configuration to that found in SANGER (1968), where experimental data of an incompressible-flow ejector are available. The computational set up was validated by comparing the ejector efficiency curve given as result by CFD simulations with experimental data shared by SANGER (1968).

Figure 3.1 – 2D-axisymmetric ejector geometry used in the computational simulations (dimensions in mm).



Source: Author.

### 3.1.2 Material specification

Both primary and secondary fluids were defined as water at 26.7 °C, and this definition was applied for the entire domain. All the additional properties of water (i.e. dynamic viscosity, density, electrical conductivity, heat capacity at constant pressure, ratio of specific heats, thermal conductivity and speed of sound) were set by default.

### 3.1.3 Definition of assumptions and boundary conditions

The boundary conditions are needed in conjunction with the equations to construct a well-posed mathematical model of a fluid flow (VERSTEEG; MALALASEKERA, 2007).

The CFD simulations were based on the following assumptions:

- Steady-state flow;
- Newtonian fluid;
- Constant viscosity;
- Boussinesq assumption for Reynolds stresses;
- Adiabatic control volume;
- Incompressible flow;
- Negligible body forces.

The *Boussinesq assumption* is a way to treat some relatively simple cases of buoyant flows without the necessity of using a compressible formulation of the Navier–Stokes equations. This approximation assumes that variations in density do not affect the flow field except that they give rise to buoyant forces (COMSOL Multiphysics, 2012).

In Table 3.1, the boundary conditions used for setting up the computational model are exposed. The conditions of normal inflow velocity imposed on the nozzle inlet and diffuser outlet implies the uniformity of the velocity profile on those sections. The same is valid for the suction chamber inlet, but setting the normal inflow pressure instead of velocity at this section. No slip condition assumes a null velocity of the flow in the ejector wall.

Table 3.1 – Values and features of the boundary conditions used in the computational model.

<b>Boundary</b>	<b>Mean field Value/Feature</b>	<b>Turbulent Value/Feature</b>
Nozzle inlet (primary inlet)	Normal velocity equals to 2.0 m/s (1.77×10 <sup>-3</sup> m <sup>3</sup> /s)	$k = \frac{3}{2} (U_0 I_t)^2$
Diffuser outlet	Normal velocity (varying with $M$ )	$\varepsilon = C_\mu^{3/4} \frac{k^{3/2}}{L_t}$
Suction chamber inlet (secondary inlet)	Uniform Pressure (1.03×10 <sup>5</sup> Pa)	$\partial_i k \cdot n_i = 0$ $\partial_i \varepsilon \cdot n_i = 0$
Wall	No slip conditions	wall function (smooth wall)

Source: Author.

Because of the flow complexity, Reynolds-Averaged Navier-Stokes (RANS) equations were employed as a suitable way to achieve a balanced result between accuracy and computational cost. RANS model ignores the turbulent fluctuations and aims at calculating only the turbulent-averaged flow, and it is currently the most widely applied approximation in the CFD practice (HIRSH, 2007).

### 3.1.4 Turbulence model definition

Turbulence occurs in flow situations when the velocity, or more precisely, the Reynolds number (defined as the product of representative scales of velocity and length, divided



by the kinematic viscosity) exceeds a certain critical value (HIRSH, 2007). A turbulence model should be properly selected to allow the capture of the flow characteristics in the entire flow process. In this study, three main turbulence models used in literature for incompressible-flow ejectors were tested:  $k-\varepsilon$ ,  $k-\omega$  and  $k-\omega$  SST. These turbulence models are explained in details in VERSTEEG; MALALASEKERA (2007), and they are summarized below.

### 3.1.4.1 $k-\varepsilon$ turbulence model

In flows where convection and diffusion phenomena significantly affect the differences between production and destruction of turbulence (e.g. in recirculating flows), the dynamics of turbulence should be taken into account.

The standard  $k-\varepsilon$  model (LAUNDER; SPALDING, 1974) has one equation model for the turbulent kinetic energy ( $k$ ) and another one for the rate of viscous dissipation ( $\varepsilon$ ).  $k$  and  $\varepsilon$  are used to define the velocity scale ( $\vartheta$ ) and length scale ( $\ell$ ):

$$\vartheta = \sqrt{k} \quad (3.1)$$

$$\ell = \frac{k^{3/2}}{\varepsilon} \quad (3.2)$$

The standard  $k-\varepsilon$  model uses the following transport equations for  $k$  and  $\varepsilon$ :

$$\frac{\partial(\rho k)}{\partial t} + \frac{\partial(\rho k U_i)}{\partial x_i} = \frac{\partial}{\partial x_j} \left( \frac{\mu_t}{\sigma_k} \frac{\partial k}{\partial x_j} \right) + 2\mu_t S_{ij} \cdot S_{ij} - \rho \varepsilon \quad (3.3)$$

$$\frac{\partial(\rho \varepsilon)}{\partial t} + \frac{\partial(\rho \varepsilon U_i)}{\partial x_i} = \frac{\partial}{\partial x_j} \left( \frac{\mu_t}{\sigma_\varepsilon} \frac{\partial \varepsilon}{\partial x_j} \right) + C_{1\varepsilon} \frac{\varepsilon}{k} 2\mu_t S_{ij} \cdot S_{ij} - C_{2\varepsilon} \rho \frac{\varepsilon^2}{k} \quad (3.4)$$

The eddy viscosity ( $\mu_t$ ) is specified as follows:

$$\mu_t = \rho C_\mu \frac{k^2}{\varepsilon} \quad (3.5)$$

where  $\rho$  is the density.  $\sigma_k$  and  $\sigma_\varepsilon$  are dimensionless parameters named Prandtl's numbers with constant values of 1.00 and 1.30, respectively.  $C_{1\varepsilon}$ ,  $C_{2\varepsilon}$  and  $C_\mu$  are also dimensionless parameters with constant values of 1.44, 1.92 and 0.09, respectively.

In words, Equations (3.3) and (3.4) could be interpreted as:

$$\left[ \begin{array}{c} \text{Rate of} \\ \text{change} \\ \text{of } k \text{ or } \varepsilon \end{array} \right] + \left[ \begin{array}{c} \text{Transport of} \\ k \text{ or } \varepsilon \text{ by} \\ \text{convection} \end{array} \right] = \left[ \begin{array}{c} \text{Transport of} \\ k \text{ or } \varepsilon \text{ by} \\ \text{diffusion} \end{array} \right] + \left[ \begin{array}{c} \text{Rate of} \\ \text{production} \\ \text{of } k \text{ or } \varepsilon \end{array} \right] - \left[ \begin{array}{c} \text{Rate of} \\ \text{destruction} \\ \text{of } k \text{ or } \varepsilon \end{array} \right]$$

The diffusivities of  $k$  and  $\varepsilon$  are connected to the eddy viscosity by  $\sigma_k$  and  $\sigma_\varepsilon$ . Production and destruction of the turbulent kinetic energy are always linked, and the dissipation rate  $\varepsilon$  is large when  $k$  production is also large. In Equation (3.4), it is assumed that the terms related to production and destruction of  $\varepsilon$  are proportional to the terms related to production and destruction of  $k$  in Equation (3.5). This assumption ensures that  $\varepsilon$  increases rapidly if  $k$  also increases fast in order to avoid negative values of  $k$ , which would be physically incoherent. Dimensionless constants  $C_{1\varepsilon}$  and  $C_{2\varepsilon}$  allow the correct proportionality between the terms in Equations (3.4) and (3.5).

### 3.1.4.2 $k$ - $\omega$ turbulence model

The rate of dissipation of  $\varepsilon$  is not the only possible length-scale determining variable. The most prominent alternative is to use the turbulence frequency ( $\omega$ ) as the second variable in addition to  $k$  (WILCOX, 1988, 1993a, 1993b, 1994).

The turbulence frequency ( $\omega$ ) is defined as

$$\omega = \frac{\varepsilon}{k} \quad (3.6)$$

Thus, the alternative length scale ( $\ell$ ) is

$$\ell = \frac{\sqrt{k}}{\omega} \quad (3.7)$$

And the eddy viscosity ( $\mu_t$ ) is given by

$$\mu_t = \frac{\rho k}{\omega} \quad (3.8)$$

The transport equations for  $k$  and  $\omega$  for high Reynolds number are expressed as follows:

$$\frac{\partial(\rho k)}{\partial t} + \frac{\partial(\rho k U_i)}{\partial x_i} = \frac{\partial}{\partial x_j} \left[ \left( \mu + \frac{\mu_t}{\sigma_k} \right) \frac{\partial k}{\partial x_j} \right] + P_k - \beta^* \rho k \omega \quad (3.9)$$

$$\begin{aligned} \frac{\partial(\rho \omega)}{\partial t} + \frac{\partial(\rho \omega U_i)}{\partial x_i} &= \\ &= \frac{\partial}{\partial x_j} \left[ \left( \mu + \frac{\mu_t}{\sigma_\omega} \right) \frac{\partial \omega}{\partial x_j} \right] + \gamma_1 \left( 2\rho S_{ij} \cdot S_{ij} - \frac{2}{3} \rho \omega \frac{\partial U_i}{\partial x_j} \delta_{ij} \right) - \beta_1 \rho \omega^2 \end{aligned} \quad (3.10)$$

where

$$P_k = 2\mu_t S_{ij} \cdot S_{ij} - \frac{2}{3} \rho k \frac{\partial U_i}{\partial x_j} \delta_{ij} \quad (3.11)$$

is the rate of production of turbulent kinetic energy, and  $\sigma_k$ ,  $\sigma_\omega$ ,  $\gamma_1$ ,  $\beta_1$  and  $\beta^*$  are dimensionless parameters with constant values of 2.0, 2.0, 0.553, 0.075 and 0.09, respectively.

In words, Equations (3.9) and (3.10) could be interpreted as:

$$\left[ \begin{array}{c} \text{Rate of} \\ \text{change} \\ \text{of } k \text{ or } \omega \end{array} \right] + \left[ \begin{array}{c} \text{Transport of} \\ k \text{ or } \omega \text{ by} \\ \text{convection} \end{array} \right] = \left[ \begin{array}{c} \text{Transport of} \\ k \text{ or } \omega \text{ by} \\ \text{turbulent diffusion} \end{array} \right] + \left[ \begin{array}{c} \text{Rate of} \\ \text{production} \\ \text{of } k \text{ or } \omega \end{array} \right] - \left[ \begin{array}{c} \text{Rate of} \\ \text{dissipation} \\ \text{of } k \text{ or } \omega \end{array} \right]$$

Integration to the wall does not require wall-damping functions in low-Reynolds number application in the  $k$ - $\omega$  model. The value of  $k$  is zero and  $\omega$  tend to infinity at the wall. Former experiences with this model have shown that the results do not depend significantly on the precise details of the wall treatment. The values of  $k$  and  $\omega$  must be specified at the inlet boundaries and the usual zero gradient conditions are employed for the outlet boundaries.

The most problematic application of this model is for a free stream case, where the turbulent kinetic energy and turbulence frequency tend to zero. In Equation (3.8) it is observed that  $\mu_t$  is indeterminate or infinite as  $\omega \rightarrow 0$ , thus a small non-zero value of  $\omega$  must be specified.

### 3.1.4.3 $k-\omega$ SST turbulence model

The unsatisfactory near-wall performance of the  $k-\varepsilon$  model for boundary layers with adverse pressure gradients was observed by MENTER (1992a), who suggested two procedures to overcome this limitation: i) transforming the  $k-\varepsilon$  model into  $k-\omega$  model in the near-wall region; and ii) applying the standard  $k-\varepsilon$  model in the complete turbulent region far from the wall (MENTER, 1992a, 1992b, 1994, 1997).

In  $k-\omega$  SST model,  $k$  equation is the same as in  $k-\omega$  model, but the  $\varepsilon$  equation is transformed by substituting  $\varepsilon = k\omega$ . This becomes

$$\begin{aligned} \frac{\partial(\rho\omega)}{\partial t} + \frac{\partial(\rho\omega U_i)}{\partial x_i} = \frac{\partial}{\partial x_j} \left[ \left( \mu + \frac{\mu_t}{\sigma_{\omega,1}} \right) \frac{\partial\omega}{\partial x_j} \right] + \gamma_2 \left( 2\rho S_{ij} \cdot S_{ij} - \frac{2}{3}\rho\omega \frac{\partial U_i}{\partial x_j} \delta_{ij} \right) - \\ -\beta_2\rho\omega^2 + +2\frac{\rho}{\sigma_{\omega,2}} \frac{\partial k}{\omega} \frac{\partial\omega}{\partial x_k} \end{aligned} \quad (3.12)$$

where  $\sigma_k$ ,  $\sigma_{\omega,1}$ ,  $\sigma_{\omega,2}$ ,  $\gamma_2$ ,  $\beta_2$  and  $\beta^*$  are dimensionless parameters with constant values of 1.0, 2.0, 1.17, 0.44, 0.083, 0.09, respectively.

In comparison with Equation (3.10), Equation (3.12) contains an additional source term (the second one on its right-hand side), named *cross-diffusion term*, which arises from the  $\varepsilon = k\omega$  transformation of the diffusion term in the  $\varepsilon$  equation.

A good performance of the eddy viscosity of the  $k-\omega$  SST model is limited to flows with adverse pressure gradients and wake regions, and the  $k$  production is limited to avoid the turbulence build-up in stagnation regions. The limiters of the model are:

$$\mu_t = \frac{a_1\rho k}{\max(a_1, \omega, SF_2)} \quad (3.13)$$

$$P_k = \min \left( 10\beta^* \rho k \omega, 2\mu_t S_{ij} \cdot S_{ij} - \frac{2}{3}\rho k \frac{\partial U_i}{\partial x_j} \delta_{ij} \right) \quad (3.14)$$

where  $S = \sqrt{2S_{ij}S_{ij}}$ ,  $a_1$  is a constant and  $F_2$  is a blending function.

In the computational set up, turbulence scale for the primary inlet ( $\ell_p$ ) and turbulence scale for the secondary inlet ( $\ell_s$ ) were set, respectively, as  $0.07 \times D_{NI}$  and

$0.07 \times (D_S - D_{NI} - \text{nozzle thickness})$ .  $D_{NI}$  and nozzle thickness were subtracted from  $D_S$  in order to apply  $\ell_S$  only to the flow passage of the secondary inlet.

### 3.1.5 Meshing

As already mentioned before, the algebraic equations of fluid flows are solved for each *element* that composes the *mesh* of the discretized domain. The approximate solution, as the name already tell us, is not exact and it is provided with errors due to the use of approximations for the various terms in the equations and the imposition of the boundary conditions (FERZIGER; PERIC, 2002).

In this work, a mesh refinement study was conducted for the three turbulence models ( $k-\varepsilon$ ,  $k-\omega$  and  $k-\omega$  SST) in order to minimize the dependence of the approximate solution in relation to the number of elements of the mesh. The mesh refinement study was performed using an *automatic* function for mesh generation available at COMSOL Multiphysics® for the  $k-\omega$  and  $k-\omega$  SST models, and an *adaptive mesh refinement* function for the  $k-\varepsilon$  model. The adaptive mesh function adds mesh elements based on an error criterion to resolve those areas where the error is large (COMSOL Multiphysics, 2012).

### 3.1.6 Simulation running and postprocessing

After running the simulation, the postprocessing step consists on extract data of interest. In this case, average pressure and average velocity data were extracted from CFD simulations for specific ejector sections to be used as input parameters in the mathematical model. In addition, the pressure and velocity profiles at the same sections were plotted in order to allow the evaluation of the flow behavior inside the ejector components.

## 3.2 Mathematical modeling

By applying conservation equations (mass, energy and momentum), a quasi-1D mathematical model (adapted from (WINOTO; LI; SHAH, 2000)) was used to calculate the friction loss coefficients of each ejector component (nozzle, suction chamber, mixing section and diffuser), to predict the ejector maximum efficiency point (or efficiency peak) and to determine the maximum theoretical efficiency that the

ejector can achieve (envelope of operation). “Quasi” is a characteristic attributed to this 1D model because the cross-sectional areas of some ejector components in the direction of flow are not constant. If the cross-sectional area of a duct varies in the direction of flow, it should be treated as a three-dimensional flow. But if these variations of cross-sectional area are smooth and gradual, then we may reasonably assume that there are no significant variations in the stream directions. However, such flow may be called as quasi-1D flow and it can reasonably be modeled by a quasi-1D mathematical model.

The mathematical approach found in WINOTO; LI; SHAH (2000) assumes that pressures of the primary and secondary flows at the mixing section inlet have the same value ( $P_o$ ). This assumption enables to express the ejector pressure recovery ratio ( $N$ ) as a function independent of pressure and velocity data. It is very useful for situations where pressure and velocity data are unknown, and where only some geometrical parameters are known, as well as in practical experiments.

The original model (WINOTO; LI; SHAH (2000)) was adapted considering that pressure of the primary flow at the nozzle outlet ( $P_n$ ) and pressure of the secondary flow at the suction chamber outlet ( $P_v$ ) have different values at the mixing section inlet, what in fact occurs in practice. Considering different pressures at the mixing section inlet may provide more reliable results when pressure and velocity data are available, as well as in results generated by CFD simulations. This assumption considered in the adapted model significantly affects the calculation of the ejector friction loss coefficients, as will be further discussed.

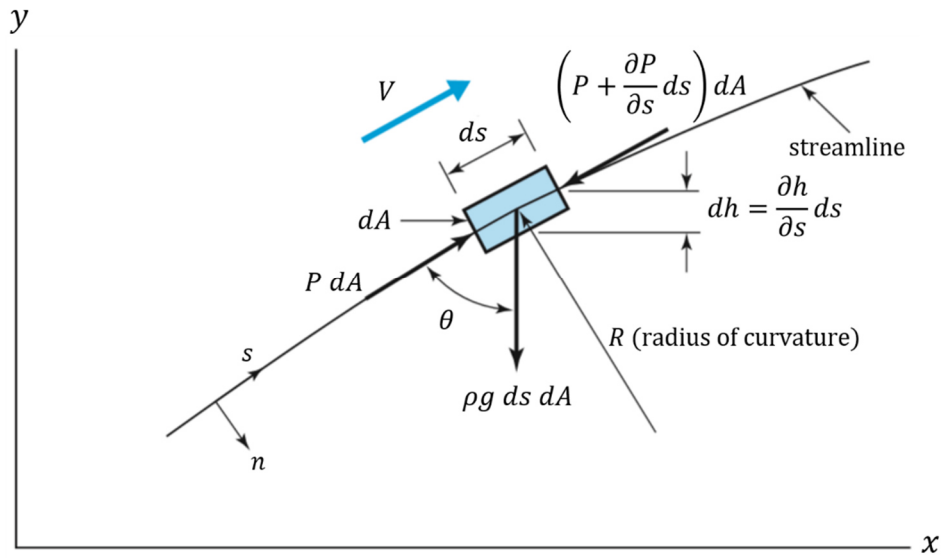
### 3.2.1 The Bernoulli equation

Let us consider an infinitesimal cylindrical particle moving along a streamline, with length  $ds$  and cross-sectional area  $dA$ , as shown in Figure 3.2. The forces acting on the particle in the direction of motion ( $s$ -direction) are due to the pressures,  $P dA$  and  $\left(P + \frac{\partial P}{\partial s} ds\right) dA$ , and due to the  $s$ -direction component of weight,  $\rho g ds dA \cos \theta$ .

The Newton’s second law for the fluid particle is given as (POTTER; WIGGERT; RAMADAN, 2010)

$$P dA - \left(P + \frac{\partial P}{\partial s} ds\right) dA - \rho g ds dA \cos \theta = \rho ds dA a_s \quad (3.15)$$

Figure 3.2 – Particle moving along a streamline.



Source: Adapted from POTTER; WIGGERT; RAMADAN (2010).

where  $g$  is the gravity and  $a_s$  is the acceleration of the particle in the  $s$ -direction represented by

$$a_s = V \frac{\partial V}{\partial s} + \frac{\partial V}{\partial t} \quad (3.16)$$

For a steady-state flow,  $\partial V / \partial t = 0$ . Also, we can define by geometry

$$dh = ds \cos \theta = \frac{\partial h}{\partial s} ds \quad (3.16)$$

So,

$$\cos \theta = \frac{\partial h}{\partial s} \quad (3.17)$$

Dividing all terms in Equation (3.15) by  $ds dA$ , substituting the relations given by Equations (3.16) and (3.17), we obtain for a steady-state flow

$$-\frac{\partial P}{\partial s} - \rho g \frac{\partial h}{\partial s} = \rho V \frac{\partial V}{\partial s} \quad (3.18)$$

Note that:

$$V \frac{\partial V}{\partial s} = \frac{\partial \left( \frac{V^2}{2} \right)}{\partial s} \quad (3.19)$$

Now, for an incompressible flow, where it is assumed a constant density, Equation (3.18) can be written as

$$\frac{\partial}{\partial s} \left( \frac{V^2}{2} + \frac{P}{\rho} + gh \right) = 0 \quad (3.20)$$

Along a streamline, this is satisfied if

$$\frac{V^2}{2} + \frac{P}{\rho} + gh = \text{constant} \quad (3.21)$$

where the constant may assume different value on a distinct streamline. Between two points (1 and 2) on the same streamline, Equation (3.21) becomes

$$\frac{V_1^2}{2} + \frac{P_1}{\rho} + gz_1 = \frac{V_2^2}{2} + \frac{P_2}{\rho} + gz_2 \quad (3.22)$$

where  $z$  is the position of the fluid particle in relation to a fixed reference frame.

Equation (3.22) is known as Bernoulli equation, named after Daniel Bernoulli (1700 – 1782), and is valid for the following assumptions (POTTER; WIGGERT; RAMADAN, 2010):

- Steady-state flow;
- No shear stress (inviscid flow);
- Flow along a streamline;
- Incompressible flow (constant density);
- Average values of pressure and velocity are considered in ejector cross-sections;
- Inertial reference frame.

### 3.2.2 Friction losses

Neglecting shear stresses means that viscous effects are not taken into consideration in the energy conservation formulation. In internal flows, shear stresses caused by friction between the fluid flow and the device inner wall result in energy losses. These



energy losses can be included in the Bernoulli equation by the Darcy–Weisbach (1803 – 1858) (1806 – 1871) relation, written in terms of *head losses* ( $h_L$ ), namely,

$$h_L = f \frac{L}{D} \frac{V^2}{2g} \quad (3.23)$$

where  $f$  is the friction factor,  $L$  is the pipe length,  $D$  is the pipe diameter, and  $V$  is the velocity of the flow inside the pipe.

Multiplying the definition of  $h_L$  by  $g$ , introducing the *friction loss coefficient* ( $K$ ),  $K = f(L/D)$ , and including Equation (3.23) into Equation (3.22) we obtain

$$\frac{P_1}{\rho} + \frac{V_1^2}{2} + gz_1 = \frac{P_2}{\rho} + \frac{V_2^2}{2} + gz_2 + K \frac{V^2}{2} \quad (3.24)$$

Finally, multiplying all terms in Equation (3.24) by  $\rho$ , we have

$$P_1 + \rho \frac{V_1^2}{2} + \rho gz_1 = P_2 + \rho \frac{V_2^2}{2} + \rho gz_2 + K\rho \frac{V^2}{2} \quad (3.25)$$

### 3.2.3 Mathematical model for incompressible-flow ejectors

Equation (3.25) is applied for the nozzle, suction chamber and diffuser, and momentum flux equation (based on the Newton's second law) for the mixing section to estimate their respective friction loss coefficients. For the ejector, the following assumptions are considered in the mathematical formulation:

- Steady-state flow;
- Variations of gravitational potential energy between the ejector inlets and outlet sections are neglected;
- Average values of pressure and velocity are considered in ejector cross-sections;
- Both primary and secondary fluids are the same with incompressible flows (water was chosen as working fluid  $\rightarrow \rho = 998.2 \text{ kg/m}^3 \equiv \text{constant}$ );
- The distance between nozzle outlet and mixing section inlet ( $NXP$ ) is zero;
- Mixing section follows a constant-area configuration;
- Mixing flow inside the mixing section is one-dimensional (1D);
- Mixing between both primary and secondary flows is complete inside the mixing section.

The mathematical formulation (WINOTO; LI; SHAH, 2000) considers some dimensionless parameters, such as: the entrainment ratio ( $M$ ), nozzle-to-mixing-section area ratio ( $R$ ) and mixing-section-to-diffuser area ratio ( $a$ ). These parameters are defined as

$$M = \frac{Q_2}{Q_1} \quad (3.26)$$

$$R = \frac{A_{NO}}{A_M} \quad (3.27)$$

$$a = \frac{A_M}{A_D} \quad (3.28)$$

where  $Q_1$  is the volumetric flow rate of the primary flow,  $Q_2$  is the volumetric flow rate of the secondary flow,  $A_{NO}$  is the cross-sectional area of the nozzle outlet,  $A_M$  is the cross-sectional area of the mixing section and  $A_D$  is the cross-section area of the diffuser outlet.

Applying the Equation (3.25) for the nozzle (from position  $i$  to  $n$  in Figure 3.3), we obtain

$$P_i + \rho \frac{V_{1i}^2}{2} = P_n + \rho \frac{V_{1n}^2}{2} + K_N \rho \frac{V_{1n}^2}{2} \quad (3.29)$$

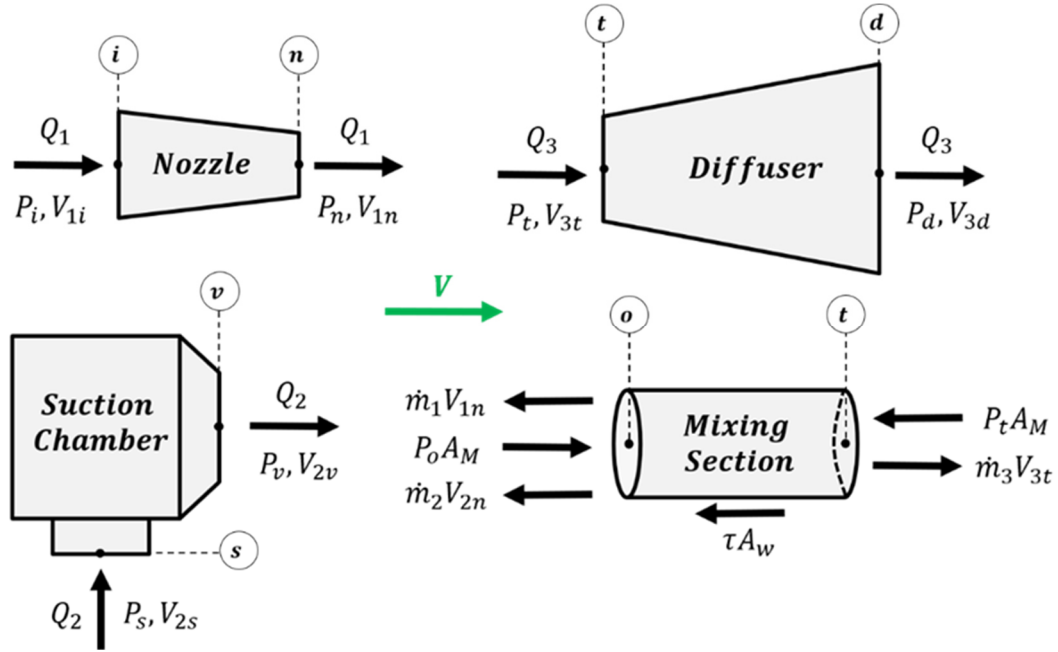
where  $P_i$  is the static pressure at the nozzle inlet,  $P_n$  is the static pressure at the nozzle outlet,  $\rho$  is the density of water,  $V_{1i}$  is the velocity of the primary flow at the nozzle inlet,  $V_{1n}$  is the velocity of the primary flow at the nozzle outlet and  $K_N$  is the friction loss coefficient of the nozzle.

Substituting the definition of total pressure of the primary flow at the nozzle inlet ( $\bar{P}_i$ ),  $\bar{P}_i = P_i + \rho(V_{1i}^2/2)$ , in Equation (3.29), the nozzle equation becomes

$$\bar{P}_i = P_n + \rho \frac{V_{1n}^2}{2} (1 + K_N) \quad (3.30)$$

For the suction chamber (from position  $s$  to  $v$  in Figure 3.3), Equation (3.25) can be written as

Figure 3.3 – Ejector components with respective parameters considered in each cross-section.



Source: Author.

$$P_s + \rho \frac{V_{2s}^2}{2} = P_v + \rho \frac{V_{2v}^2}{2} + K_S \rho \frac{V_{2v}^2}{2} \quad (3.31)$$

where  $P_s$  is the static pressure at the suction chamber inlet,  $P_v$  is the static pressure at the suction chamber outlet,  $V_{2s}$  is the velocity of the secondary flow at the suction chamber inlet,  $V_{2v}$  is the velocity of the secondary flow at the suction chamber outlet and  $K_S$  is the friction loss coefficient of the suction chamber.

Substituting the total pressure at the suction chamber inlet ( $\bar{P}_s$ ),  $\bar{P}_s = P_s + \rho(V_{2s}^2/2)$ , in Equation (3.31), the suction chamber equation becomes

$$\bar{P}_s = P_v + \rho \frac{V_{2v}^2}{2} (1 + K_S) \quad (3.32)$$

Momentum flux coupled with mass conservation equation for the mixing section (from position  $o$  to  $t$  in Figure 3.3) is

$$(\dot{m}_1 + \dot{m}_2)V_{3t} - \dot{m}_1 V_{1n} - \dot{m}_2 V_{2v} = (P_o - P_t)A_M - \tau A_w \quad (3.33)$$

where  $\dot{m}_1$  is the mass flow rate of the primary flow,  $\dot{m}_2$  is the mass flow rate of the secondary flow,  $V_{3t}$  is the velocity of the mixing flow at the mixing section outlet,  $P_o$  is

the static pressure at the mixing section inlet,  $P_t$  is the static pressure at the mixing section outlet,  $\tau$  is the shear stress and  $A_w$  is the inner wall area of the mixing section.

Dividing all terms from Equation (3.33) by  $A_M$ , substituting the definitions of friction loss,  $\tau(A_w/A_M) = K_M\rho(V_{3t}^2/2)$ , mass flow rate,  $\dot{m} = \rho VA$ , and  $R$ , it can be written as

$$P_o - P_t = \rho \left\{ [V_{1n}R + V_{2v}(1-R)]V_{3t} - V_{1n}^2R - V_{2v}^2(1-R) + K_M \frac{V_{3t}^2}{2} \right\} \quad (3.34)$$

where  $K_M$  is the friction loss coefficient of the mixing section.

Applying Equation (3.25) for the diffuser (from position  $t$  to  $d$  in Figure 3.3), it results in

$$P_t + \rho \frac{V_{3t}^2}{2} = P_d + \rho \frac{V_{3d}^2}{2} + K_D \rho \frac{(V_{3t} - V_{3d})^2}{2} \quad (3.35)$$

where  $P_d$  is the static pressure at the diffuser outlet,  $V_{3d}$  is the velocity of the mixing flow at the diffuser outlet and  $K_D$  is the friction loss coefficient of the diffuser.

Substituting the total pressure at the diffuser outlet ( $\bar{P}_D$ ),  $\bar{P}_D = P_D + \rho(V_{3d}^2/2)$ , in Equation (3.35), the diffuser equation turns

$$\bar{P}_d = P_t + \frac{\rho}{2} [V_{3t}^2 - K_D(V_{3t} - V_{3d})^2] \quad (3.36)$$

For mass conservation from position  $t$  to  $d$ , we have

$$V_{3d} = V_{3t}a \quad (3.37)$$

If we expand the term  $(V_{3t} - V_{3d})^2$  in Equation (3.6), put  $V_{3t}$  in evidence and replace  $V_{3d}$  with  $V_{3t}a$ , we obtain

$$\bar{P}_d = P_t + \frac{\rho}{2} V_{3t}^2 [1 - K_D(a - 1)^2] \quad (3.38)$$

Ejector pressure recovery ratio ( $N$ ) is a dimensionless parameter which is expressed in terms of total pressures at the nozzle inlet, suction chamber inlet and diffuser outlet. It can be defined as

$$N = \frac{\bar{P}_d - \bar{P}_s}{\bar{P}_i - \bar{P}_d} \quad (3.39)$$

Applying the assumption used by WINOTO; LI; SHAH (2000), which considers that the static pressures at the nozzle outlet ( $P_n$ ) and suction chamber outlet ( $P_v$ ) have the same value at the mixing section inlet ( $P_o$ ),  $N$  can be also expressed as

$$N = \frac{2R + \frac{2M^2R^2}{1-R} - [1 + K_M + (1-a)^2K_D]R^2(1+M)^2 - (1+K_S)\frac{M^2R^2}{(1-R)^2}}{1 + K_N - 2R - \frac{2M^2R^2}{1-R} + [1 + K_M + (1-a)^2K_D]R^2(1+M)^2} \quad (3.40)$$

The theoretical ideal equation for the pressure recovery ratio ( $N_{ideal}$ ) is obtained by assuming all friction loss coefficients equal to zero in Equation (3.40). Thus, it turns

$$N_{ideal} = \frac{2R + \frac{2M^2R^2}{1-R} - R^2(1+M)^2 - \frac{M^2R^2}{(1-R)^2}}{1 - 2R - \frac{2M^2R^2}{1-R} + R^2(1+M)^2} \quad (3.41)$$

The ejector efficiency ( $\eta$ ) can be defined as the ratio of energy transferred to the secondary flow to energy available from primary flow (EL GAZZAR; MEAKHAIL; MIKHAIL, 2006), and it can be written as

$$\eta = M \times N \quad (3.42)$$

Finally, the theoretical ideal efficiency ( $\eta_{ideal}$ ), which represents the maximum efficiency that the ejector can achieve (envelope of operation), is defined as

$$\eta_{ideal} = M \times N_{ideal} \quad (3.43)$$

### 3.2.4 Pressure correction factor ( $\gamma$ )

If the assumption of uniform pressure profile at the cross-sections is not acceptable for a specific situation, the properly pressure distribution can be accounted by applying a *pressure correction factor* ( $\gamma$ ) in the pressure data. Its definition comes from the first law of thermodynamics, which can be expressed as (POTTER; WIGGERT; RAMADAN, 2010)

$$\dot{Q} - \dot{W} = \frac{D}{Dt} \int_{sys} e \rho dV \quad (3.44)$$

where  $\dot{Q}$  is the rate-of-heat transfer term,  $\dot{W}$  is the work-rate term,  $e$  is the specific energy (which includes terms of specific-kinetic energy, specific-potential energy and specific-internal energy),  $V$  is the volume and  $D/Dt$  is called *material derivative*, used for a *Lagrangian* description in terms of a fixed collection of material particles.

The work-rate term in Equation (3.44) may be divided into four other work contributions as follows

$$\dot{W} = \int_S p \hat{n} \cdot \mathbf{V} dA + \dot{W}_S + \dot{W}_{shear} + \dot{W}_I \quad (3.45)$$

where  $\int_S p \hat{n} \cdot \mathbf{V} dA$  is the *flow work* resulting from the forces due to pressure moving at the control surface,  $\dot{W}_S$  is the work rate resulting from rotating shafts of mechanical machines,  $\dot{W}_{shear}$  is the work rate due to the shear acting on a moving boundary, and  $\dot{W}_I$  is the work rate that occurs when the control volume moves relatively to a fixed reference frame.

Pressure for sections with non-uniform profiles can be properly expressed by using the definition of *flow work*,  $\int_S p \hat{n} \cdot \mathbf{V} dA$ . Note that this term represents the pressure distribution over the cross-sectional area  $A$ . We can define the pressure correction factor ( $\gamma$ ) as

$$\gamma = \frac{\int_S p \hat{n} \cdot \mathbf{V} dA}{P V A} \quad (3.46)$$

where  $p$  and  $\mathbf{V}$  correspond to the pressure and velocity functions over an area element  $dA$ , and  $\hat{n}$  denotes the unit vector pointing outward  $dA$  in numerator. Denominator corresponds to the product between average value of  $P$ , average value of  $V$  and  $A$ . Average  $P$  and  $V$  are given as result by CFD simulations and evaluated for each ejector section of interest ( $i, n, s, v, o, t$  and  $d$ ) showed in Figure 3.3.

### 3.2.5 Kinetic-energy correction factor ( $\alpha$ )

Following the same principle of  $\gamma$ , the properly velocity in non-uniform distributions can be accounted for by introducing the kinetic-energy correction factor ( $\alpha$ ), defined by (POTTER; WIGGERT; RAMADAN, 2010)

$$\alpha = \frac{\int V^3 dA}{V^3 A} \quad (3.47)$$

### 3.2.6 Equations with corrected factors

The correction factors  $\gamma$  and  $\alpha$  were applied for five sections: nozzle inlet (position  $i$ ), nozzle outlet (position  $n$ ), suction chamber inlet (position  $s$ ), mixing section outlet (position  $t$ ) and diffuser outlet (position  $d$ ) (see Figure 3.3). So, Equations (3.30), (3.32) and (3.38) can be rewritten, on their respective corrected form, as

$$\bar{P}_i' = \gamma_n P_n + \alpha_n \rho \frac{V_{1n}^2}{2} (1 + K_N') \quad (3.48)$$

$$\bar{P}_s' = P_v + \rho \frac{V_{2v}^2}{2} (1 + K_S') \quad (3.49)$$

$$\bar{P}_d' = \gamma_t P_t + \rho \frac{V_{3t}^2}{2} [\alpha_t - K_D' \alpha_d (a - 1)^2] \quad (3.50)$$

where  $\bar{P}_i'$ ,  $\bar{P}_s'$  and  $\bar{P}_d'$  are the total pressures corrected by  $\gamma$  and  $\alpha$  at the nozzle inlet, suction chamber inlet and diffuser outlet, respectively, that are also expressed as follows

$$\bar{P}_i' = \gamma_i P_i + \alpha_i \rho \frac{V_{1i}^2}{2} \quad (3.51)$$

$$\bar{P}_s' = \gamma_s P_s + \alpha_s \rho \frac{V_{2s}^2}{2} \quad (3.52)$$

$$\bar{P}_d' = \gamma_d P_d + \alpha_d \rho \frac{V_{3d}^2}{2} \quad (3.53)$$

and  $K_N'$ ,  $K_S'$  and  $K_D'$  are the new friction loss coefficients that include the correction factors.



# Chapter 4

## Results and Discussion

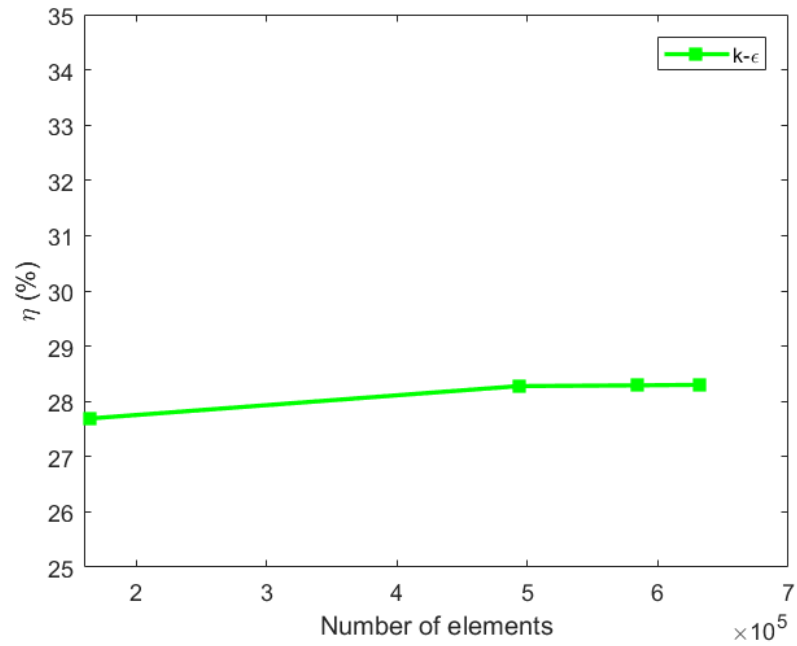
*“Science is man’s progressive approach to the real world”.*

*– Max K. E. L. Planck (1858 – 1947)*

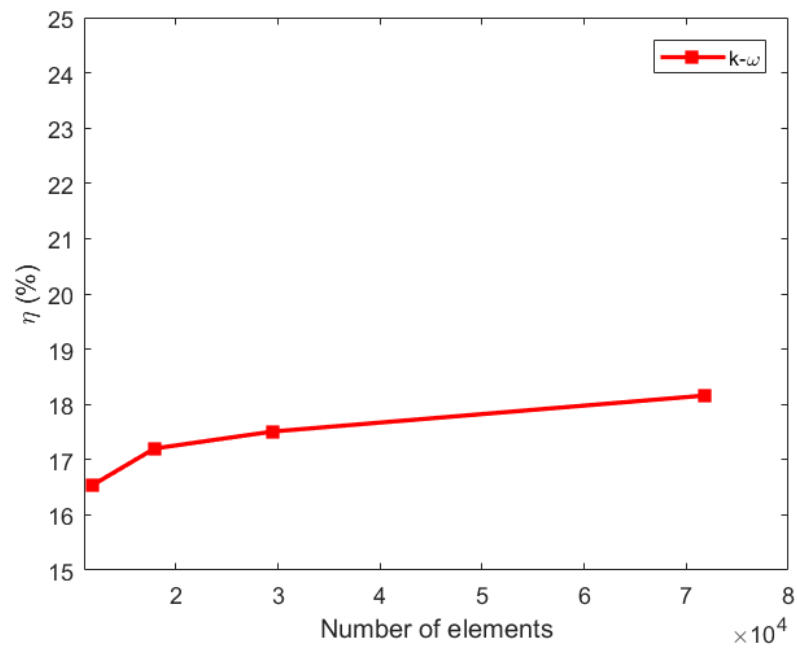
### 4.1 Mesh refinement study

In this work, three turbulence models were tested in the computational simulations:  $k-\varepsilon$ ,  $k-\omega$  and  $k-\omega$  SST. The mesh refinement analysis was carried out using an *automatic* function for mesh generation for the  $k-\omega$  and  $k-\omega$  SST models, and an *adaptive mesh refinement* function for the  $k-\varepsilon$  model. A mesh refinement study is important to ensure the minimal dependence on the approximate result (given by a computational simulation, for example) in relation to the number of elements that composes the discretized domain.

The refinement study for all the turbulence models tested is presented for an intermediate value of entrainment ratio ( $M = 3.56$ ). For the  $k-\varepsilon$  model (Figure 4.1), the adaptive mesh was composed only of triangular elements totaling 618,872 elements at the end of refinement process. For the  $k-\omega$  model (Figure 4.2), the final mesh was composed of 71,806 elements, of which 58,096 are triangular and 13,710 are quadrilateral elements. And for the  $k-\omega$  SST model (Figure 4.3), the final mesh was composed of 86,337 elements, of which 72,627 are triangular and 13,710 are quadrilateral elements.

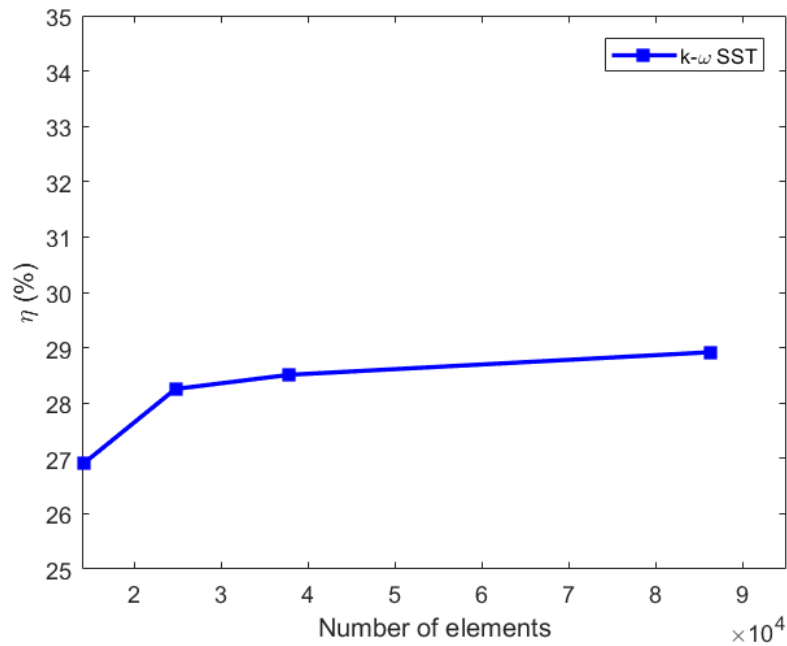
Figure 4.1 – Mesh convergence for  $k-\varepsilon$  turbulence model performed for  $M = 3.56$ .

Source: Author.

Figure 4.2 – Mesh convergence for  $k-\omega$  turbulence model performed for  $M = 3.56$ .

Source: Author.

Figure 4.3 – Mesh convergence for  $k-\omega$  SST turbulence model performed for  $M = 3.56$ .



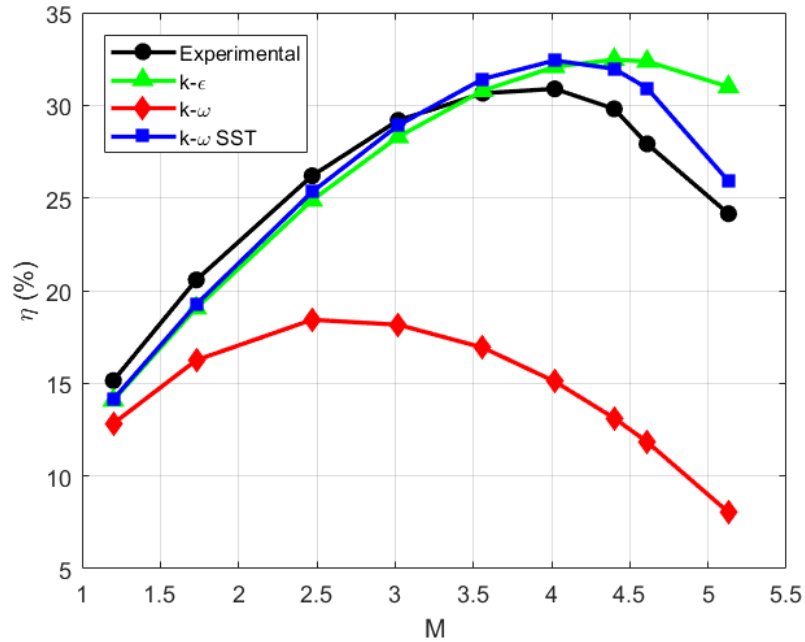
Source: Author.

## 4.2 Computational model validation

The results of the CFD simulations were used as input data into the mathematical approach from literature (WINOTO; LI; SHAH, 2000) and validated with the experimental data shared by SANGER (1968). The validation process consisted of the comparison between the efficiency curves generated by the computational simulations using each of the three turbulence models and the experimental data of SANGER (1968) (Figure 4.4). Different values of static pressure ( $P$ ) and velocity ( $V$ ) were given as results by the CFD simulations for specific  $M$  values.  $P$  and  $V$  data at the ejector cross-section regions were obtained for nine different  $M$  values (1.20, 1.73, 2.47, 3.02, 3.56, 4.02, 4.40, 4.61 and 5.13). The efficiency curves for the three turbulence models were plotted using the Equation (3.42), with the simulation data obtained for each corresponding  $M$ .

Figure 4.4 shows that the  $k-\varepsilon$  and  $k-\omega$  SST models have good fit with the experimental data up to  $M = 3.56$ . On the other hand, for  $M$  values higher than the maximum efficiency point (for  $M = 4.02$ ), the  $k-\varepsilon$  and  $k-\omega$  SST models have overestimated the ejector efficiency. The  $k-\omega$  SST model was the only model capable of predicting the operating condition which gives the efficiency peak ( $M = 4.02$ ) and also has given the

Figure 4.4 – Ejector efficiency ( $\eta$ ) as a function of the entrainment ratio ( $M$ ) for  $k-\epsilon$ ,  $k-\omega$  and  $k-\omega SST$  turbulence models in comparison with experimental data from Sanger (1968).



Source: Author.

best fit for the highest entrainment ratio ( $M = 5.13$ ), while the  $k-\omega$  model has proven to be unsatisfactory for all  $M$  in this study.

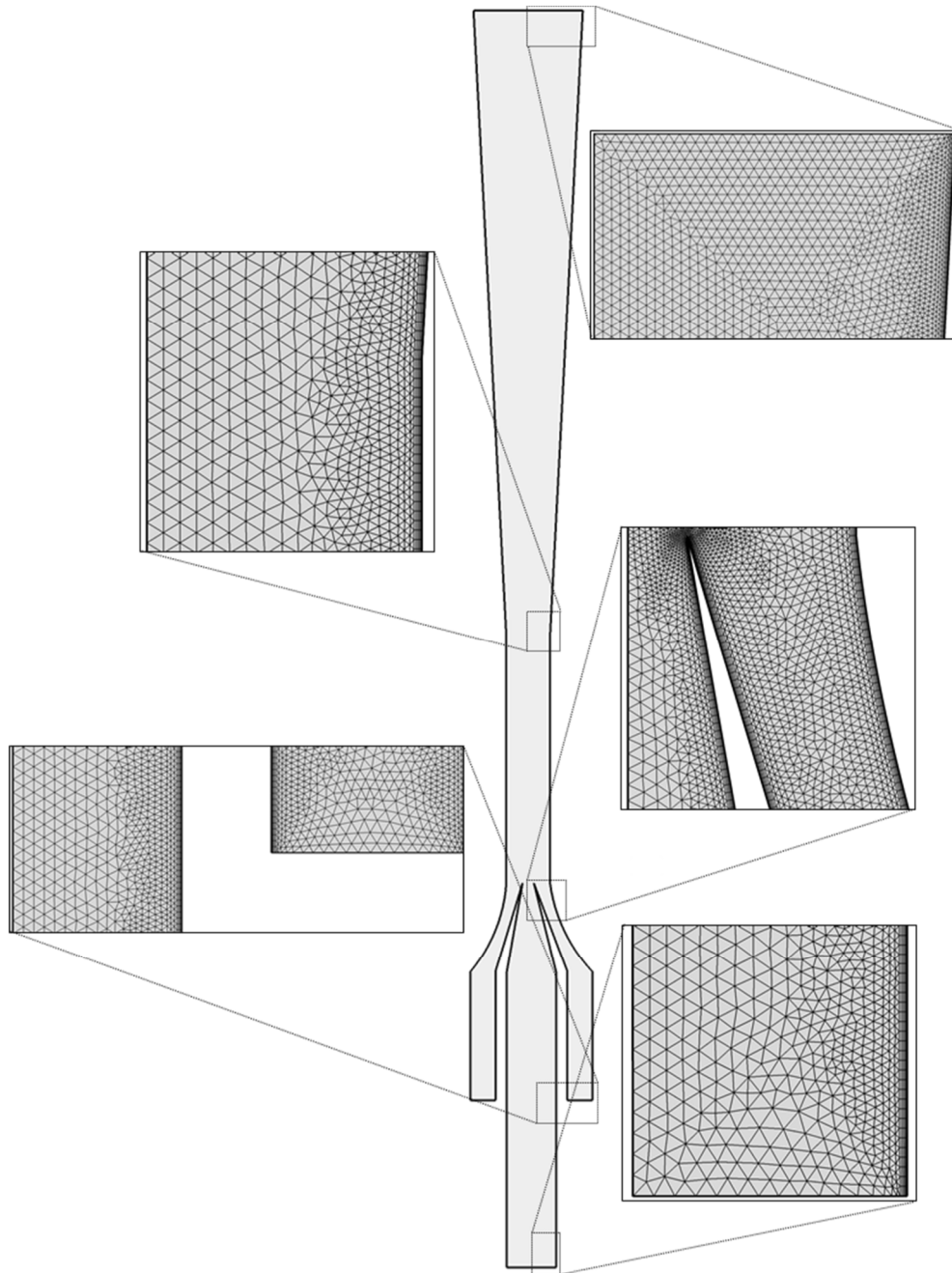
Due to the better performance demonstrated by the  $k-\omega SST$  model, it was decided to present only its final mesh for convenience, and not to show the final meshes of the other turbulence models. The final mesh for the  $k-\omega SST$  model can be analyzed in Figure 4.5, which contains five snapshots from different regions of the ejector geometry used in the CFD simulations.

It can be noticed in Figure 4.5 that the quadrilateral elements are located on the geometry wall, where the *no slip* condition was imposed (see Table 3.1). We can also observe that the final mesh is more refined in the regions near the wall and at the nozzle outlet, where the first contact between primary and secondary flows occurs.

### 4.3 Results from CFD simulations

The  $k-\omega SST$  model has shown the best fit with the experimental results (SANGER, 1968) and it was selected to be used in the further simulations to obtain the data of interest. Average values of static pressure ( $P$ ) and velocity ( $V$ ) at positions  $i$ ,  $n$ ,  $s$ ,  $v$ ,  $o$ ,

Figure 4.5 – Final mesh for the  $k-\omega$  SST turbulence model for specific regions in ejector geometry used in the CFD simulations.



Source: Author.

$t$  and  $d$  (see Figure 3.3) are shown in Tables 4.1 and 4.2, respectively, for the nine  $M$  values mentioned before.

The data presented in Tables 4.1 and 4.2 are in conformity with the theoretical explanation about the ejector's working principle described in section 2.2. Initially, the primary flow enters the nozzle (position  $i$ ) with high pressure and low velocity (2 m/s).

Table 4.1 – Average-static pressure ( $P$ ) data, in Pa, from CFD simulations for specific  $M$  values at some ejector sections of interest.

$M$	$P_i$	$P_n$	$P_s$	$P_v$	$P_o$	$P_t$	$P_d$
1.20	615714	183403	103000	99835	100770	148812	157037
1.73	613641	181328	103000	96532	97702	141198	154142
2.47	609472	177145	103000	89914	91426	128259	150100
3.02	605371	173023	103000	83469	85259	116556	146901
3.56	600480	168106	103000	75880	77969	103190	143344
4.02	595643	163243	103000	68429	70794	90112	139760
4.40	591169	158746	103000	61588	64196	78408	136064
4.61	588513	156076	103000	57542	60290	72745	133521
5.13	581377	148900	103000	46706	49821	59177	126000

Source: Author.

Table 4.2 – Average-velocity ( $V$ ) data, in m/s, from CFD simulations for specific  $M$  values at some ejector sections of interest.

$M$	$V_{1i}$	$V_{1n}$	$V_{2s}$	$V_{2v}$	$V_{3o}$	$V_{3t}$	$V_{3d}$
1.20	2.0081	29.0500	0.4864	2.5503	4.2868	4.2388	0.6782
1.73	2.0081	29.0500	0.7013	3.6410	5.2969	5.2606	0.8416
2.47	2.0081	29.0520	1.0012	5.1677	6.7142	6.6876	1.0697
3.02	2.0081	29.0530	1.2241	6.3038	7.7700	7.7479	1.2393
3.56	2.0081	29.0540	1.4430	7.4199	8.8078	8.7887	1.4058
4.02	2.0081	29.0540	1.6295	8.3708	9.6925	9.6760	1.5476
4.40	2.0081	29.0050	1.7835	9.1565	10.4240	10.4090	1.6647
4.61	2.0081	29.0560	1.8687	9.5908	10.8280	10.8130	1.7295
5.13	2.0081	29.0570	2.0794	10.6660	11.8290	11.8140	1.8898

Source: Author.

At the nozzle outlet (position  $n$ ), the primary flow is accelerated to 29 m/s. As the boundary condition of *normal inflow* was imposed at position  $i$ , the velocity profile (and consequently the average velocity) is constant for this section (i.e. does not change with the  $M$  variation). It is important to mention that variations in  $M$  were induced by increments in the volumetric flow rate of the secondary flow ( $Q_2$ ), meaning that no variations of the velocities in positions  $i$  and  $n$  were expected with the  $M$  incrementing.

Constant pressure of 103 kPa at the suction chamber inlet (position  $s$ ) for all  $M$  values is explained by the boundary condition of *normal pressure* imposed at this section. Notice that  $V_{2s}$  varies from 0.4864 to 2.0794 m/s, which is responsible for the increments in  $M$  values.

By mass conservation,  $V_{3o}$  and  $V_{3t}$  are expected to be the same since we are dealing with an incompressible flow between two sections with the same cross-sectional area. In Table 4.2, we observe a slight variation between these velocities for all  $M$  values, and it can be explained by the numerical errors due to the approximation functions used by the solver.

As already explained in section 3.2.3, the ejector efficiency is defined as the ratio of energy transferred to the secondary flow to the energy available from the primary flow (EL GAZZAR; MEAKHAIL; MIKHAIL, 2006). In practical terms, the secondary flow must have its pressure increased in the end of the compression process to avoid a null or negative efficiency. In Table 4.1,  $P_d$  is higher than  $P_s$  and lower than  $P_i$  for all  $M$  values, indicating that energy was transferred from the primary flow to the secondary flow.

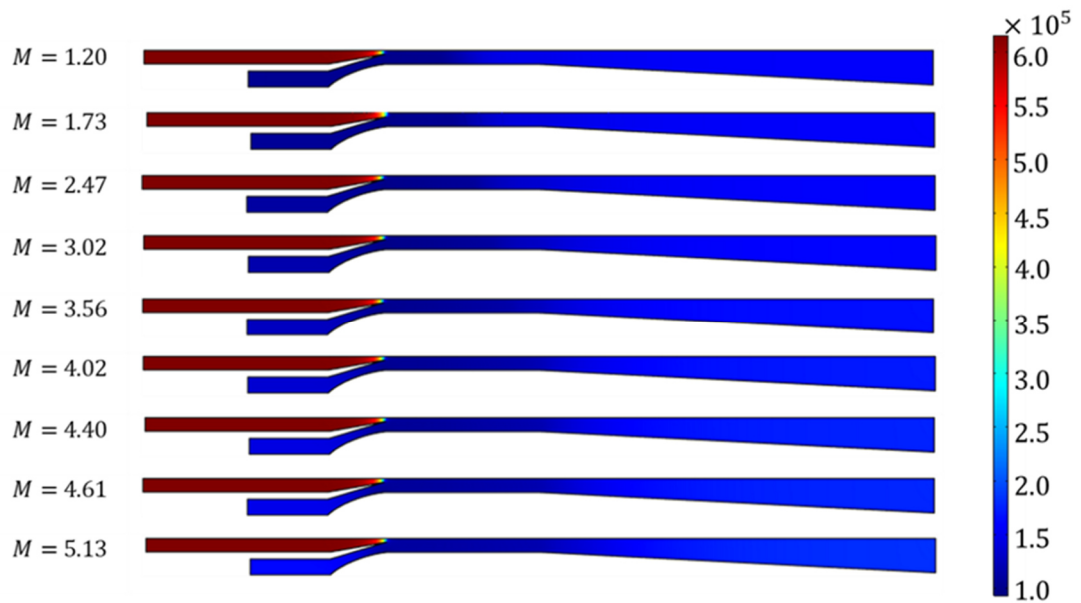
Another interesting observation is the proved importance of a diffuser in the ejector configuration. If we consider a hypothetical situation where the diffuser is absent, the ejector's final pressure (backpressure) would be given by  $P_t$ . If it would be adopted, the final pressure ( $P_t$ ) would be lower than  $P_s$  for the four last  $M$  values (4.02, 4.40, 4.61 and 5.13), and it would result in a negative efficiency. Negative efficiency means that the secondary flow is losing energy in the ejection process instead of gaining, and this is incoherent from a practical perspective.

### 4.3.1 Internal pressure distribution

In Figure 4.6, the static pressure distribution in the ejector entire domain is presented for the nine  $M$  values with a color scale. From this color scale, it is not possible to infer many conclusions, except that the nozzle is the most pressurized component of the ejector and there is a significant pressure decrease at the nozzle outlet position.

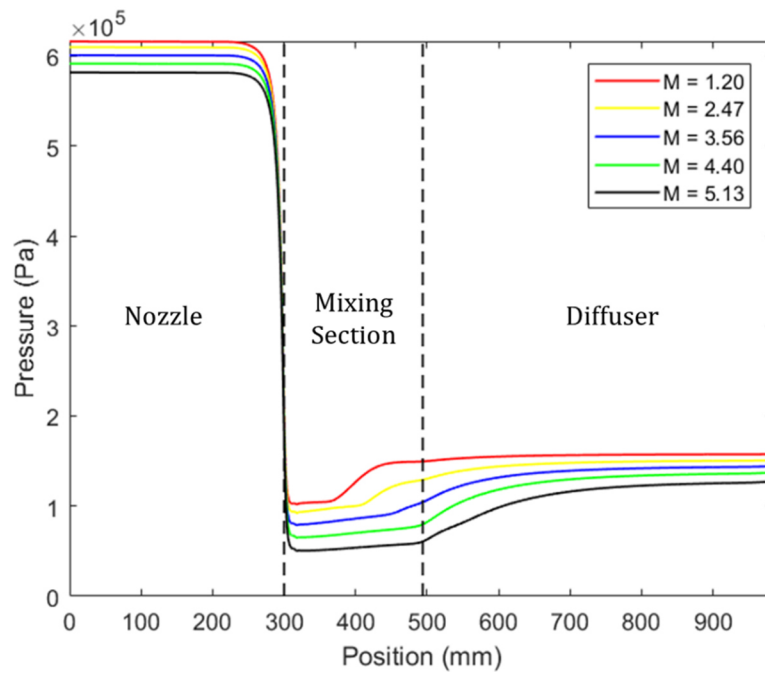
The pressure distribution along the ejector's central axis is plotted in Figure 4.7 for five  $M$  values (1.20, 2.47, 3.56, 4.40 and 5.13). This plot enables a better comprehension about the meaning of the data presented in Table 4.1. The low-pressure condition created at the nozzle outlet position is responsible for the suction of the

Figure 4.6 – Pressure distribution in ejector domain for specific  $M$  values. Color scale in Pa.



Source: Author.

Figure 4.7 – Static pressure distribution along the ejector's central axis for specific  $M$  values.



Source: Author.

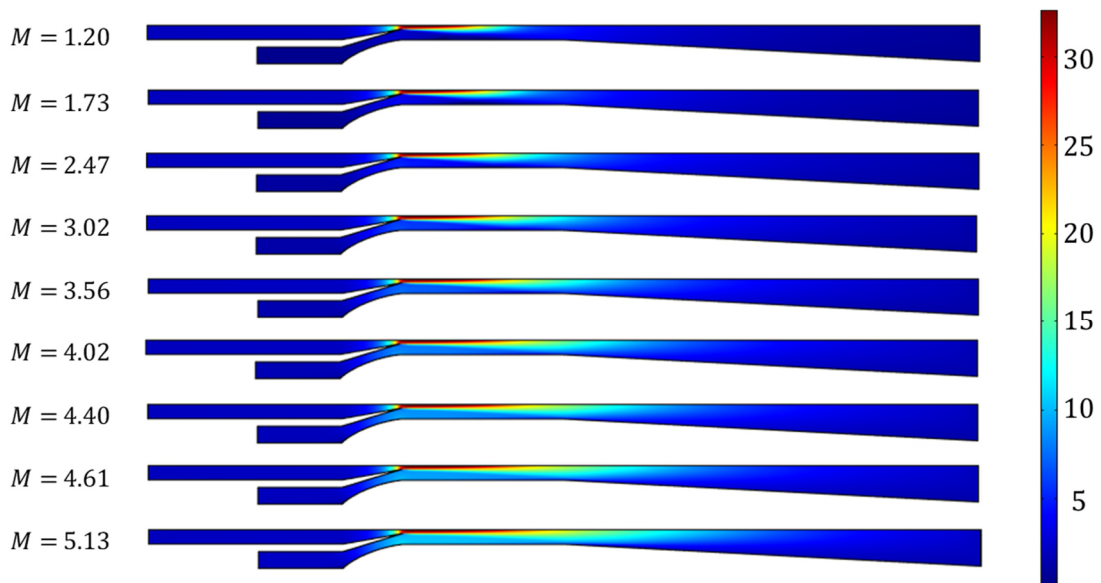


secondary flow. The process of pressure increasing starts in the mixing section with a more abrupt increment for  $M = 1.20$  and  $M = 2.47$  than for the other  $M$  values. Inside the diffuser, the opposite occurs: the more abrupt increment of the pressure is evident for the highest  $M$  values. The behavior of this plot is in conformity with those showed by ABDULATEEF et al. (2009).

### 4.3.2 Internal velocity distribution

The velocity distribution in the ejector entire domain is presented for the nine  $M$  values with a color scale in Figure 4.8. The main observation from this figure is that the mixing flow velocity significantly increases inside the mixing section with the increment of  $M$ . All the ejector positions, except the nozzle outlet, present values of velocity lower than 12 m/s, which makes it difficult to discriminate the velocity gradients by the color scale in the nozzle, suction chamber and diffuser.

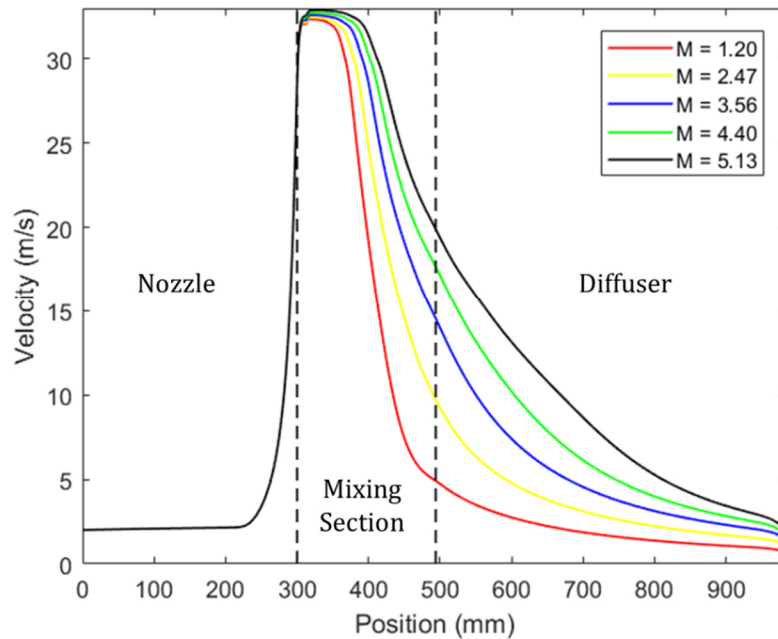
Figure 4.8 – Velocity distribution in ejector domain for specific  $M$  values. Color scale in m/s.



Source: Author.

In Figure 4.9, the velocity distribution along the ejector's central axis is presented for five  $M$  values (1.20, 2.47, 3.56, 4.40 and 5.13). Inside the nozzle, the velocity distribution is coincident for all  $M$  values, because  $V_{1i}$  does not change due to imposition of the *normal inflow* condition at the nozzle inlet. It is worth emphasizing that the velocity peak along the ejector's central axis occurs at the nozzle outlet with approximately 33 m/s. This value does not appear in Table 4.2 because this mentioned

Figure 4.9 – Velocity distribution along the ejector’s central axis for specific  $M$  values.



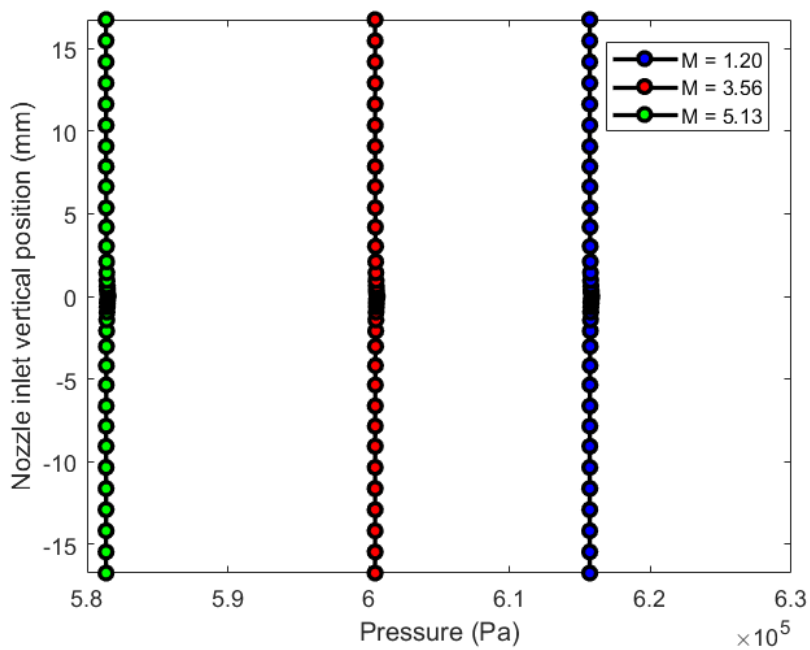
Source: Author.

table contains the average values of velocity in the sections, and not the complete values of the velocity profiles (that will also be presented in this chapter). Still in the Figure 4.9, the lower the  $M$ , the more abrupt the velocity drop inside the mixing section and diffuser.

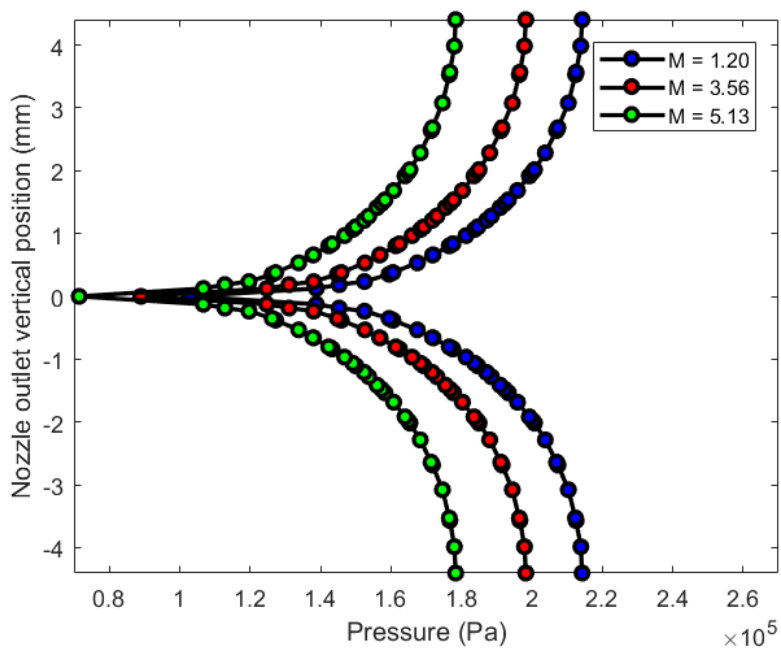
In Figures 4.7 and 4.9, the pressure and velocity distributions inside the suction chamber are not shown. Although the ejector’s symmetry axis coincides with the central axis of the suction chamber, the flow channel of the suction chamber is not connected with the ejector’s symmetry axis (see Figure 3.1).

### 4.3.3 Pressure profiles at the ejector sections

The non-uniformity of the pressure and velocity profiles explains the necessity of application of the correction factors on these data. The pressure profiles were plotted for the nozzle inlet (Figure 4.10), nozzle outlet (Figure 4.11), suction chamber inlet (Figure 4.12), suction chamber outlet (Figure 4.13), mixing section inlet (Figure 4.14), mixing section outlet (Figure 4.15) and diffuser outlet (Figure 4.16). These profiles were obtained for three  $M$  values: the lowest ( $M = 1.20$ ), the intermediate ( $M = 3.56$ ) and the highest one ( $M = 5.13$ ). The pressure and velocity profiles are presented with the vertical axis corresponding to the specific cross section of the ejector position,

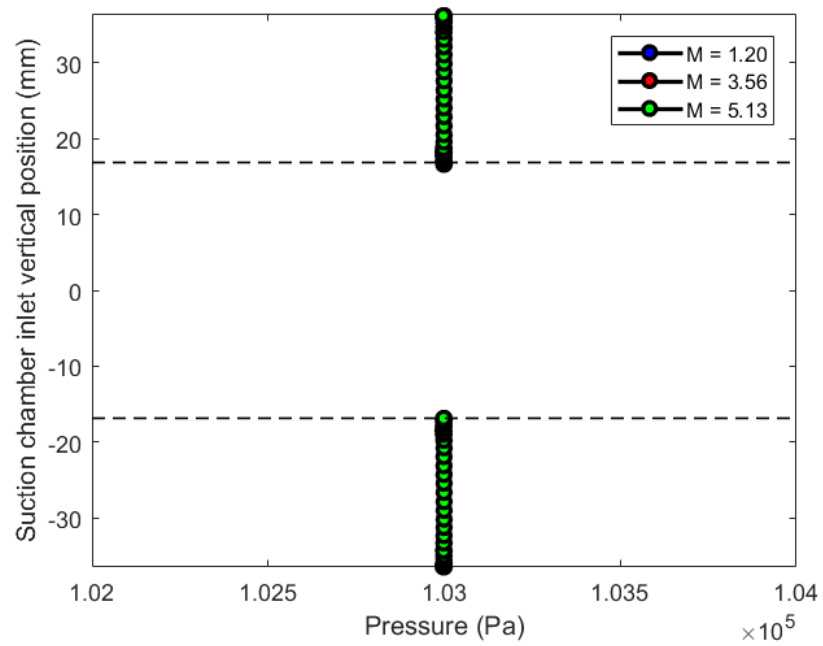
Figure 4.10 – Pressure profile at the nozzle inlet (position  $i$ ) for specific  $M$  values.

Source: Author.

Figure 4.11 – Pressure profile at the nozzle outlet (position  $n$ ) for specific  $M$  values.

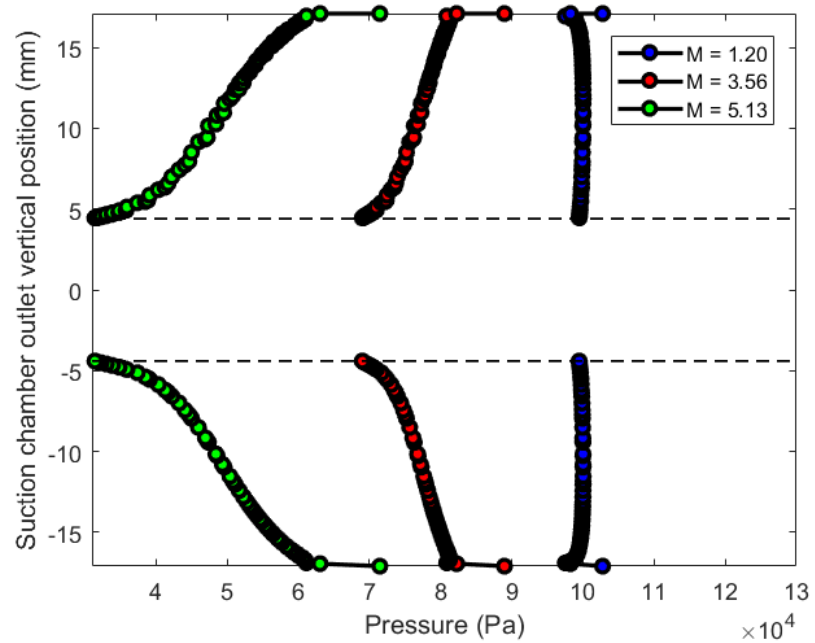
Source: Author.

Figure 4.12 – Pressure profile at the suction chamber inlet (position  $s$ ) for specific  $M$  values.

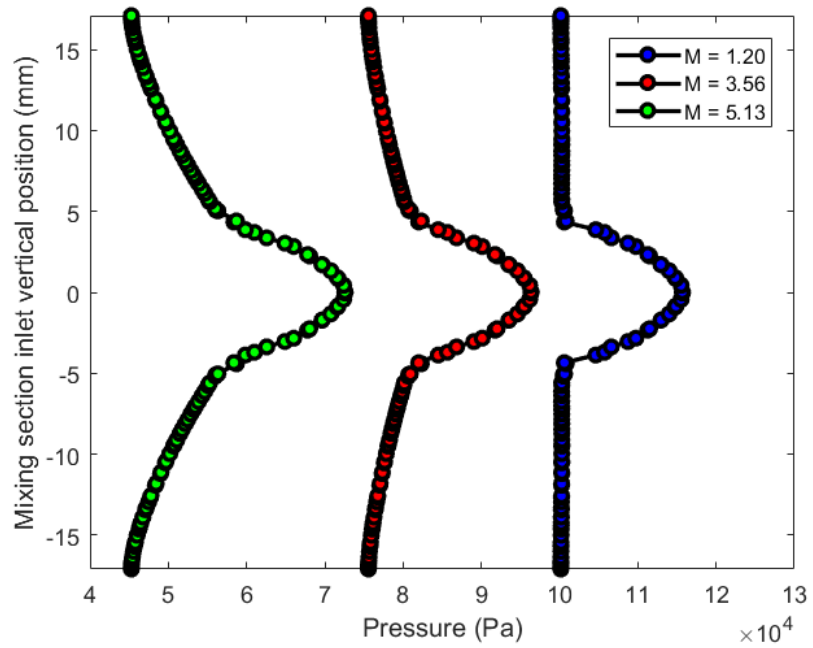


Source: Author.

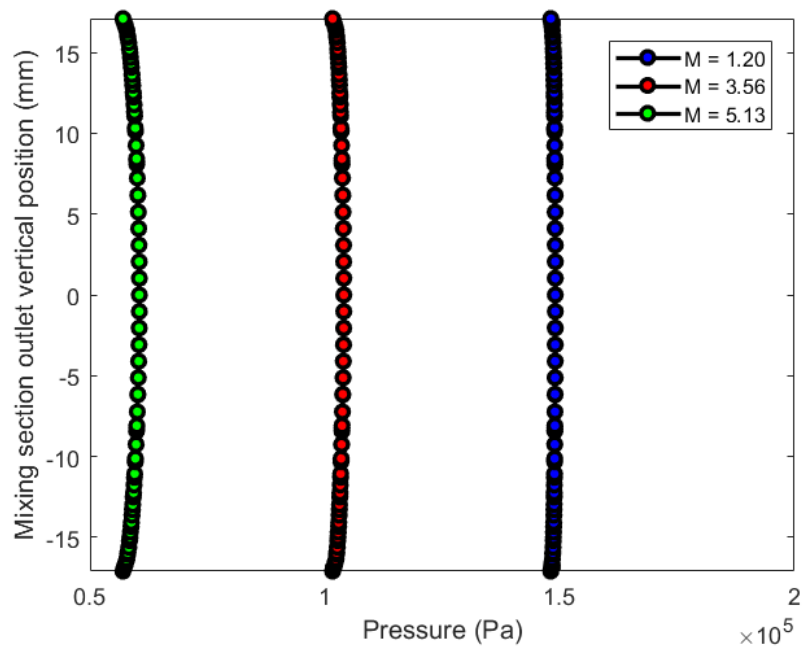
Figure 4.13 – Pressure profile at the suction chamber outlet (position  $v$ ) for specific  $M$  values.



Source: Author.

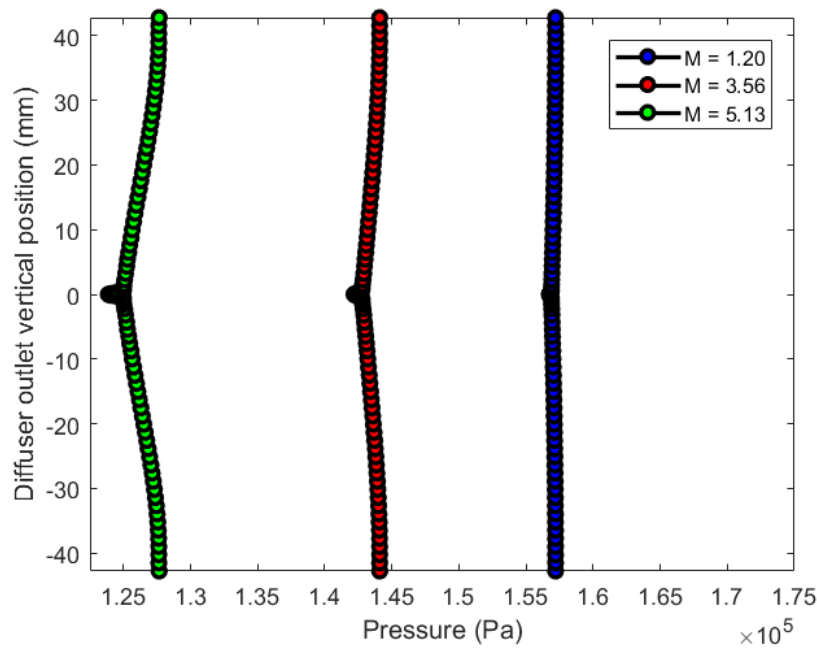
Figure 4.14 – Pressure profile at the mixing section inlet (position  $o$ ) for specific  $M$  values.

Source: Author.

Figure 4.15 – Pressure profile at the mixing section outlet (position  $t$ ) for specific  $M$  values.

Source: Author.

Figure 4.16 – Pressure profile at the diffuser outlet (position  $d$ ) for specific  $M$  values.



Source: Author.

whose central point representing the position of the symmetry axis (0 mm) and the limits ranging from  $-radius$  to  $+radius$  of the circular section.

From Figure 4.10, we infer that the pressure profile at the nozzle inlet is uniform for all the three  $M$  values, and the pressure values correspond to their average values shown in Table 4.1. The static pressure of the primary flow at the nozzle inlet decreases with the increment of  $M$ .

In Figure 4.11, the point of minimum pressure is located in the center of the cross section at the nozzle outlet. It is expected because this is the point where the maximum velocity is achieved. From this figure, we can better visualize the low-pressure region created at the nozzle outlet section, which is responsible for the suction of the secondary flow. At this region, all profiles have the same behavior, with higher-pressure values near wall and lower-pressure values as it approaches the center of the circular section.

At the suction chamber inlet, the boundary condition of *normal pressure* (with fixed 103 kPa) was imposed and it explains the linearity (or uniformity) of the pressure profile at this section, as shown in Figure 4.12. A gap delimited by two dashed lines was intentionally left between the two flow passages of the suction chamber in order to

represent the presence of the nozzle plus its thickness, respecting the ejector's original geometry (see Figure 3.3).

A similar gap was encountered in Figure 4.13 to represent the nozzle outlet diameter that exists between the suction chamber outlet and mixing section inlet. In that figure, we can notice that the pressure profile at the suction chamber outlet is uniform for  $M = 1.20$  and non-uniform for  $M = 3.56$  and  $M = 5.13$ . Thus, the uniformity of the pressure profile at the suction chamber outlet is dependent on  $M$ .

Figure 4.14 shows the three profiles with two distinct pressure gradients in each one. In the central portion of the three profiles, the right-side deflection represents the pressure gradient of the nozzle outlet, while the gradients of the upper and lower portions refer to the suction chamber outlet. Notice that the pressure profile for  $M = 1.20$  remains uniform in the upper and lower portions of the profile, which can be corroborated by Figure 4.13.

At the mixing section outlet, all the three profiles are approximately uniform (Figure 4.15), and it is a strong indicative that the complete mixing between both primary and secondary flows is achieved. Uniformity of the three profiles is preserved at the diffuser outlet, as shown in Figure 4.16. It is important to emphasize that the ejector efficiency is not measured by the maximum backpressure ( $P_d$ ), but by the definition of Equation (3.42). As we can see from Figure 4.16 and Table 4.1, the maximum  $P_d$  is given for  $M = 1.20$  and curiously this corresponds to the operating condition that culminated in the lowest equipment efficiency (see Figure 4.4).

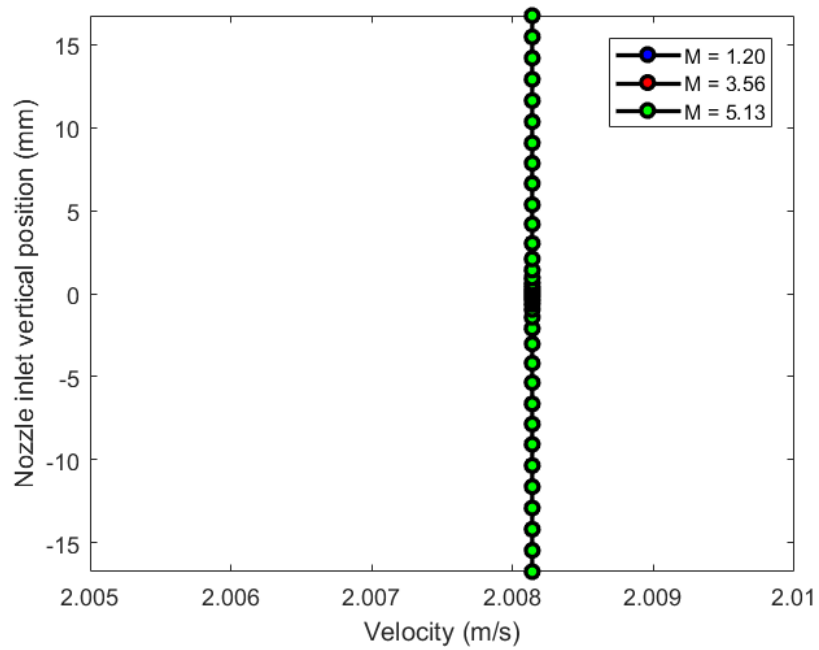
#### 4.3.4 Velocity profiles at the ejector sections

Following the same justification as the previous section, the velocity profiles were plotted for the nozzle inlet (Figure 4.17), nozzle outlet (Figure 4.18), suction chamber inlet (Figure 4.19), suction chamber outlet (Figure 4.20), mixing section inlet (Figure 4.21), mixing section outlet (Figure 4.22) and diffuser outlet (Figure 4.23), for the lowest ( $M = 1.20$ ), the intermediate ( $M = 3.56$ ) and the highest  $M$  ( $M = 5.13$ ).

In Figure 4.17, the three velocity profiles are overlapping since the boundary condition of normal inflow ( $Q_1 = 1.77 \times 10^{-3} \text{ m}^3/\text{s}$  and  $V_{1i} = 2.00 \text{ m/s}$ ) was imposed at the nozzle inlet (see Table 3.1).

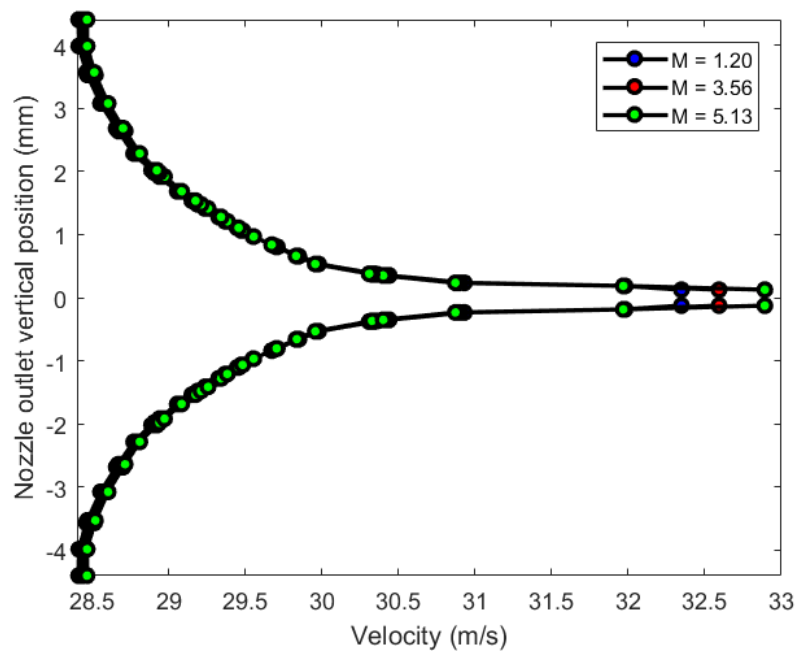
At the nozzle outlet position (Figure 4.18) the three velocity profiles are also overlapping, with the exception of the points in the central portion of the nozzle (near

Figure 4.17 – Velocity profile at the nozzle inlet (position  $i$ ) for specific  $M$  values.



Source: Author.

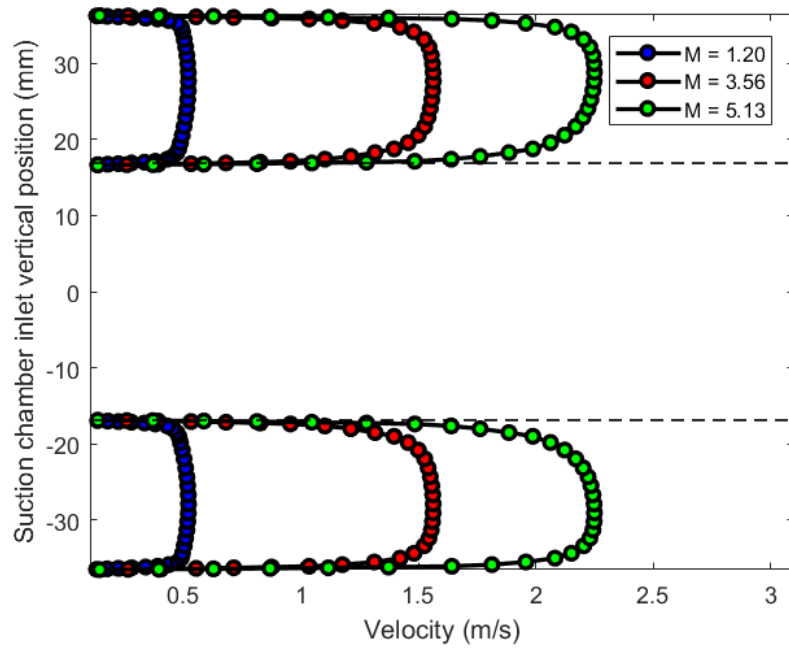
Figure 4.18 – Velocity profile at the nozzle outlet (position  $n$ ) for specific  $M$  values.



Source: Author.

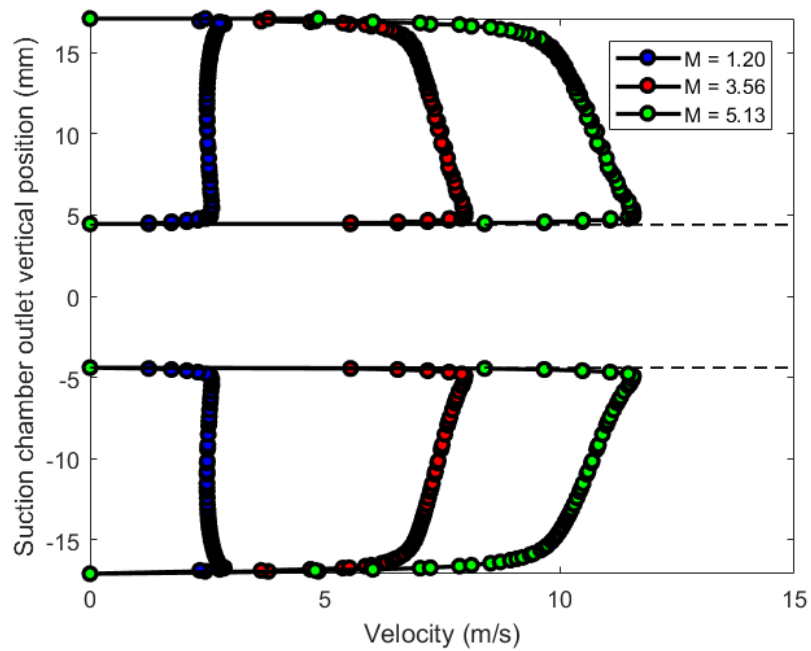


Figure 4.19 – Velocity profile at the suction chamber inlet (position  $s$ ) for specific  $M$  values.



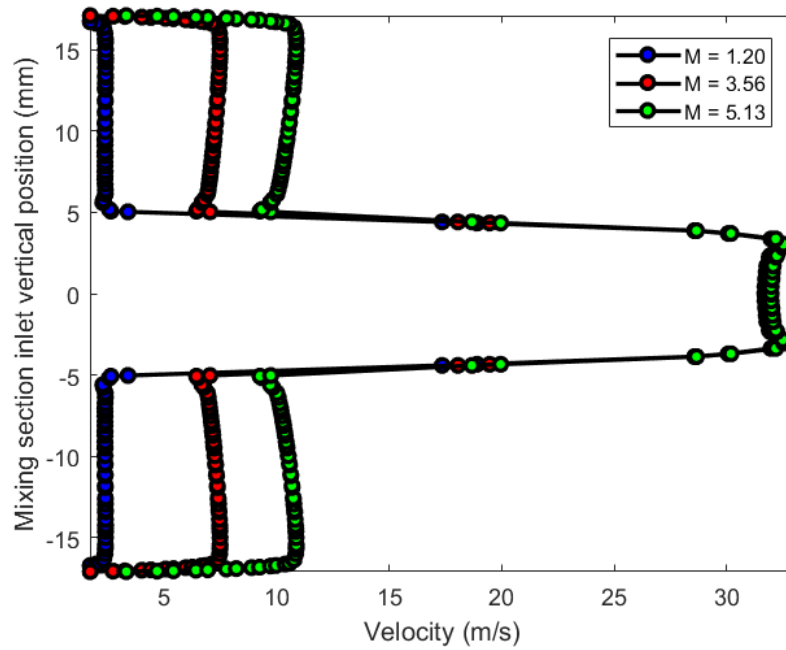
Source: Author.

Figure 4.20 – Velocity profile at the suction chamber outlet (position  $v$ ) for specific  $M$  values.



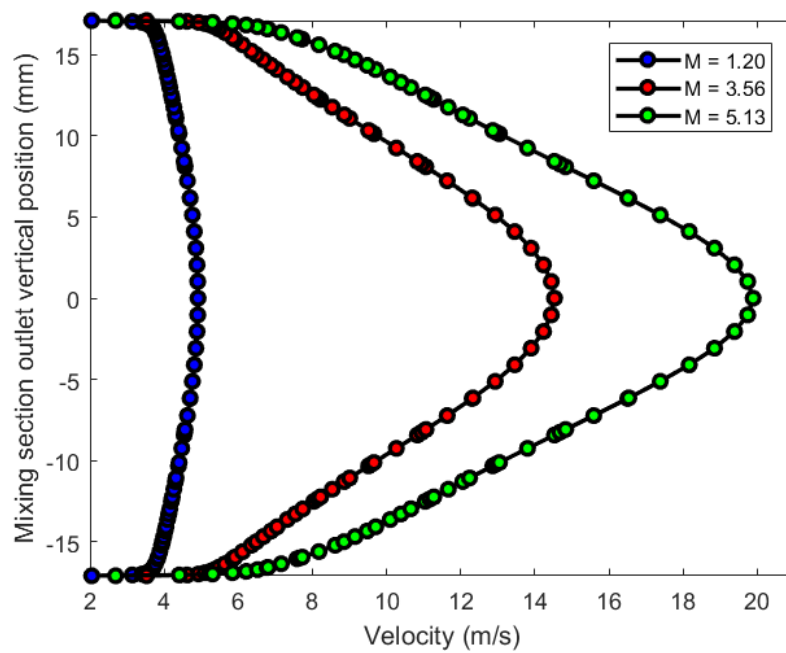
Source: Author.

Figure 4.21 – Velocity profile at the mixing section inlet (position  $o$ ) for specific  $M$  values.



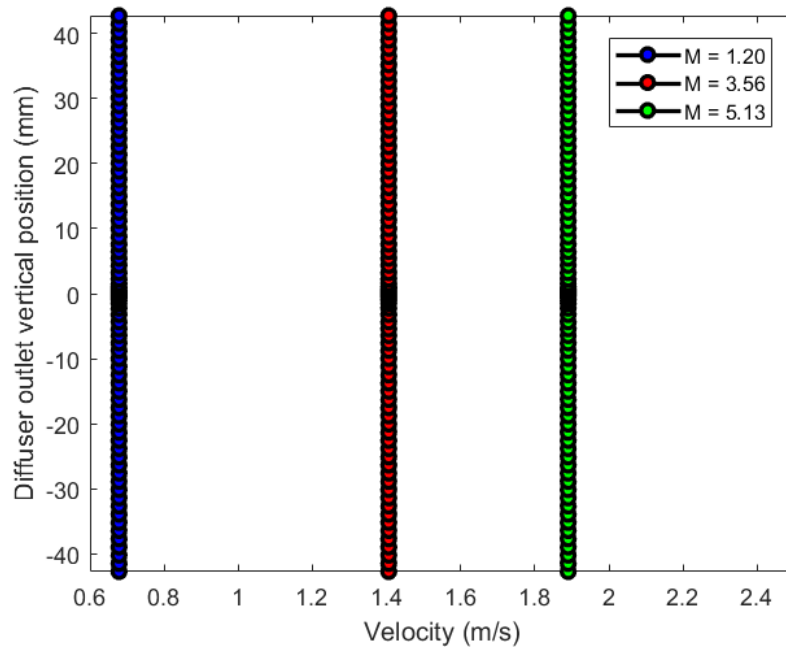
Source: Author.

Figure 4.22 – Velocity profile at the mixing section outlet (position  $t$ ) for specific  $M$  values.



Source: Author.

Figure 4.23 – Velocity profile at the diffuser outlet (position  $d$ ) for specific  $M$  values.



Source: Author.

radius = 0 mm), where the velocity intensity varies as a function of  $M$ . This phenomenon can be also observed in Figure 4.9, where the velocity intensity is slightly different at the nozzle outlet section for different  $M$  values. Still in the Figure 4.18, the points of maximum velocity are in agreement with the points of minimum pressure in Figure 4.11. It is consistent if we understand that the total energy is conserved at the nozzle outlet, i.e., an increment in kinetic energy (increase of the flow velocity) implies a reduction in the flow work (pressure reduction), so that the principle of energy conservation is satisfied. This can be better visualized with Equation (3.22).

The velocity profiles at the suction chamber inlet are shown in Figure 4.19. The dashed-line gap in this figure follows the same justification as in Figure 4.12. The uniform behavior is observed only for  $M = 1.20$ , while the non-uniformity is observed for  $M = 3.56$  and  $M = 5.13$ . As it occurs at the suction chamber inlet, the uniform feature is also observed only for  $M = 1.20$  at the suction chamber outlet (Figure 4.20).

Similar to Figure 4.14, Figure 4.21 exhibits the three profiles with two different pressure gradients. In their central part, the right-side deflection represents the velocity intensity of the nozzle outlet, while the velocity gradients of the upper and lower portions refer to the suction chamber outlet. The velocity intensities for the

nozzle outlet and suction chamber outlet presented in Figure 4.21 can be corroborated with the velocity values expressed in Figures 4.18 and 4.20.

In Figure 4.22, the velocity profiles are presented for the mixing section outlet. It is observed that the profile amplitude increases with the increment of  $M$ . By comparing the pressure and velocity profiles at the mixing section outlet (Figures 4.15 and 4.22, respectively), we notice that the pressure stabilization of the mixing flow occurs earlier than its velocity stabilization. The velocity stabilization occurs only inside the diffuser (Figure 4.23), where the boundary condition of *normal outflow* velocity is imposed at its outlet section (see Table 3.1). As the velocity profiles at the nozzle inlet and diffuser outlet are uniform, the average velocities shown in Table 4.2 represent the entire profiles for each  $M$  value.

#### 4.4 Calculation of the friction loss coefficients

Using results from CFD simulations (i.e. average pressure and velocity at the cross-sectional areas at positions  $i, n, s, v, o, t$  and  $d$ ), constant  $\rho = 998.2 \text{ kg/m}^3$ ,  $R = 0.066$  and  $a = 0.160$ , the friction loss coefficients of the nozzle ( $K_N$ ), suction chamber ( $K_S$ ), mixing section ( $K_M$ ) and diffuser ( $K_D$ ) were calculated using Equations (3.30), (3.32), (3.34) and (3.38), respectively, for the nine  $M$  values (Table 4.3).

Table 4.3 – Friction loss coefficients of each ejector component calculated with the 1D mathematical model for specific  $M$  values.

$M$	$K_N$	$K_S$	$K_M$	$K_D$
1.20	0.0312	0.0114	-0.4808	0.0811
1.73	0.0312	0.0147	-0.2328	0.0528
2.47	0.0311	0.0193	-0.0500	-0.0057
3.02	0.0311	0.0225	0.0407	-0.0544
3.56	0.0310	0.0248	0.1119	-0.0952
4.02	0.0311	0.0264	0.1668	-0.1248
4.40	0.0311	0.0276	0.2032	-0.1300
4.61	0.0311	0.0281	0.2010	-0.0950
5.13	0.0311	0.0295	0.1783	0.0214
<b>Average</b>	<b>0.0311</b>	<b>0.0227</b>	<b>0.1498</b>	<b>0.0518</b>

Source: Author.

As shown in Table 4.3, some of the friction loss coefficients are negative for specific  $M$  values, which is physically inconsistent. A hypothetical situation where the friction losses are negative means that there is energy gain instead of energy loss. This phenomenon would violate the *Second Law of Thermodynamics*, whose entropy statement enunciates that “*it is impossible for any system to operate in a way that entropy is destroyed*” (MORAN; SHAPIRO; BOETTNER, 2011). In statistical thermodynamics, entropy is associated with the notion of microscopic disorder, so that entropy increases as the process tend to their state of equilibrium (MORAN; SHAPIRO; BOETTNER, 2011). Considering this certification, in real cases (i.e. irreversible processes), entropy generation (which may be associated to friction losses in fluid flows) cannot be negative.

To overcome the limitation of negative friction loss coefficients, they were not taken into account in the calculation of the average values of the friction loss coefficients. Thus, the average friction loss coefficients (last row in Table 4.3) for the mixing section and diffuser were calculated with only their positive values.

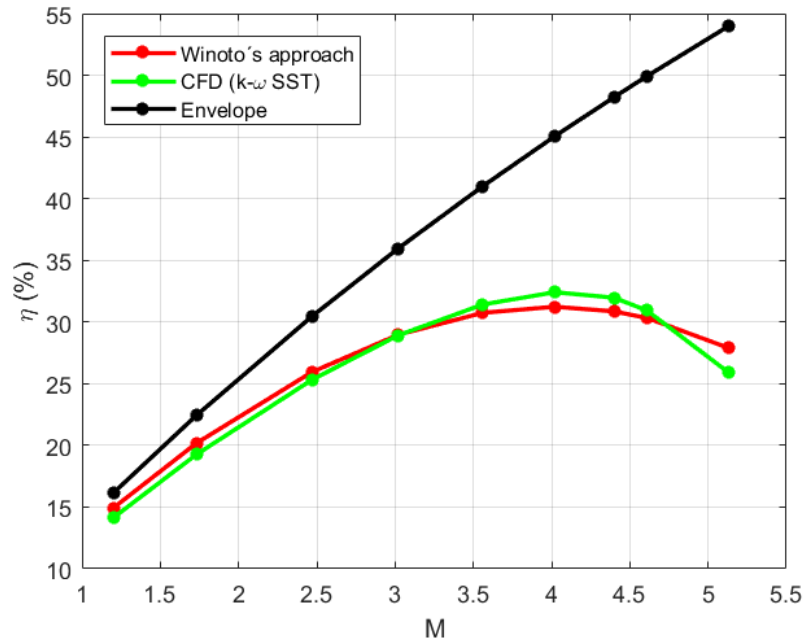
## 4.5 Efficiency analysis with the mathematical model

From Equation (3.40) it is possible to calculate a corresponding pressure recovery ratio ( $N$ ) for each  $M$ , and also the ejector efficiency curve using Equation (3.42). The same procedure is employed to obtain the ideal efficiency curve (envelope of operation), but considering Equations (3.41) and (3.43).

The accuracy of the mathematical model was tested by comparing the three efficiency curves in Figure 4.24: i) in red: the efficiency curve plotted with the mathematical model including the calculated friction loss coefficients shown in Table 4.3; ii) in green: the efficiency curve generated from data of the CFD simulations; and iii) in black: the ejector theoretical maximum efficiency (ideal efficiency). The efficiency curve from simulation data was obtained considering the turbulence model which showed the best agreement with the experimental results ( $k-\omega$  SST).

In Figure 4.24, we observe that the efficiency curve plotted with the calculated friction loss coefficients (“*Mathematical model*”) shows a great agreement with simulation data, mainly for  $M$  values between 1.20 and 3.56, and the peak of both efficiency curves is coincident for  $M = 4.02$ . In addition, the ejector envelope of operation (ideal efficiency), estimated by the mathematical model, have accurately

Figure 4.24 – Ejector efficiency curves plotted with the calculated friction loss coefficients by the mathematical model and simulation data, compared with the ideal efficiency as a function of  $M$ .



Source: Author.

restricted the ejector's operating points, considering that the simulation results are below the theoretical maximum efficiency that the ejector can reach (envelope).

## 4.6 Calculation of the corrected friction loss coefficients

In order to properly express the terms of pressure and kinetic energy in the conservation equations for the nozzle, suction chamber and diffuser, Equations (3.46) and (3.47) were employed in the CFD results for some ejector's positions of interest.

Pressure ( $\gamma$ ) and kinetic-energy ( $\alpha$ ) correction factors were not applied for the mixing section, since the mixing phenomenon inside this component is modeled by the principle of momentum flux conservation (see Equation (3.3)). Thus, the application of  $\gamma$  and  $\alpha$  between positions  $o$  and  $t$  has no plausible justification. However,  $\alpha$  was employed in the diffuser inlet section, which is coincident with the mixing section outlet (position  $t$ ), since both components are connected. In addition, the correction factors were not applied for the suction chamber outlet section (position  $v$ ), and even

without that, results were satisfactory, as will be discussed later. In summary, the correction factors were applied for the nozzle inlet (position  $i$ ), nozzle outlet (position  $n$ ), suction chamber inlet (position  $s$ ), diffuser inlet (position  $t$ ) and diffuser outlet (position  $d$ ), and their calculated values are exposed in Table 4.4.

Table 4.4 – Pressure ( $\gamma$ ) and kinetic-energy ( $\alpha$ ) correction factors for the pressure and velocity profiles for specific  $M$  values at some ejector sections of interest.

$M$	$\gamma_i$	$\gamma_n$	$\gamma_s$	$\gamma_t$	$\gamma_d$	$\alpha_i$	$\alpha_n$	$\alpha_s$	$\alpha_t$	$\alpha_d$
1.20	1.0000	1.0016	1.0000	1.0001	1.0000	1.0000	1.0074	1.0394	1.0232	1.0000
1.73	1.0000	1.0017	1.0000	1.0003	1.0000	1.0000	1.0075	1.0478	1.0530	1.0000
2.47	1.0000	1.0017	1.0000	1.0006	1.0000	1.0000	1.0074	1.0567	1.1289	1.0000
3.02	1.0000	1.0017	1.0000	1.0009	1.0000	1.0000	1.0074	1.0601	1.2022	1.0000
3.56	1.0000	1.0018	1.0000	1.0015	1.0000	1.0000	1.0074	1.0615	1.2723	1.0000
4.02	1.0000	1.0019	1.0000	1.0021	1.0000	1.0000	1.0075	1.0608	1.3256	1.0000
4.40	1.0000	1.0037	1.0000	1.0030	1.0000	1.0000	1.0126	1.0600	1.3522	1.0000
4.61	1.0000	1.0020	1.0000	1.0030	1.0000	1.0000	1.0074	1.0591	1.3401	1.0000
5.13	1.0000	1.0021	1.0000	1.0043	1.0000	1.0000	1.0074	1.0551	1.2878	1.0000

Source: Author.

In Table 4.4,  $\alpha_i$  and  $\alpha_d$  are equivalent to 1.0000 due to the boundary condition of *normal inflow* imposed at the nozzle inlet and diffuser outlet sections. Explaining better, in the numerator of Equation (3.47), the integrals of the linear velocity profiles in the areas of these two sections correspond to the same value of the constant denominators (see Figures 4.17 and 4.23). As the boundary condition of *normal pressure* was imposed at the suction chamber inlet,  $\gamma_s$  is also 1.0000 (see Figure 4.12). Finally, the pressure profile in the nozzle inlet is uniform (see Figure 4.10) and the pressure profile in the diffuser outlet is approximately uniform (see Figure 4.17), and this explains why  $\gamma_i$  and  $\gamma_d$  are also equal to 1.0000.

In other words, one of the hypothesis of the Equation (3.25) assumes that the pressure and velocity profiles in the cross sections are uniform, so that the correction factors should not influence the corresponding terms of pressure and kinetic energy.

The  $\alpha_s$  values in Table 4.4 are consistent with the theoretical values found in MUNSON; YOUNG; OKIISHI (2013) for the specific behavior of the velocity profile in position  $s$ . For velocity profiles similar to a “flattened parabola” (as in Figure 4.19), MUNSON; YOUNG; OKIISHI (2013) suggest  $\alpha = 1.08$ , that slightly diverges in the

second decimal digit from the values in the eighth column of Table 4.4. Finally, the variations of  $\gamma_n$  are higher than the variations of  $\alpha_n$  as a function of  $M$ , since the pressure profiles at the nozzle outlet section (see Figure 4.11) are quantitatively different from each other and the velocity profiles in the same section are almost overlapping (see Figure 4.18). The opposite occurs in the mixing section outlet, where we observe that the variations of  $\alpha_t$  are higher than the variations of  $\gamma_t$ , since the behavior of the velocity profile is more sensitive to  $M$  rather than the pressure profile at the same section (see Figures 4.15 and 4.22).

Employing the correction factors exposed in Table 4.4, the corrected friction loss coefficients of the nozzle ( $K_N'$ ), suction chamber ( $K_S'$ ) and diffuser ( $K_D'$ ) were calculated with Equations (3.48), (3.49) and (3.50), respectively, and they are shown in Table 4.5.

Table 4.5 – Corrected friction loss coefficients for the nozzle, suction chamber and diffuser, calculated with the 1D mathematical model coupled with the correction factors for specific  $M$  values.

$M$	$K_N'$	$K_S'$	$K_D'$
1.20	0.0303	0.0070	0.1171
1.73	0.0302	0.0140	0.1319
2.47	0.0302	0.0201	0.1811
3.02	0.0301	0.0240	0.2370
3.56	0.0301	0.0266	0.2963
4.02	0.0302	0.0282	0.3425
4.40	0.0329	0.0295	0.3750
4.61	0.0302	0.0299	0.3923
5.13	0.0301	0.0313	0.4346
<b>Average</b>	<b>0.0305</b>	<b>0.0234</b>	<b>0.2786</b>

Source: Author.

Compared to their non-corrected version, calculated with the initial mathematical formulation (WINOTO; LI; SHAH, 2000), the corrected friction loss coefficients presented a deviation of 1.929% for  $K_N'$ , 2.991% for  $K_S'$  and 81.407% for  $K_D'$ . Considering this, we can infer that the diffuser is the component most affected by the application of the correction factors.



As already mentioned in section 3.1.4, Reynolds number ( $Re$ ) is a dimensionless parameter written in terms of the flow velocity, pipe diameter and kinematic viscosity. Reynolds number is useful to classify a fluid flow in laminar ( $Re < 2000$ ) or turbulent ( $Re > 2000$ ). In the simulations of the present work, Reynolds number was incremented with the  $M$  increasing. From that, we can observe in Table 4.5 that  $K_N'$  and  $K_S'$  are not dependent on the *Reynolds number* since these values do not significantly change with the  $M$  variation.

## 4.7 A new approximation

In this section, a new approximation is proposed to model the efficiency of an incompressible-flow ejector, which may be useful in analysis where data of CFD simulations are available.

As shown in section 3.2.3, some assumptions were considered in the original mathematical formulation. In the new approximation, the assumption of average values of pressure and velocity in the cross-sections was removed, and the correction factors were applied into the energy equations for the nozzle, suction chamber and diffuser. In addition to the assumptions listed in section 3.2.3, the two following additional assumptions were adopted in the formulation of the new approximation:

- Constant friction loss coefficient for the mixing section (average value of  $K_M$  in Table 4.3);
- No correction factors for the suction chamber outlet section (position  $v$ ).

The mathematical model proposed by WINOTO; LI; SHAH (2000) considers that the pressures of the primary and secondary flows at the mixing section inlet have the same value ( $P_o$ ). This assumption enables to express the ejector efficiency as a function independent of the pressure and velocity data, which is very useful when only some geometrical parameters are known. In addition, this model adjusts well to the authors' own experimental data considering the specific friction loss coefficients obtained by them.

On the other hand, it was observed in Table 4.1 that the values of  $P_n$  and  $P_v$  are not equivalent and the assumption of a single average value to represent these two pressures at the mixing section inlet might not be acceptable in some cases. In order to

overcome this limitation, the new efficiency approximation considers different pressure values at the mixing section inlet. As consequence, some pressure and velocity data are necessary to be input in the new approach. Nevertheless, this is not a limitation as long as CFD data are available.

To define the new mathematical approach, we will take the opposite direction of the sequence used to introduce the original model in section 3.2.3. First, the new ejector's efficiency approach ( $\eta^{new}$ ) is introduced:

$$\eta^{new} = M \times N' \quad (4.1)$$

where  $N'$  is the new version of the pressure recovery ratio, which includes the correction factors on its definition.

Following the same principle of Equation (3.39), the corrected pressure recovery ratio is defined as

$$N' = \frac{\bar{P}_d' - \bar{P}_s'}{\bar{P}_i' - \bar{P}_d'} \quad (4.2)$$

where  $\bar{P}_i'$ ,  $\bar{P}_s'$  and  $\bar{P}_d'$  are the corrected total pressures defined in Equations (3.48) to (3.53).

Before deducing the complete expression of  $N'$ , three new *correlations parameters* are introduced:

$$\delta = \delta(M) = \frac{P_o - P_t}{\rho[V_{3t}^2(1 + 0.5K_M) - V_{1n}^2R - V_{2v}^2(1 - R)]} \quad (4.3)$$

$$\sigma = \sigma(M) = \frac{P_v}{P_o} \quad (4.4)$$

$$\lambda = \lambda(M) = \frac{P_n}{P_o} \quad (4.5)$$

All three correlation parameters depend on  $M$ , so that for each  $M$  there are different  $\delta$ ,  $\sigma$  and  $\lambda$ . In order to guarantee a better comprehension, the function of the three correlation parameters will be explained as they appear throughout the model development in this section.

In Equation (3.34), the approximation  $V_{1n}R + V_{2v}(1 - R) = V_{3t}$  proposed by WINOTO; LI; SHAH (2000) (deduced from mass conservation between the positions

$o$  and  $t$ ) is employed in order to write the mixing section equation in terms of squared velocities ( $V_{1n}^2$ ,  $V_{2v}^2$  and  $V_{3t}^2$ ). As the efficiency function of pumps is a parabola with downward concavity, the squared velocities enable the expression of the efficiency as a second-degree function. However, this approximation, i.e.  $V_{1n}R + V_{2v}(1 - R) = V_{3t}$ , presents a small divergence that significantly affect the efficiency approach if it is propagated throughout the following steps of the new formulation.

To overcome this deviation,  $\delta$  was implemented into Equation (3.34) to validate the mathematical relationship that represents the difference  $P_o - P_t$ . Therefore, the new equation for the mixing section becomes

$$P_o - P_t = \delta\rho[V_{3t}^2(1 + 0.5K_M) - V_{1n}^2R - V_{2v}^2(1 - R)] \quad (4.6)$$

Still with the purpose of facilitating the comprehension, the numerator of Equation (4.2) will be expanded first and the denominator later. Using the definitions presented in Equations (3.49) and (3.50), the numerator of Equation (4.5) becomes

$$\bar{P}_d' - \bar{P}_s' = \left\{ \gamma_t P_t + \frac{\rho}{2} [V_{3t}^2 \alpha_t - K_D' \alpha_d V_{3t}^2 (a - 1)^2] \right\} - \left\{ P_v + \rho \frac{V_{2v}^2}{2} (1 + K_S') \right\} \quad (4.7)$$

Coupling the terms with common factors,  $\rho/2$  and  $V_{3t}^2$ , and rearranging, we obtain

$$\bar{P}_d' - \bar{P}_s' = \gamma_t P_t - P_v + \frac{\rho}{2} \{ V_{3t}^2 [\alpha_t - K_D' \alpha_d (a - 1)^2] - V_{2v}^2 (1 + K_S') \} \quad (4.8)$$

Substituting  $P_v = \sigma P_o$  in Equation (4.8), it turns

$$\bar{P}_d' - \bar{P}_s' = \gamma_t P_t - \sigma P_o + \frac{\rho}{2} \{ V_{3t}^2 [\alpha_t - K_D' \alpha_d (a - 1)^2] - V_{2v}^2 (1 + K_S') \} \quad (4.9)$$

The purpose of replacing the relation  $P_v = \sigma P_o$  is to obtain terms that allow the inclusion of the Equation (4.6) into Equation (4.9). Thus,  $P_o$  and  $P_t$  are presented in the first two terms on the right side of the Equation (4.9) now.

Adding and subtracting  $\gamma_t P_o$  in Equation (4.9), we have

$$\begin{aligned} \bar{P}_d' - \bar{P}_s' &= P_o(\gamma_t - \sigma) - \gamma_t(P_o - P_t) + \\ &+ \frac{\rho}{2} \{ V_{3t}^2 [\alpha_t - K_D' \alpha_d (a - 1)^2] - V_{2v}^2 (1 + K_S') \} \end{aligned} \quad (4.10)$$

Substituting the Equation (4.6) into Equation (4.10), it turns

$$\begin{aligned} \bar{P}_d' - \bar{P}_s' &= P_o(\gamma_t - \sigma) - \gamma_t \delta \rho [V_{3t}^2(1 + 0.5K_M) - V_{1n}^2 R - V_{2v}^2(1 - R)] + \\ &+ \frac{\rho}{2} \{V_{3t}^2[\alpha_t - K_D' \alpha_d(a - 1)^2] - V_{2v}^2(1 + K_S')\} \end{aligned} \quad (4.11)$$

Substituting the relation  $V_{3t} = V_{1n}R(1 + M)$  (WINOTO; LI; SHAH, 2000) into Equation (4.11), we have

$$\begin{aligned} \bar{P}_d' - \bar{P}_s' &= P_o(\gamma_t - \sigma) - \gamma_t \delta \rho [V_{1n}^2 R^2(1 + M)^2(1 + 0.5K_M) - V_{1n}^2 R - \\ &- V_{2v}^2(1 - R)] + \frac{\rho}{2} \{V_{1n}^2 R^2(1 + M)^2[\alpha_t - K_D' \alpha_d(a - 1)^2] - V_{2v}^2(1 + K_S')\} \end{aligned} \quad (4.12)$$

Dividing all terms in the right side of Equation (4.12) by  $V_{1n}^2$  and applying the relation  $\bar{V} = V_{2v}/V_{1n}$  (WINOTO; LI; SHAH, 2000), we obtain

$$\begin{aligned} \bar{P}_d' - \bar{P}_s' &= \frac{P_o(\gamma_t - \sigma)}{V_{1n}^2} - \gamma_t \delta \rho [R^2(1 + M)^2(1 + 0.5K_M) - R - \bar{V}^2(1 - R)] + \\ &+ \frac{\rho}{2} \{R^2(1 + M)^2[\alpha_t - K_D' \alpha_d(a - 1)^2] - \bar{V}^2(1 + K_S')\} \end{aligned} \quad (4.13)$$

Substituting the relation  $\bar{V} = RM/(1 - R)$  (WINOTO; LI; SHAH, 2000) in Equation (4.13), it becomes

$$\begin{aligned} \bar{P}_d' - \bar{P}_s' &= \frac{P_o(\gamma_t - \sigma)}{V_{1n}^2} - \gamma_t \delta \rho \left[ R^2(1 + M)^2(1 + 0.5K_M) - R - \frac{R^2 M^2}{(1 - R)} \right] + \\ &+ \frac{\rho}{2} \left\{ R^2(1 + M)^2[\alpha_t - K_D' \alpha_d(a - 1)^2] - \frac{R^2 M^2}{(1 - R)^2}(1 + K_S') \right\} \end{aligned} \quad (4.14)$$

Finally, putting  $R^2$  as a common factor in Equation (4.14), the expanded numerator of Equation (4.2) becomes

$$\begin{aligned} \bar{P}_d' - \bar{P}_s' &= \frac{P_o(\gamma_t - \sigma)}{V_{1n}^2} - \gamma_t \delta \rho R^2 \left[ (1 + M)^2 (1 + 0.5K_M) - \frac{1}{R} - \frac{M^2}{(1 - R)} \right] + \\ &+ \frac{\rho}{2} R^2 \left\{ (1 + M)^2 [\alpha_t - K_D' \alpha_d (a - 1)^2] - \frac{M^2}{(1 - R)^2} (1 + K_S') \right\} \end{aligned} \quad (4.15)$$

Using the definitions presented in Equations (3.48) and (3.50), the denominator of Equation (4.5) becomes

$$\begin{aligned} \bar{P}_i' - \bar{P}_d' &= \left\{ \gamma_n P_n + \alpha_n \rho \frac{V_{1n}^2}{2} (1 + K_N') \right\} - \\ &- \left\{ \gamma_t P_t + \frac{\rho}{2} [V_{3t}^2 \alpha_t - K_D' \alpha_d V_{3t}^2 (a - 1)^2] \right\} \end{aligned} \quad (4.16)$$

Coupling the terms with common factors,  $\rho/2$  and  $V_{3t}^2$ , and rearranging, we have

$$\bar{P}_i' - \bar{P}_d' = \gamma_n P_n - \gamma_t P_t - \frac{\rho}{2} \{ V_{3t}^2 [\alpha_t - K_D' \alpha_d (a - 1)^2] - \alpha_n V_{1n}^2 (1 + K_N') \} \quad (4.17)$$

Substituting  $P_n = \lambda P_o$  in Equation (4.17), it becomes

$$\bar{P}_i' - \bar{P}_d' = \gamma_n \lambda P_o - \gamma_t P_t - \frac{\rho}{2} \{ V_{3t}^2 [\alpha_t - K_D' \alpha_d (a - 1)^2] - \alpha_n V_{1n}^2 (1 + K_N') \} \quad (4.18)$$

The application of the relation  $P_n = \lambda P_o$  also aims to obtain terms that allow the inclusion of the Equation (4.6) into Equation (4.18). In this way,  $P_o$  and  $P_t$  appear on the first two terms on the right side of the Equation (4.9).

Adding and subtracting  $\gamma_n \lambda P_t$  in Equation (4.18), we obtain

$$\begin{aligned} \bar{P}_i' - \bar{P}_d' &= \gamma_n \lambda (P_o - P_t) + P_t (\gamma_n \lambda - \gamma_t) - \\ &- \frac{\rho}{2} \{ V_{3t}^2 [\alpha_t - K_D' \alpha_d (a - 1)^2] - \alpha_n V_{1n}^2 (1 + K_N') \} \end{aligned} \quad (4.19)$$

Substituting the Equation (4.6) into Equation (4.19), it turns

$$\bar{P}_i' - \bar{P}_d' = \gamma_n \lambda \delta \rho [V_{3t}^2 (1 + 0.5K_M) - V_{1n}^2 R - V_{2v}^2 (1 - R)] + \quad (4.20)$$

$$+ P_t(\gamma_n\lambda - \gamma_t) - \frac{\rho}{2}\{V_{3t}^2[\alpha_t - K_D'\alpha_d(a-1)^2] - \alpha_n V_{1n}^2(1 + K_N')\}$$

Substituting the relation  $V_{3t} = V_{1n}R(1 + M)$  (WINOTO; LI; SHAH, 2000) into Equation (4.20), we have

$$\begin{aligned} \bar{P}_i' - \bar{P}_a' &= \gamma_n\lambda\delta\rho[V_{1n}^2R^2(1 + M)^2(1 + 0.5K_M) - V_{1n}^2R - V_{2v}^2(1 - R)] + \\ &+ P_t(\gamma_n\lambda - \gamma_t) - \frac{\rho}{2}\{V_{1n}^2R^2(1 + M)^2[\alpha_t - K_D'\alpha_d(a-1)^2] - \alpha_n V_{1n}^2(1 + K_N')\} \end{aligned} \quad (4.21)$$

Dividing all terms in the right side of Equation (4.21) by  $V_{1n}^2$  and applying the relation  $\bar{V} = V_{2v}/V_{1n}$  (WINOTO; LI; SHAH, 2000), we have

$$\begin{aligned} \bar{P}_i' - \bar{P}_a' &= \gamma_n\lambda\delta\rho[R^2(1 + M)^2(1 + 0.5K_M) - R - \bar{V}^2(1 - R)] + \\ &+ \frac{P_t(\gamma_n\lambda - \gamma_t)}{V_{1n}^2} - \frac{\rho}{2}\{R^2(1 + M)^2[\alpha_t - K_D'\alpha_d(a-1)^2] - \alpha_n(1 + K_N')\} \end{aligned} \quad (4.22)$$

Substituting the relation  $\bar{V} = RM/(1 - R)$  (WINOTO; LI; SHAH, 2000) in Equation (4.22), it becomes

$$\begin{aligned} \bar{P}_i' - \bar{P}_a' &= \gamma_n\lambda\delta\rho \left[ R^2(1 + M)^2(1 + 0.5K_M) - R - \frac{R^2M^2}{(1 - R)} \right] + \\ &+ \frac{P_t(\gamma_n\lambda - \gamma_t)}{V_{1n}^2} - \frac{\rho}{2}\{R^2(1 + M)^2[\alpha_t - K_D'\alpha_d(a-1)^2] - \alpha_n(1 + K_N')\} \end{aligned} \quad (4.23)$$

Finally, putting  $R^2$  as a common factor in Equation (4.23), the expanded denominator of Equation (4.2) becomes

$$\bar{P}_i' - \bar{P}_a' = \gamma_n\lambda\delta\rho R^2 \left[ (1 + M)^2(1 + 0.5K_M) - \frac{1}{R} - \frac{M^2}{(1 - R)} \right] + \quad (4.24)$$

$$+ \frac{P_t(\gamma_n \lambda - \gamma_t)}{V_{1n}^2} - \frac{\rho}{2} \{R^2(1+M)^2[\alpha_t - K_D' \alpha_d(a-1)^2] - \alpha_n(1+K_N')\}$$

Coupling Equations (4.15) and (4.22), we obtain the complete equation for the corrected pressure recovery ratio ( $N'$ ), which is defined as

$$N' = \frac{P_o(\gamma_t - \sigma)}{V_{1n}^2} - \gamma_t \delta \rho R^2 \left[ (1+M)^2(1+0.5K_M) - \frac{1}{R} - \frac{M^2}{(1-R)} \right] +$$

$$+ \frac{\rho}{2} R^2 \left\{ (1+M)^2[\alpha_t - K_D' \alpha_d(a-1)^2] - \frac{M^2}{(1-R)^2}(1+K_S') \right\} / \quad (4.25)$$

$$\gamma_n \lambda \delta \rho R^2 \left[ (1+M)^2(1+0.5K_M) - \frac{1}{R} - \frac{M^2}{(1-R)} \right] + \frac{P_t(\gamma_n \lambda - \gamma_t)}{V_{1n}^2} -$$

$$- \frac{\rho}{2} \{R^2(1+M)^2[\alpha_t - K_D' \alpha_d(a-1)^2] - \alpha_n(1+K_N')\}$$

where

$$\gamma_n = \frac{\int_{A_n} (p \hat{n} \cdot \mathbf{V})_n dA_n}{P_n V_{1n} A_n} \quad (4.26)$$

$$\gamma_t = \frac{\int_{A_t} (p \hat{n} \cdot \mathbf{V})_t dA_t}{P_t V_{3t} A_t} \quad (4.27)$$

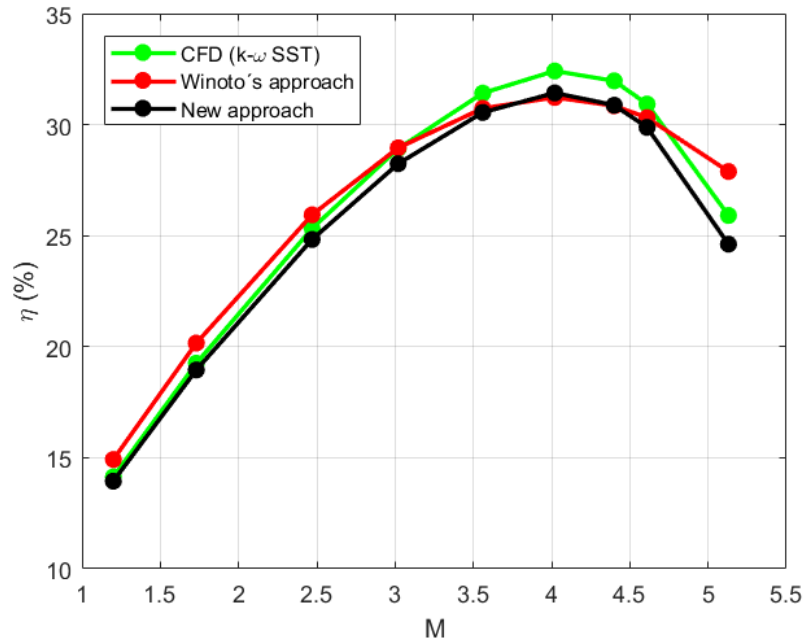
$$\alpha_n = \frac{\int_{A_n} (\mathbf{V}^3)_n dA_n}{V_{1n}^3 A_n} \quad (4.28)$$

$$\alpha_t = \frac{\int_{A_t} (\mathbf{V}^3)_t dA_t}{V_{3t}^3 A_t} \quad (4.29)$$

$$\alpha_d = \frac{\int_{A_d} (\mathbf{V}^3)_d dA_d}{V_{3d}^3 A_d} \quad (4.30)$$

The comparison between the new efficiency approach and the mathematical model proposed by WINOTO; LI; SHAH (2000) is presented in Figure 4.25, where we

Figure 4.25 – Ejector efficiency curves plotted with the simulation data, new approach and Winoto’s approach as a function of  $M$ .



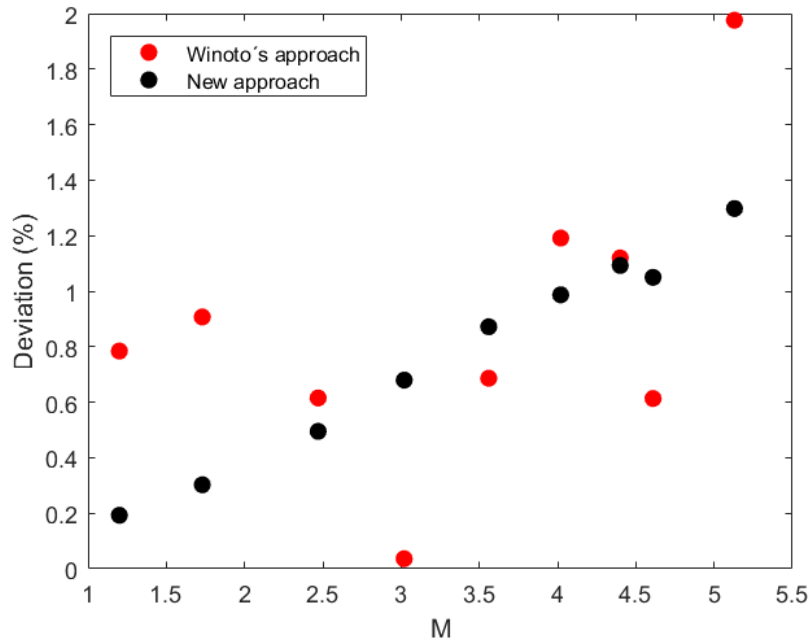
Source: Author.

can notice that the shape of new approach is slightly better adjusted to the simulation data, in comparison with the Winoto’s approach. The new approach coincides with the simulation data up to  $M = 2.47$ , and then shows a slight deviation up to the end of the efficiency curve. The new approach could also predict the operating condition that gives the efficiency peak ( $M = 4.02$ ) and the efficiency value is practically the same for both approaches at  $M = 4.02$ . In addition, the end of the simulation curve is better modeled by the new approximation instead of the Winoto’s formulation.

Deviation from the simulation data is presented for the new approach and Winoto’s approach in Figure 4.26. From this plot, we can notice that the deviation is approximately linear for the new approach and random for the Winoto’s approach. As  $M$  increases, the deviation of the new approach also increases. This linear behavior may be result of the shape similarity between the simulation data and the new approach, so that the deviation increases proportionally with the increment of  $M$ . In addition, the new approach presented lower deviation for six  $M$  values (1.20, 1.73, 2.47, 4.02, 4.40 and 5.13), while the Winoto’s approach showed lower deviation for three  $M$  values (3.02, 3.56 and 4.61).



Figure 4.26 – Deviation from simulation data plotted for the new approach and Winoto’s approach as a function of  $M$ .



Source: Author.

However, although they exist, the deviations are small (maximum of 2%) for both approaches and may be neglected, since we are dealing with a quasi-1D approach trying to model a phenomenon that occurs in three dimensions.

## 4.8 Sensitivity analysis

A sensitivity analysis was conducted in order to investigate the influence of each component on the ejector performance. The sensitivity analysis was performed by increasing 10, 20, 30, 40 and 50% in the corrected friction loss coefficients presented in Table 4.5 and in the average value of the mixing section friction loss coefficient presented in Table 4.3.

The sensitivity analysis was carried out using the new ejector’s efficiency approach ( $\eta^{new}$ ) described in the previous section due to its similar behavior in relation to the simulation data. Variations of the ejector efficiency curve due to increments on the friction loss coefficients of the nozzle ( $K_N'$ ), suction chamber ( $K_S'$ ), mixing section ( $K_M$ ) and diffuser ( $K_D'$ ) are shown, respectively, in Figures 4.27, 4.28, 4.29 and 4.30.

Due to the low values of  $K_N'$  and  $K_S'$  (see Table 4.5), the variations induced in the efficiency curves in Figures 4.27 and 4.28 are small and inconclusive. In Figure

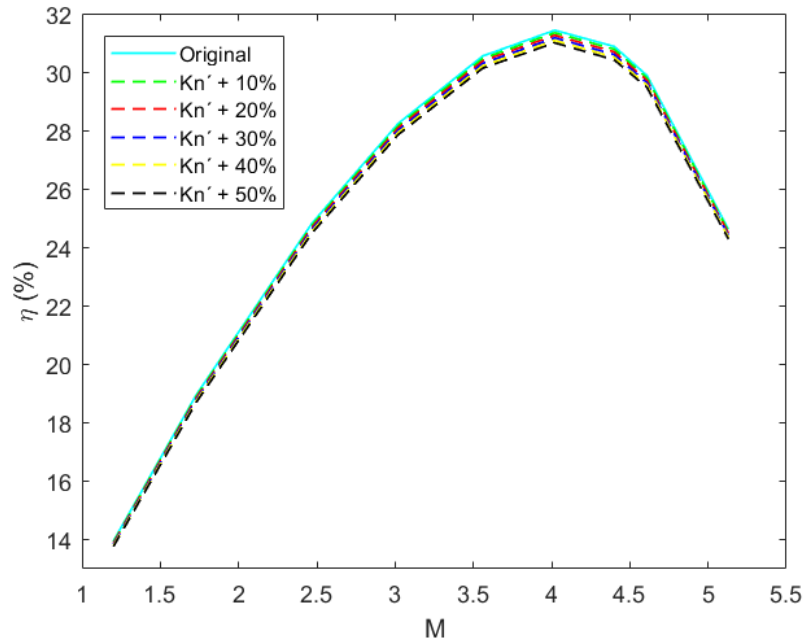
4.27, the increments in  $K_N'$  imply smooth variations in the efficiency curves for lower and higher  $M$  values, and slightly larger variations for  $M$  values close to the efficiency peak. On the other hand, Figure 4.28 shows that the efficiency curve does not change with increments in  $K_S'$  for lower  $M$  values and smoothly varies for intermediate and higher  $M$  values.

In Figure 4.29, the sensitivity for the mixing section shows small variations in the efficiency curve for lower  $M$  values and more significant variations for intermediate and higher  $M$  with increments in  $K_M$ . For the diffuser, the sensitivity analysis shows a similar behavior in comparison with the mixing section, with smooth variations for lower  $M$  values and more expressive variations for intermediate and higher  $M$  with increments in  $K_D'$  (Figure 4.30).

Another important phenomenon that can be observed in Figure 4.30 is the displacement of the ejector's efficiency peak with the increasing of the friction losses in diffuser. The efficiency peak, originally predicted for  $M = 4.02$ , moves to approximately  $M = 3.6$  with a 50% increase in  $K_D'$ . In addition, as a general comment, the ejector efficiency curve is more sensitive to friction losses for higher  $M$  instead of lower  $M$  values.

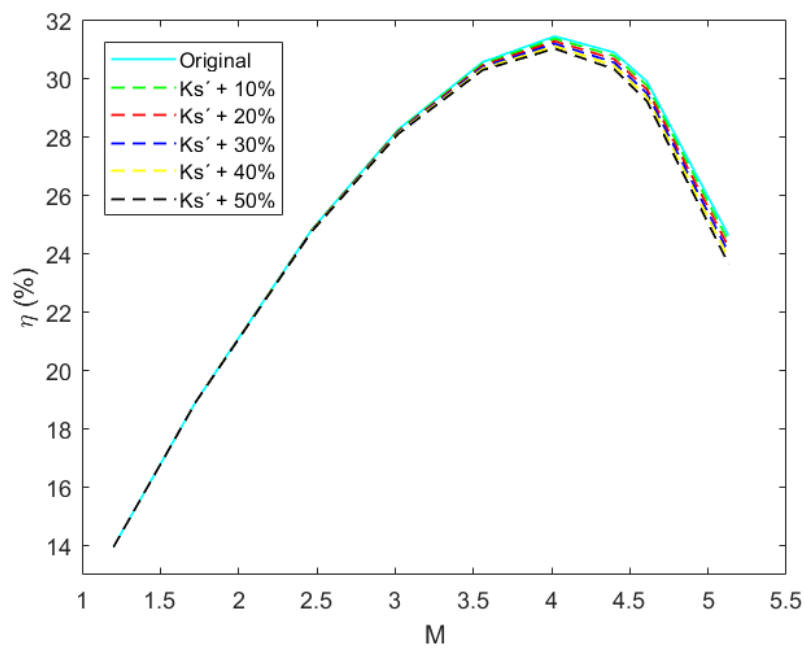
In order to ensure concrete conclusions about the sensitivity analysis, the deviations from the original efficiency curve were plotted for all the incremented friction loss coefficients of each ejector component in Figures 4.31, 4.32, 4.33 and 4.34. From Figure 4.31, we infer that the entire ejector's efficiency curve is sensitive to the nozzle, since the deviations from original curve are expressively observed for all  $M$  values. Deviations observed for the suction chamber (Figure 4.32) and diffuser (Figure 4.34) present exponential behavior, that increase with the increment of  $M$ . In contrast, deviations evaluated for the mixing section (Figure 4.33) show an approximately linear behavior, that also increase with the  $M$  incrementing.

Figure 4.27 – Sensitivity analysis of the corrected friction loss coefficient of the nozzle ( $K_N'$ ) on the ejector efficiency curve as a function of  $M$ .



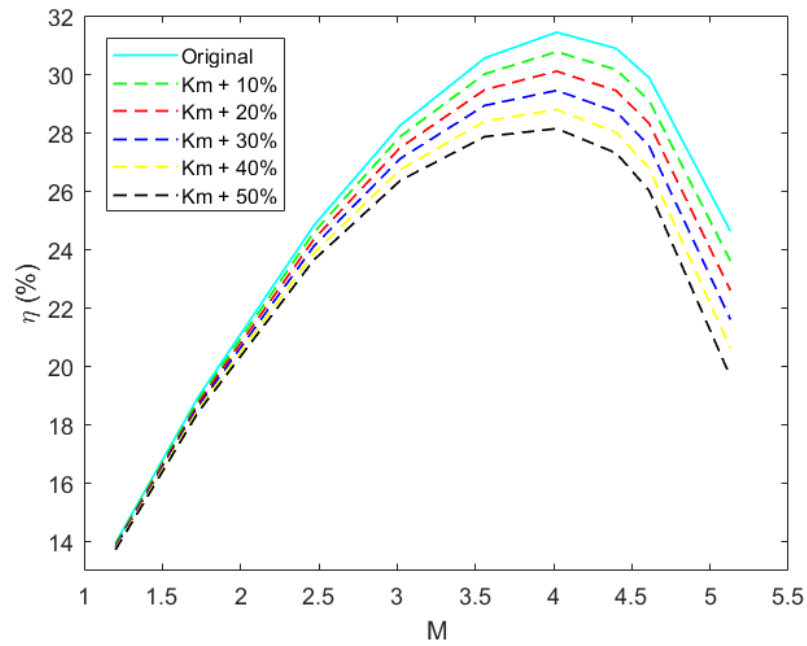
Source: Author.

Figure 4.28 – Sensitivity analysis of the corrected friction loss coefficient of the suction chamber ( $K_S'$ ) on the ejector efficiency curve as a function of  $M$ .



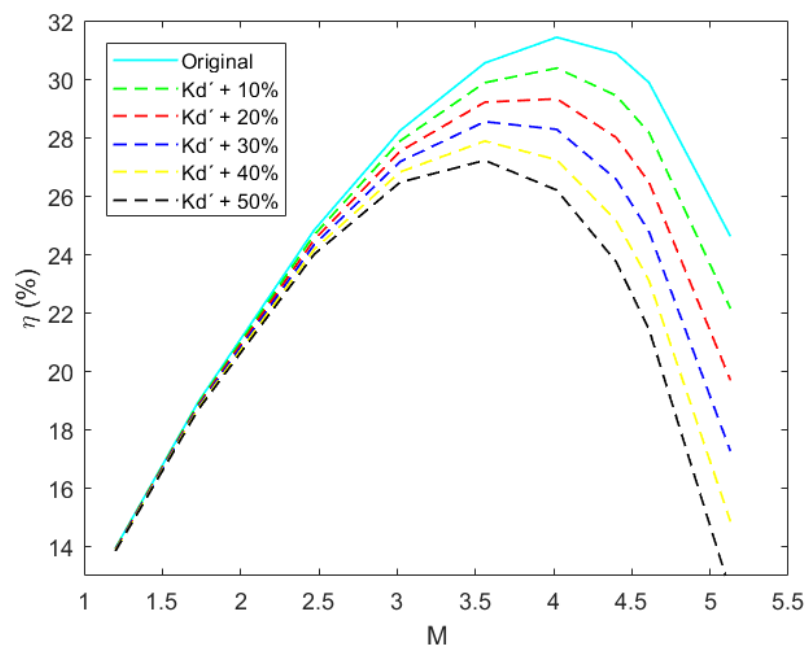
Source: Author.

Figure 4.29 – Sensitivity analysis of the friction loss coefficient of the mixing section ( $K_M$ ) on the ejector efficiency curve as a function of  $M$ .



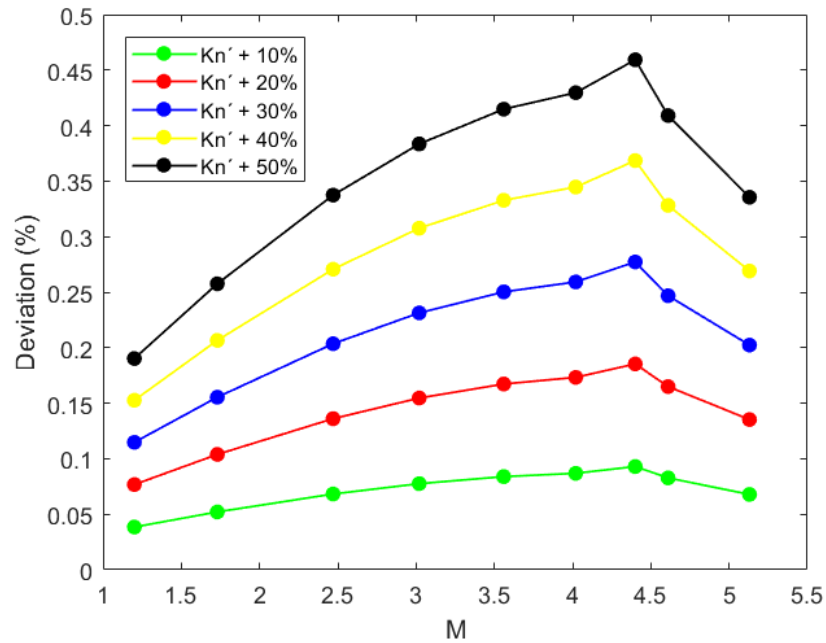
Source: Author.

Figure 4.30 – Sensitivity analysis of the corrected friction loss coefficient of the diffuser ( $K_D'$ ) on the ejector efficiency curve as a function of  $M$ .



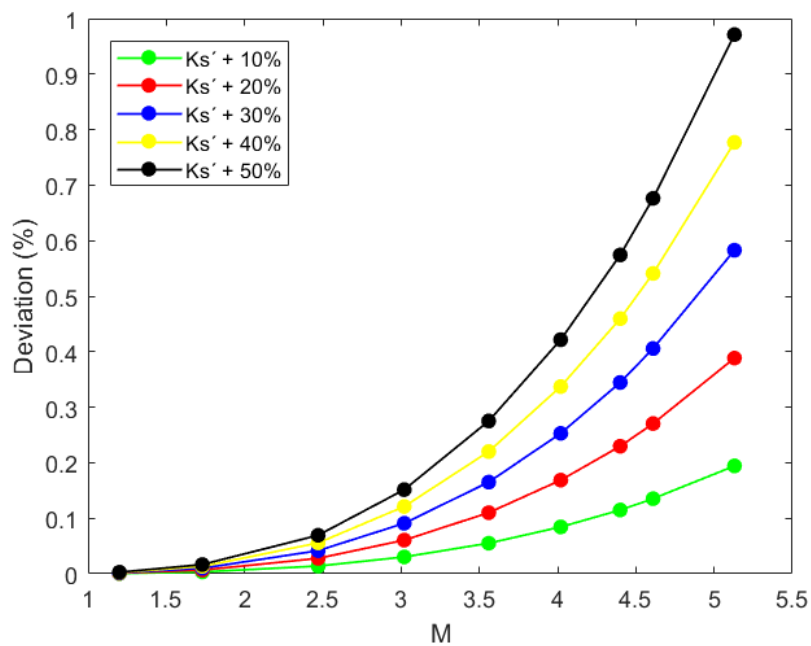
Source: Author.

Figure 4.31 – Deviation from the original efficiency curve plotted for all increments in the corrected friction loss coefficient of the nozzle ( $K_N'$ ).



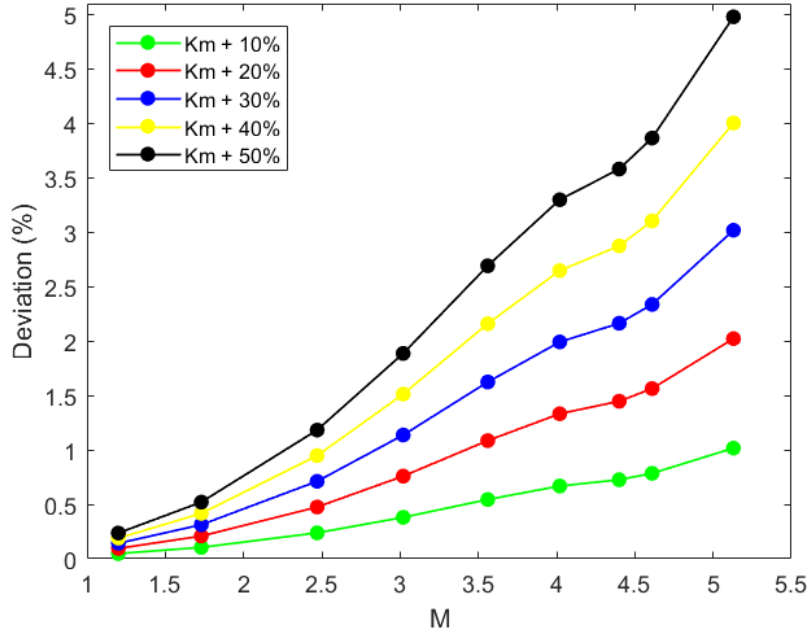
Source: Author.

Figure 4.32 – Deviation from the original efficiency curve plotted for all increments in the corrected friction loss coefficient of the suction chamber ( $K_S'$ ).



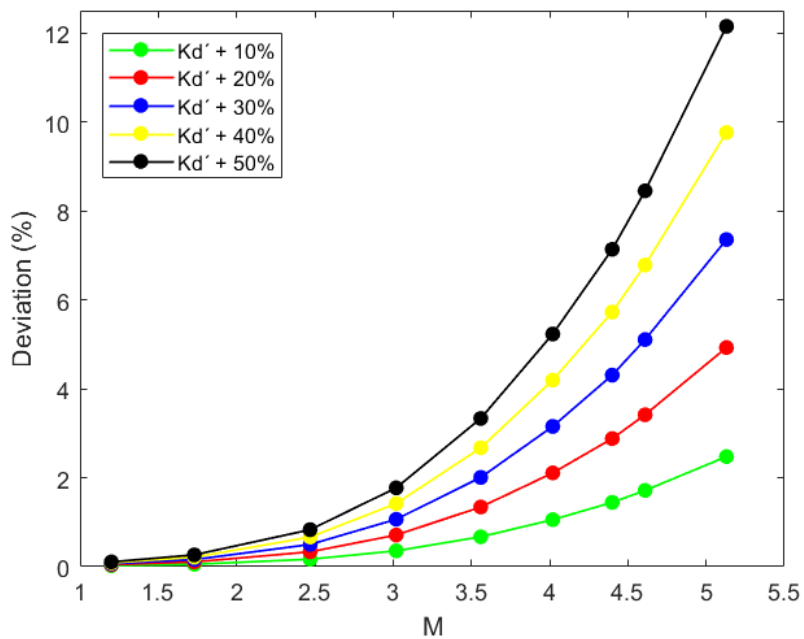
Source: Author.

Figure 4.33 – Deviation from the original efficiency curve plotted for all increments in the friction loss coefficient of the mixing section ( $K_M$ ).



Source: Author.

Figure 4.34 – Deviation from the original efficiency curve plotted for all increments in the corrected friction loss coefficient of the diffuser ( $K_D'$ ).



Source: Author.

## 4.9 Derivatives of the sensitivity curves

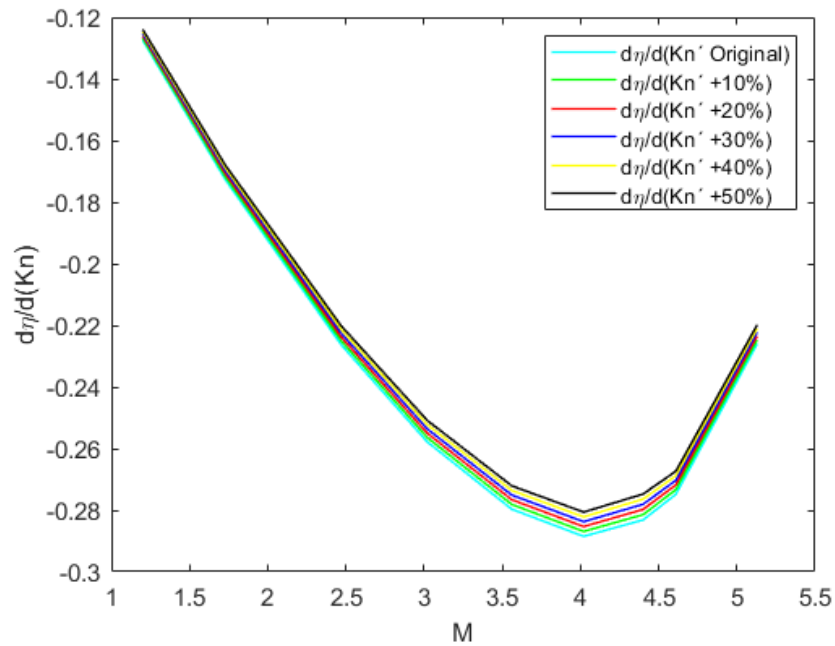
In order to verify if the sensitivity curves of the previous section were correctly determined, their numerical derivatives were calculated in relation to each friction loss coefficient ( $K_N'$ ,  $K_S'$ ,  $K_M$  and  $K_D'$ ), as respectively shown in Figures 4.35, 4.36, 4.37 and 4.38.

By comparing Figures 4.31 and 4.35, it is observed that the largest variations in the derivative curves (Figure 4.35) coincide with the regions of greatest deviations in Figure 4.31 (for  $M$  values between 3.5 and 4.5, approximately). This observation is a strong indicative that the sensitivity analysis is adequate for the nozzle.

For the suction chamber, the derivative curves plotted for all increments in  $K_S'$  are overlapping (Figure 4.36). It can be explained by the cumulative occurrence of three factors: i)  $K_S'$  presents an average value of 0.0234 (see Table 4.5), the smallest value in comparison with the other friction loss coefficients; ii) the deviations from the original efficiency curve are low for all increments in  $K_S'$  (see Figure 4.32); and iii) the deviations between the curves with incremented  $K_S'$  (see Figure 4.32) are also low. This observation may indicate that the suction chamber does not affect the efficiency curve with significance when compared to the other components of the ejector for this present study.

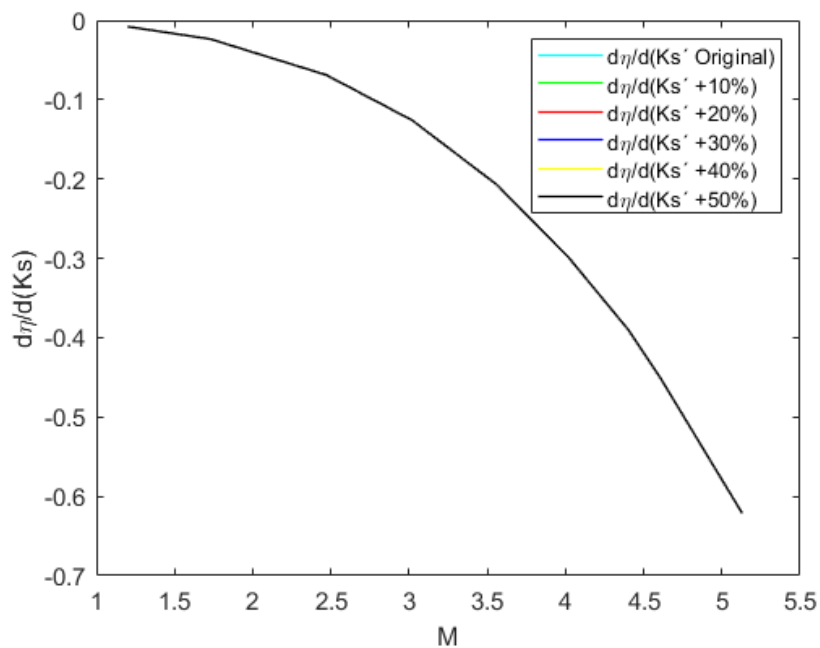
The derivative curves for the mixing section and diffuser are plotted in Figures 4.37 and 4.38, respectively. In both figures it is possible to notice that the variations in the derivative curves occur for higher and intermediate values of  $M$ , which correspond to the operating conditions that present the greatest deviation from the original efficiency curve of the ejector (see Figures 4.33 and 4.34). As observed for the nozzle, this corroboration is also a strong indicative that the sensitivity analysis is adequate for the mixing section and diffuser.

Figure 4.35 – Numerical derivatives of the efficiency curve plotted for all increments in the corrected friction loss coefficient of the nozzle ( $K_N'$ ).



Source: Author.

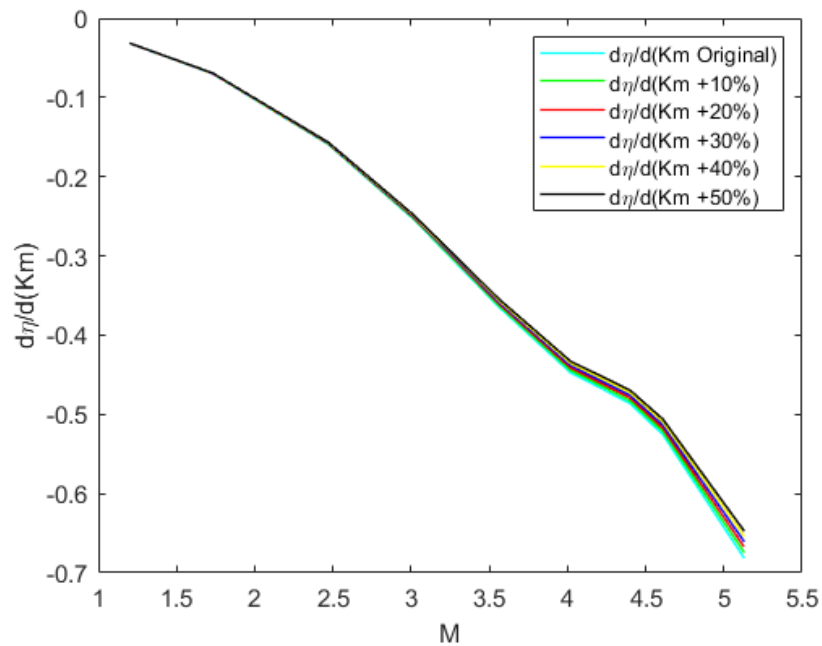
Figure 4.36 – Numerical derivatives of the efficiency curve plotted for all increments in the corrected friction loss coefficient of the suction chamber ( $K_S'$ ).



Source: Author.

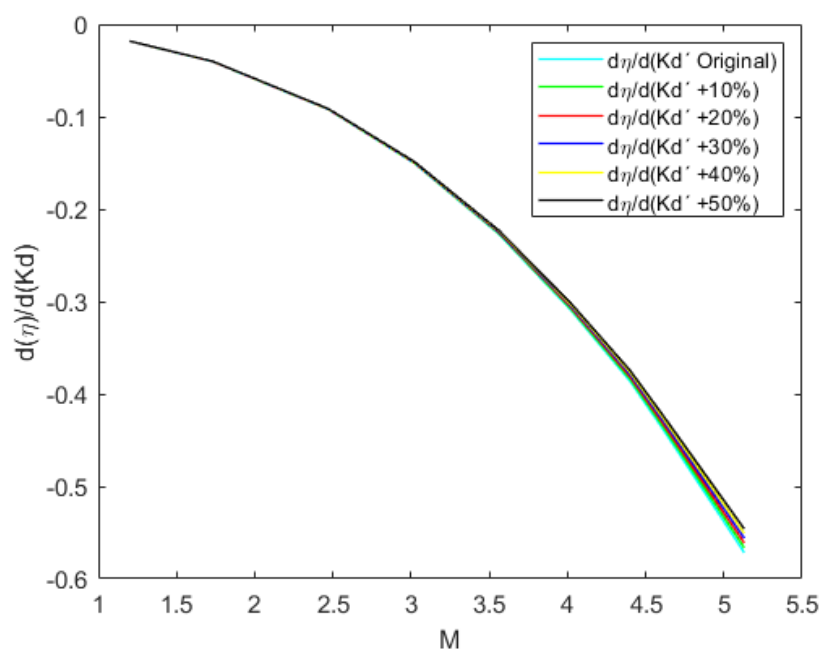


Figure 4.37 – Numerical derivatives of the efficiency curve plotted for all increments in the friction loss coefficient of the mixing section ( $K_M$ ).



Source: Author.

Figure 4.38 – Numerical derivatives of the efficiency curve plotted for all increments in the corrected friction loss coefficient of the diffuser ( $K_D'$ ).



Source: Author.

## Chapter 5

### Conclusions

*“Science never solves a problem without creating ten more”.*

*– George B. Shaw (1856 – 1950)*

In this work, a quasi-1D mathematical model from literature (WINOTO; LI; SHAH, 2000) was employed to perform a theoretical analysis of an incompressible-flow ejector, which is expected to be applied in Carbon Capture and Storage (CCS) activities in the future. The accuracy of the mathematical model adapted from the literature (WINOTO; LI; SHAH, 2000) was tested considering its effectiveness in calculating the ejector’s friction loss coefficients, delimiting the ejector’s envelope of operation and predicting the ejector’s efficiency peak. Computational Fluid Dynamics (CFD) results were used as input data into the mathematical model and validated by comparison with the experimental results from SANGER (1968).

The mathematical approach (WINOTO; LI; SHAH, 2000) assumes that pressures at the nozzle outlet ( $P_n$ ) and suction chamber outlet ( $P_v$ ) have the same value at the mixing section inlet. This hypothesis enables to express the ejector’s pressure recovery ratio ( $N$ ) as a function independent of pressure and velocity data. It is very useful for experiments, where only some geometrical parameters are known. However, it was demonstrated that  $P_n$  and  $P_v$  are significantly different at the mixing section inlet, and considering these distinct values in the mathematical formulation may be a good strategy to calculate more reliable values for the friction loss coefficients when CFD

data are available. In addition, the mathematical approach showed good accuracy to predict the ejector's maximum efficiency point and delimit its envelope of operation.

By comparing the effectiveness of  $k-\varepsilon$ ,  $k-\omega$  and  $k-\omega$  SST turbulence models, the later has proven to be the most suitable one to capture the ejector flow characteristics in all operating conditions. On the other hand, the  $k-\omega$  model was unsatisfactory for this present study.

At the ejector cross sections, the non-uniformity of the velocity and pressure profiles justified the application of the kinetic-energy ( $\alpha$ ) and pressure ( $\gamma$ ) correction factors into the CFD results. From the profiles plotted for some of the ejector sections, we could infer that: i) the uniformity of the pressure profile at the suction chamber outlet is dependent on the entrainment ratio ( $M$ ); ii) the pressure stabilization of the mixing flow occurs earlier than its velocity stabilization; and iii) the velocity stabilization occurs only inside the diffuser.

The analyzes including  $\alpha$  and  $\gamma$  allowed the formulation of a new efficiency approximation that showed better performance for specific operating conditions, including the efficiency peak, compared with the original mathematical model from literature (WINOTO; LI; SHAH, 2000). The new approximation may be a good alternative to model the ejector efficiency when CFD data are available.

A sensitivity analysis was conducted in order to investigate the influence of the friction loss coefficient of the nozzle ( $K_N'$ ), suction chamber ( $K_S'$ ), mixing section ( $K_M$ ) and diffuser ( $K_D'$ ) on the ejector performance, and showed that: i)  $K_S'$  and  $K_D'$  exponentially affect the ejector's efficiency curve, while the influence of  $K_M$  is linear; ii) the ejector's efficiency curve is sensitive to the friction losses for higher and intermediate  $M$  values for the suction chamber, mixing section and diffuser; iii)  $K_N'$  impacts the entire efficiency curve; and iv) increments in  $K_D'$ , in addition to reducing the equipment efficiency, can displace the ejector's efficiency peak.

# Bibliography

- ABDEL-HAMID, A. A.; MAHMOUD, N. H.; HAMED, Mofreh H.; HUSSIEN, A. A. Gas-solid flow through the mixing duct and tail section of ejectors: Experimental studies. **Powder Technology**, v. 328, p. 148–155, 2018. DOI: 10.1016/j.powtec.2018.01.011.
- ABDULATEEF, J. M.; SOPIAN, K.; ALGHOUL, M. A.; SULAIMAN, M. Y. Review on solar-driven ejector refrigeration technologies. **Renewable and Sustainable Energy Reviews**, v. 13, p. 1338–1349, 2009. DOI: 10.1016/j.rser.2008.08.012.
- ANDERSON, T. R.; HAWKINS, E.; JONES, P. D. CO<sub>2</sub>, the greenhouse effect and global warming: from the pioneering work of Arrhenius and Callendar to today's Earth System Models. **Endeavour**, v. 40, n. 3, p. 178–187, 2016. DOI: 10.1016/j.endeavour.2016.07.002.
- ANTONIO, Y. M.; PÉRILHON, C.; DESCOMBES, G.; CHACOUX, C. Thermodynamic modelling of an ejector with compressible flow by a one-dimensional approach. **Entropy**, v. 14, n. 4, p. 599–613, 2012. DOI: 10.3390/e14040599.
- APHORN RATANA, S.; EAMES, I. W. A small capacity steam-ejector refrigerator: Experimental investigation of a system using ejector with movable primary nozzle. **International Journal of Refrigeration**, v. 20, n. 5, p. 352–358, 1997. DOI: 10.1016/S0140-7007(97)00008-X.
- ARBEL, A.; SHKLYAR, A.; HERSHGAL, D.; BARAK, M.; SOKOLOV, M. Ejector irreversibility characteristics. **Journal of Fluids Engineering**, v. 125, n. 1, p. 121–129, 2003. DOI: 10.1115/1.1523067.
- ASFORA, L.; SANTOS, A.; DUARTE, L. Modeling multiphase jet pumps for gas compression. **Journal of Petroleum Science and Engineering**, v. 173, p. 844–852, 2019. DOI: 10.1016/j.petrol.2018.10.036.
- BAEK, S.; KO, S.; SONG, S.; RYU, S. Numerical study of high-speed two-phase ejector performance with R134a refrigerant. **International Journal of Heat and Mass Transfer**, v. 126, p. 1071–1082, 2018. DOI: 10.1016/j.ijheatmasstransfer.2018.05.053.
- BANASIAK, K.; HAFNER, A.; ANDRESEN, T. Experimental and numerical investigation of the influence of the two-phase ejector geometry on the performance of the R744 heat pump. **International Journal of Refrigeration**, v. 35, n. 6, p. 1617–1625, 2012. DOI: 10.1016/j.ijrefrig.2012.04.012.
- BESAGNI, G.; MEREU, R.; INZOLI, F. Ejector refrigeration: A comprehensive review. **Renewable and Sustainable Energy Reviews**, v. 53, p. 373–407, 2016. DOI: 10.1016/j.rser.2015.08.059.
- BHAVIKATTI, S. S. **Finite Element Analysis**. New Age International Ltd., 2005.

- BOUHANGUEL, A.; DESEVAUX, P.; GAVIGNET, E. Flow visualization in supersonic ejectors using laser tomography techniques. **International Journal of Refrigeration**, v. 34, n. 7, p. 1633–1640, 2011. DOI: 10.1016/j.ijrefrig.2010.08.017
- CARRILLO, J. A. E.; DE LA FLOR, F. J. S.; LISSÉN, J. M. S. Thermodynamic comparison of ejector cooling cycles. Ejector characterisation by means of entrainment ratio and compression efficiency. **International Journal of Refrigeration**, v. 74, p. 371–384, 2017. DOI: 10.1016/j.ijrefrig.2016.11.006.
- CHEN, W.; LIU, M.; CHONG, D.; YAN, J.; LITTLE, A. B.; BARTOSIEWICZ, Y. A 1D model to predict ejector performance at critical and sub-critical operational regimes. **International Journal of Refrigeration**, v. 36, n. 6, p. 1750–1761, 2013. DOI: 10.1016/j.ijrefrig.2013.04.009.
- COMSOL Multiphysics. **COMSOL Multiphysics User's Guide**, 2012.
- CUNNINGHAM, R. G. Jet-pump theory and performance with fluid of high viscosity. **Trans. ASME**, v. 79, p. 1807–1820, 1957.
- CUNNINGHAM, R. G. **Jet Pump Theory**. In: *Jet Pumps*, 2001.
- EL-DESSOUKY, H. ETTOUNEY, H.; ALATIQUI, I.; AL-NUWAIBIT, G. Evaluation of steam jet ejectors. **Chemical Engineering and Processing**, v. 41, n. 6, p. 551–561, 2002. DOI: 10.1016/S0255-2701(01)00176-3.
- EL GAZZAR, M.; MEAKHAIL, T.; MIKHAIL, S. Numerical study of flow inside an annular jet pump. **Journal of Thermophysics and Heat Transfer**, v. 20, n. 4, p. 930–932, 2006. DOI: 10.2514/1.18104.
- ELBEL, S. Historical and present developments of ejector refrigeration systems with emphasis on transcritical carbon dioxide air-conditioning applications. **International Journal of Refrigeration**, v. 34, n. 7, p. 1545–1561, 2011. DOI: 10.1016/j.ijrefrig.2010.11.011.
- ELHUB, B.; MAT, S.; SOPIAN, K.; ELBREKI, A. M.; RUSLAN, M. H.; AMMAR, A. A. Performance evaluation and parametric studies on variable nozzle ejector using R134A. **Case Studies in Thermal Engineering**, v. 12, p. 258–270, 2018. DOI: 10.1016/j.csite.2018.04.006.
- FALSAFIOON, M.; AIDOUN, Z.; POIRIER, M. A Numerical and Experimental Study of Ejector Internal Flow Structure and Geometry Modification for Maximized Performance. **IOP Conference Series: Materials Science and Engineering**, v. 280, n. 1, 2017. DOI: 10.1088/1757-899X/280/1/012011.
- FAN, J.; EVES, J.; THOMPSON, H. M.; TOROPOV, V. V.; KAPUR, N.; COPLEY, D.; MINCHER, A. Computational fluid dynamic analysis and design optimization of jet pumps. **Computers and Fluids**, v. 46, n. 1, p. 212–217, 2011. DOI: 10.1016/j.compfluid.2010.10.024.
- FERZIGER, J. H.; PERIC, M. **Computational Methods for Fluid Dynamics**. 3. ed.

- Springer, 2002.
- FORTUNA, A. de O. **Técnicas Computacionais para Dinâmica dos Fluidos: Conceitos Básicos e Aplicações**. Edusp, 2000.
- FU, W.; LI, Y.; LIU, Z.; WU, H.; WU, T. Numerical study for the influences of primary nozzle on steam ejector performance. **Applied Thermal Engineering**, v. 106, p. 1148–1156, 2016. DOI: 10.1016/j.applthermaleng.2016.06.111.
- GALANIS, N.; SORIN, M. Ejector design and performance prediction. **International Journal of Thermal Sciences**, v. 104, p. 315–329, 2016. DOI: 10.1016/j.ijthermalsci.2015.12.022.
- GOSLINE, J. E.; O'BRIEN, M. P. **The water jet pump**. University of California Publications, 1934.
- GOSNEY, W. B. **Principles of refrigeration**. Cambridge University Press, 1982.
- GRUPPING, A. W.; COPPES, J. L. R.; GROOT, J. G. Fundamentals of Oilwell Jet Pumping. **SPE Production Engineering**, p. 9–14, 1988.
- HAMZAOU, M.; NESREDDINE, H.; AIDOUN, Z.; BALISTROU, M. Experimental study of a low grade heat driven ejector cooling system using the working fluid R245fa. **International Journal of Refrigeration**, v. 86, p. 388–400, 2018. DOI: 10.1016/j.ijrefrig.2017.11.018.
- HATZLAVRAMIDIS, D. T. Modelling and Design of Jet Pumps. **SPE Production Engineering**, v. 6, n. 4, p. 413–419, 1991. DOI: 10.2118/19713-pa.
- HE, S.; LI, Y.; WANG, R. Z. Progress of mathematical modeling on ejectors. **Renewable and Sustainable Energy Reviews**, v. 13, n. 8, p. 1760–1780, 2009. DOI: 10.1016/j.rser.2008.09.032.
- HIRSH, Charles. **Numerical Computation of Internal & External Flows**. 2. ed. Butterworth-Heinemann, 2007.
- HU, J.; SHI, J.; LIANG, Y.; YANG, Z.; CHEN, J. Numerical and experimental investigation on nozzle parameters for R410A ejector air conditioning system. **International Journal of Refrigeration**, v. 40, p. 338–346, 2014. DOI: 10.1016/j.ijrefrig.2013.12.008.
- HUANG, B. J.; CHANG, J. M.; WANG, C. P.; PETRENKO, V. A. 1-D analysis of ejector performance. **International Journal of Refrigeration**, v. 22, n. 5, p. 354–364, 1999. DOI: 10.1016/S0140-7007(99)00004-3.
- INTERNATIONAL ENERGY AGENCY. **World Energy Outlook 2015**. International Energy Agency, 2015a.
- INTERNATIONAL ENERGY AGENCY. **Carbon Capture and Storage: The solution for deep emissions reductions**. International Energy Agency, 2015b.
- INTERNATIONAL ENERGY AGENCY. **Energy Technology Perspectives 2015**. International Energy Agency, 2015c.

- ISKANDARANI, Mohamed. **Numerical Methods in Fluid Dynamics**. Lecture Notes for Numerical Methods in Ocean Modeling, 2010.
- KEENAN, J., H.; NEUMANN, E., P. A simple air ejector. **ASME Journal of Applied Mechanics**, v. 64, p. 75–82, 1942.
- KEENAN, J. H. An investigation of ejector design by analysis and experiment. **Journal of Applied Mechanics**, v. 17, p. 299, 1950.
- KIM, H. D.; LEE, J. H.; SETOGUCHI, T.; MATSUO, S. Computational analysis of a variable ejector flow. **Journal of Thermal Science**, v. 15, n. 2, p. 140–144, 2006. DOI: 10.1007/s11630-006-0140-5.
- KONG, F.; JIN, Y.; SETOGUCHI, T.; KIM, H. D. Numerical analysis of Chevron nozzle effects on performance of the supersonic ejector-diffuser system. **Journal of Thermal Science**, v. 22, n. 5, p. 459–466, 2013. DOI: 10.1007/s11630-013-0648-4.
- KORNHAUSER, A. A. The Use of an Ejector as a Refrigerant Expander. **Proceedings of the International Refrigeration and Air Conditioning Conference**, v. 5, p. 10–19, 1990.
- KRACÍK, J.; DVOŘÁK, V.. Experimental and numerical investigation of an air to air supersonic ejector for propulsion of a small supersonic wind tunnel. **EPJ Web of Conferences**, v. 92, p. 1–5, 2015. DOI: 10.1051/epjconf/20159202038.
- LAUNDER, B. E.; SPALDING, D. B. The Numerical Computation of Turbulent Flows. **Computer Methods in Applied Mechanical Engineering**, v. 3, p. 269–289, 1974.
- LEE, M. S.; LEE, H.; HWANG, Y.; RADERMACHER, R.; JEONG, H. M. Optimization of two-phase R600a ejector geometries using a non-equilibrium CFD model. **Applied Thermal Engineering**, v. 109, p. 272–282, 2016. DOI: 10.1016/j.applthermaleng.2016.08.078.
- LI, C.; LI, Y. Z. Investigation of entrainment behavior and characteristics of gas-liquid ejectors based on CFD simulation. **Chemical Engineering Science**, v. 66, n. 3, p. 405–416, 2011. DOI: 10.1016/j.ces.2010.10.041.
- LITTLE, A. B.; GARIMELLA, S.; DIPRETE, J. P. Combined effects of fluid selection and flow condensation on ejector operation in an ejector-based chiller. **International Journal of Refrigeration**, v. 69, p. 1–16, 2016. DOI: 10.1016/j.ijrefrig.2016.04.011.
- LIU, F.; GROLL, E. A. Analysis of a Two Phase Flow Ejector for the Transcritical CO<sub>2</sub> Cycle. **International Refrigeration and Air Conditioning Conference at Purdue**, p. 1–10, 2008.
- LIU, J.; WANG, L.; JIA, L.; WANG, X. The influence of the area ratio on ejector efficiencies in the MED-TVC desalination system. **Desalination**, v. 413, p. 168–175, 2017. DOI: 10.1016/j.desal.2017.03.017.

- LONG, X.; HAN, N.; CHEN, Q. Influence of nozzle exit tip thickness on the performance and flow field of jet pump. **Journal of Mechanical Science and Technology**, v. 22, n. 10, p. 1959–1965, 2008. DOI: 10.1007/s12206-008-0739-4.
- MENTER, F. R. Influence of freestream values on k-omega turbulence model predictions. **AIAA Journal**, v. 30, n. 6, p. 1657–1659, 1992a.
- MENTER, F. R. **Improved two-equation k-omega turbulence models for aerodynamic flows**. NASA Technical Memorandum TM-103975, Ames, CA, 1992b.
- MENTER, F. R. Eddy viscosity transport equations and their relation to the k- $\epsilon$  model. **Journal of Fluids Engineering**, v. 119, n. 4, p. 876–884, 1997. DOI: 10.1115/1.2819511.
- MENTER, F. R. Two-equation eddy-viscosity turbulence models for engineering applications. **AIAA Journal**, v. 32, n. 8, p. 1598–1605, 1994.
- MERCER, J. H. West Antarctic ice sheet and CO<sub>2</sub> greenhouse effect: A threat of disaster. **Nature**, v. 271, p. 321–325, 1978. DOI: 10.1038/271321a0.
- MORAN, M. J.; SHAPIRO, H. N.; BOETTNER, D. D. **Fundamentals of Engineering Thermodynamics**. 7. ed. Don Fowley, 2011.
- MUELLER, N. H. G. Water jet pump. **Journal of the Hydraulics Division**, v. 90, n. 3, p. 83–113, 1964.
- MUNDAY, J. T.; BAGSTER, D. F. A New Ejector Theory Applied to Steam Jet Refrigeration. **Industrial and Engineering Chemistry Process Design and Development**, v. 16, n. 4, p. 442–449, 1977. DOI: 10.1021/i260064a003.
- MUNSON, B. R.; YOUNG, D. F.; OKIISHI, T. H. **Fundamentals of fluid mechanics**. 7. ed. John Wiley & Sons Inc, 2013.
- NEVE, R. S. Diffuser performance in two-phase jet pumps. **International Journal of Multiphase Flow**, v. 17, n. 2, p. 267–272, 1991. DOI: 10.1016/0301-9322(91)90019-Y.
- PALACZ, M.; SMOLKA, J.; KUS, W.; FIC, A.; BULINSKI, Z.; NOWAK, A. J.; BANASIAK, K.; HAFNER, A. CFD-based shape optimisation of a CO<sub>2</sub> two-phase ejector mixing section. **Applied Thermal Engineering**. v. 95, p. 62–69, 2016. DOI: 10.1016/j.applthermaleng.2015.11.012.
- PARK, B. H.; LIM, J. H.; YOON, W. Fluid dynamics in starting and terminating transients of zero-secondary flow ejector. **International Journal of Heat and Fluid Flow**, v. 29, p. 327–339, 2008. DOI: 10.1016/j.ijheatfluidflow.2007.06.008.
- PEDROSO, M. C. **Dinâmica dos fluidos computacional aplicada a ejetores**. Dissertação de Mestrado. Universidade Estadual de Campinas, 2015.
- PHITAKWINAI, S.; THEPA, S.; NILNONT, W. Effect of nozzle position on water ejector efficiency. **KKU Engineering Journal**, v. 40, n. S2, p. 196–198, 2016. DOI:



- 10.14456/kkuenj.2016.87.
- POTTER, M. C.; WIGGERT, D. C.; RAMADAN, B. H. **Mechanics of Fluids**. 4. ed. Cengage Learning, 2010.
- RACKLEY, S. **Carbon Capture and Storage**. Elsevier, 2010.
- RAMESH, A. S.; SEKHAR, J. S. Experimental studies on the effect of suction chamber angle on the entrainment of passive fluid in a steam ejector. **Journal of Fluids Engineering, Transactions of the ASME**, v. 140, n. 1, p. 1–8, 2018. DOI: 10.1115/1.4037692.
- RANKINE, W. J. M. On the mathematical theory of combined streams. **Lond. and Edin.**, p. 90–94, 1870.
- REDDY, Y. R.; KAR, S. Theory and Performance of Water Jet Pump. **Journal of the Hydraulics Division**, v. 94, n. 5, p. 1261–1282, 1968.
- RIFFAT, S. B.; GAN, G.; SMITH, S. Computational fluid dynamics applied to ejector heat pumps. **Applied Thermal Engineering**, v. 16, n. 4, p. 291–297, 1996. DOI: 10.1016/1359-4311(95)00033-X.
- RITM Industry. **Pneumatica Conveying: Pumps, Valves, Piping...** Disponível em: [www.google.com/imgres?imgurl=http%3A%2F%2Fritmindustry.com%2Fupload%2Fitems%2F110%2F110092.jpg&imgrefurl=http%3A%2F%2Fritmindustry.com%2Fcatalog%2Fpneumatic-conveying-pumps-valves-piping%2Fventuri-ejector-2%2F&docid=\\_vvTrbMdl-UiRM&tbnid=AaGqoq4gHRcZNM%3A&vet=12ahUKEwi57qO3hK7mAhX3JLkGHX9fAc84yAEQMygZMBI6BAgBEBo..i&w=800&h=800&itg=1&bih=833&biw=1280&q=ejector in industry&ved=2ahUKEwi57qO3hK7mAhX3JLkGHX9fAc84yAEQMygZMBI6BAgBEBo&iact=mrc&uact=8](http://www.google.com/imgres?imgurl=http%3A%2F%2Fritmindustry.com%2Fupload%2Fitems%2F110%2F110092.jpg&imgrefurl=http%3A%2F%2Fritmindustry.com%2Fcatalog%2Fpneumatic-conveying-pumps-valves-piping%2Fventuri-ejector-2%2F&docid=_vvTrbMdl-UiRM&tbnid=AaGqoq4gHRcZNM%3A&vet=12ahUKEwi57qO3hK7mAhX3JLkGHX9fAc84yAEQMygZMBI6BAgBEBo..i&w=800&h=800&itg=1&bih=833&biw=1280&q=ejector in industry&ved=2ahUKEwi57qO3hK7mAhX3JLkGHX9fAc84yAEQMygZMBI6BAgBEBo&iact=mrc&uact=8). Acesso em: 31 jul. 2020.
- SADEGHI, M.; YARI, M.; MAHMOUDI, S. M. S.; JAFARI, M.. Thermodynamic analysis and optimization of a novel combined power and ejector refrigeration cycle – Desalination system. **Applied Energy**, v. 208, p. 239–251, 2017. DOI: 10.1016/j.apenergy.2017.10.047.
- SANAYE, S.; NIROOMAND, B. Vertical ground coupled steam ejector heat pump; Thermal-economic modeling and optimization. **International Journal of Refrigeration**, v. 34, n. 7, p. 1562–1576, 2011. DOI: 10.1016/j.ijrefrig.2010.03.004.
- SANGER, N. L. An Experimental Investigation of Several. **Transactions of the ASME**, p. 11–19, 1970.
- SANGER, N. L. Noncavitating and cavitating performance of two low-area-ratio water jet pumps with throat lengths of 5.66 diameters. **Nasa Technical Note**, 1968.
- SHAH, A.; CHUGHTAI, I. R.; INAYAT, M. H. Experimental study of the characteristics of

- steam jet pump and effect of mixing section length on direct-contact condensation. **International Journal of Heat and Mass Transfer**, v. 58, p. 62–69, 2013. DOI: 10.1016/j.ijheatmasstransfer.2012.11.048.
- SHESTOPALOV, K. O.; HUANG, B. J.; PETRENKO, V. O.; VOLOVYK, O. S. Investigation of an experimental ejector refrigeration machine operating with refrigerant R245fa at design and off-design working conditions. Part 1. Theoretical analysis. **International Journal of Refrigeration**, v. 55, p. 201–211, 2015. DOI: 10.1016/j.ijrefrig.2015.01.016.
- TEAM Tech AS. **TeamTec AS - Simply better**. Disponível em: [www.google.com/imgres?imgurl=http%3A%2F%2Fwww.worldcruiseindustryreview.com%2Fuploads%2Fstorefront%2F22457%2Fimages%2F256906%2Fsmall%2Fejector%2520jpg.jpg&imgrefurl=http%3A%2F%2Fwww.worldcruiseindustryreview.com%2Fcontractors%2Fenvironmental-issues%2Fteamtec-as%2F&docid=duKZIQAcn7xxYM&tbnid=yVEnM1cJvBYEfM%3A&vet=12ahUKEwjF4\\_L7hq7mAhV9JrkGHYpOCQc4ZBAzKCcwJ3oECAEQLA..i&w=600&h=450&bih=772&biw=1280&q=ejectorindustry&ved=2ahUKEwjF4\\_L7hq7mAhV9JrkGHYpOCQc4ZBAzKCcwJ3oECAEQLA&iact=mrc&uact=8](http://www.google.com/imgres?imgurl=http%3A%2F%2Fwww.worldcruiseindustryreview.com%2Fuploads%2Fstorefront%2F22457%2Fimages%2F256906%2Fsmall%2Fejector%2520jpg.jpg&imgrefurl=http%3A%2F%2Fwww.worldcruiseindustryreview.com%2Fcontractors%2Fenvironmental-issues%2Fteamtec-as%2F&docid=duKZIQAcn7xxYM&tbnid=yVEnM1cJvBYEfM%3A&vet=12ahUKEwjF4_L7hq7mAhV9JrkGHYpOCQc4ZBAzKCcwJ3oECAEQLA..i&w=600&h=450&bih=772&biw=1280&q=ejectorindustry&ved=2ahUKEwjF4_L7hq7mAhV9JrkGHYpOCQc4ZBAzKCcwJ3oECAEQLA&iact=mrc&uact=8). Acesso em: 31 jul. 2020.
- THOMAS, J. E. **Fundamentos de Engenharia de Petróleo**. 1. ed. Rio de Janeiro: Editora Interciência Ltda., 2001.
- UNITED NATIONS. **About the Sustainable Development Goals**. 2015. Disponível em: <https://www.un.org/sustainabledevelopment/sustainable-development-goals/>. Acesso em: 31 jul. 2020.
- VARGA, S.; OLIVEIRA, A. C.; DIACONU, B. Influence of geometrical factors on steam ejector performance - A numerical assessment. **International Journal of Refrigeration**, v. 32, n. 7, p. 1694–1701, 2009. DOI: 10.1016/j.ijrefrig.2009.05.009.
- VERSTEEG, H. K.; MALALASEKERA, W. **An Introduction to Computational Fluid Dynamics**. 2. ed. Pearson Education Limited, 2007.
- VOGEL, R. Theoretical and experimental investigation of air ejectors. **Maschinenbautechnik**, v. Berlin, n. 5, p. 619–637, 1956.
- WANG, C.; WANG, L.; WANG, X.; ZHAO, H. Design and numerical investigation of an adaptive nozzle exit position ejector in multi-effect distillation desalination system. **Energy**, v. 140, p. 673–681, 2017. DOI: 10.1016/j.energy.2017.08.104.
- WANG, X.; YU, J. An investigation on the component efficiencies of a small two-phase ejector. **International Journal of Refrigeration**, v. 71, p. 26–38, 2016. DOI: 10.1016/j.ijrefrig.2016.08.006.
- WATANAWANAVET, Somsak. **CFD Optimization Study of High-Efficiency Jet**

- Ejectors**. PhD Dissertation: Texas A&M University, 2008.
- WILCOX, D. C. Turbulence Modelling for CFD. **DCW Industries Inc., La Canada, California**, 1993a.
- WILCOX, D. C. Reassessment of the scale-determining equation for advanced turbulence models. **AIAA Journal**, v. 26, n. 11, p. 1299–1310, 1988. DOI: 10.2514/3.10041.
- WILCOX, D. C. Comparison of two-equation turbulence models for boundary layers with pressure gradient. **AIAA Journal**, v. 31, n. 8, p. 1414–1421, 1993b. DOI: 10.2514/3.11790.
- WILCOX, D. C. Simulation of transition with a two-equation turbulence model. **AIAA Journal**, v. 32, n. 2, p. 247–255, 1994. DOI: 10.2514/3.59994.
- WINOTO, S. H.; LI, H.; SHAH, D. A. Efficiency of Jet Pumps. **Journal of Hydraulic Engineering**, v. 126, n. 2, p. 150–156, 2000.
- WU, H.; LIU, Z.; HAN, B.; LI, Y.. Numerical investigation of the influences of mixing chamber geometries on steam ejector performance. **Desalination**, v. 353, p. 15–20, 2014. DOI: 10.1016/j.desal.2014.09.002.
- WU, Y.; ZHAO, H.; ZHANG, C.; WANG, L.; HAN, J.. Optimization analysis of structure parameters of steam ejector based on CFD and orthogonal test. **Energy**, v. 151, p. 79–93, 2018. DOI: 10.1016/j.energy.2018.03.041.
- XUE, K.; LI, K.; CHEN, W.; CHONG, D.; YAN, J.. Numerical Investigation on the Performance of Different Primary Nozzle Structures in the Supersonic Ejector. **Energy Procedia**, v. 105, p. 4997–5004, 2017. DOI: 10.1016/j.egypro.2017.03.1000.
- YADAV, R. L.; PATWARDHAN, A. W. Design aspects of ejectors: Effects of suction chamber geometry. **Chemical Engineering Science**, v. 63, n. 15, p. 3886–3897, 2008. DOI: 10.1016/j.ces.2008.04.012.
- YAPICI, R.; ALDAS, K. Optimization of water jet pumps using numerical simulation. **Proceedings of the Institution of Mechanical Engineers, Part A: Journal of Power and Energy**, v. 227, n. 4, p. 438–449, 2013. DOI: 10.1177/0957650913487529.
- ZHANG, H.; WANG, L.; JIA, L.; ZHAO, H.; WANG, C. Influence investigation of friction on supersonic ejector performance. **International Journal of Refrigeration**, v. 85, p. 229–239, 2018. DOI: 10.1016/j.ijrefrig.2017.09.028.
- ZHANG, K.; ZHU, X.; REN, X.; QIU, Q.; SHEN, S.. Numerical investigation on the effect of nozzle position for design of high performance ejector. **Applied Thermal Engineering**, v. 126, p. 594–601, 2017. DOI: 10.1016/j.applthermaleng.2017.07.085.
- ZHENG, L.; DENG, J. Experimental investigation on a transcritical CO<sub>2</sub> ejector expansion refrigeration system with two-stage evaporation. **Applied Thermal Engineering**, v. 125, p. 919–927, 2017. DOI: 10.1016/j.applthermaleng.2017.07.056.
- ZHU, Y.; CAI, W.; WEN, C.; LI, Y. Numerical investigation of geometry parameters for design

of high performance ejectors. **Applied Thermal Engineering**, v. 29, p. 898–905, 2009. DOI: 10.1016/j.applthermaleng.2008.04.025.

ZHU, Y.; WANG, Z.; YANG, Y.; JIANG, P. X. Flow visualization of supersonic two-phase transcritical flow of CO<sub>2</sub> in an ejector of a refrigeration system. **International Journal of Refrigeration**, v. 74, p. 352–359, 2017. DOI: 10.1016/j.ijrefrig.2016.11.012.